DYNAMIC MODELING, CONTROL AND OPTIMIZATION OF PEM FUEL CELL SYSTEM FOR AUTOMOTIVE AND POWER SYSTEM APPLICATIONS

by

WOON KI NA

Presented to the Faculty of the Graduate School of

The University of Texas at Arlington in Partial Fulfillment

of the Requirements

for the Degree of

DOCTOR OF PHILOSOPHY

THE UNIVERSITY OF TEXAS AT ARLINGTON

May 2008

Dedicated to my beloved wife Eun Ji Seo and Family

ACKNOWLEDGEMENTS

I am really honored to take this opportunity to express my appreciation to all those people who have supported me during my Ph.D. program at the University of Texas at Arlington.

First of all, I would like to thank my advisor of Ph.D. program, Dr. Bei Gou for his support, guidance, and encouragement throughout my Ph.D. study. I also would like to thank to other committee members: Dr. Wei-Jen Lee, Dr. Raymond Shoults, Dr. William E Dillon, and Dr. Bumsoo Han, for their valuable suggestions, advice, and comments about my research. I want to thank to Dr. Bill Diong and Dr. Kai S. Yeung, who helped me to establish my background of the fuel cell systems and control theory solidly. Also, I would like to express special thanks to my graduate advisor of Master's program, Dr. Seung Gi Jeong at Kwangwoon University in Seoul, Korea, who led me to study in power electronics.

Furthermore, without the consistent support from my dearest wife, Eun Ji Seo, and my parents, Chang Seok Na and Seok Ja Yoon, it could have been impossible for me to achieve these research works. I would like to give warm thanks to Dr. Esther K. Yang, who not only showed me how to be a good researcher, but also demonstrated how to be a dedicated citizen who helps others. I want to thank all members of the Korean Martyrs Catholic Church community in Bedford, TX, especially Dr. Yong Hoo Kwon, who showed his devotion to God. I want to thank Rev. Simon Jeung Rae Cho,

who baptized me and introduced a different perspective of being a dedicated believer. I also want to express special thanks to all my dear friends at the University of Texas at Arlington: Dr. Wieder Chung, Ms. Xioa Hu, Mr. Yunzhi Chen, Dr. Zheng Hui, Mr. Bohoon Kim, Mr. Daewoo Kim, Mr. Kunhee Han, Mr. Sangseuk Park, Mr. Yongsik Seo, Mr. Hyunjoo Jin, Mr. Kyungseo Park, Dr. Young Rael Lee, Dr. Jae Gwan Kim, Dr. Jeong Gyu Lee, Dr. Juhan Kim, and Dr. Do Nyun Kim, for their encouragements and friendships.

Finally, my Lord Jesus Christ deserves to receive more thanks than anyone. He always stands by me, loves me, and gives me a right direction. Needless to say, thanks to his trust, I get my strength and belief, which leads me to finish my study, help others, and make better society for youngsters. Even he blesses my wife and me to have my dearest son, Daniel Hyun Na. Currently all I have are thanks to him.

April 8, 2008

ABSTRACT

DYNAMIC MODELING, CONTROL AND OPTIMIZATION OF PEM FUEL CELL SYSTEM FOR AUTOMOTIVE AND POWER SYSTEM APPLICATIONS

Woon Ki Na, Ph.D.

The University of Texas at Arlington, 2008

Supervising Professor: Bei Gou

This dissertation is focusing on fuel cell dynamic modeling and control, the optimization design of fuel cell systems, power electronics interface designs, and control for the fuel cell based hybrid system.

First, a dynamic PEM fuel cell model is proposed as a nonlinear, multiple-input, multiple-output (MIMO) system so that feedback linearization can be directly utilized and the PEM fuel cells can be protected through the controller. For the design of the dynamic model PEM fuel cells, all possible water effects are considered, and the anode and cathode gas pressures, as well as the fuel cell voltage are defined as the control objectives. In terms of optimization of the fuel cell systems, the efficiency and the cost

models of fuel cell system have been optimized under various operating conditions using a multi-objective optimization technique, the SQP (sequential quadratic programming) method.

Second, due to a slow dynamics of fuel cell system by nature, it is recommended to have an additional auxiliary power such as ultra-capacitors or battery during transients to improve system performance in stationary power and transportation applications. Using ultracapacitors and bidirectional converter with the fuel cell system can be a possible solution to the problem of slow dynamics of the fuel cell system. In this research, we present a combined small signal ac equivalent circuit model consisting of bidirectional converter, PEM fuel cell, and ultracapacitor for the purpose to design an appropriate controller for the bidirectional converter during buck and boost mode. Transient performance of the fuel cell based hybrid system including fuel cell model, ultracapacitor and bidirectional converter is simulated.

At last, a supervisory control strategy for a hybrid power system consisting of fuel cell, solar cell and energy storage is proposed. Using ultra-capacitors and photovoltaic (PV) panel together with a fuel cell system is another feasible consideration to provide a sufficient power supply for residential areas. Four modes of operations of this hybrid power system are defined for the proposed supervisory control. The proposed hybrid power system is simulated and analyzed based upon the supervisory control algorithm in Matlab/Simulink environment.

Therefore, this dissertation will be a good platform for modeling,control and optimization of the fuel cell system and its applications such as hybrid power systems.

TABLE OF CONTENTS

LIST OF ILLUSTRATIONS

LIST OF TABLES

CHAPTER 1

INTRODUCTION

1.1 Background

A fuel cell system is widely regarded as one of the most promising energy sources due to its high energy efficiency, extremely low emission of oxides of nitrogen and sulfur, very low noises, and the cleanness of its energy production. In addition, a fuel cell system can be run with other conventional and alternative fuels such as hydrogen, ethanol, methanol, and natural gas. Based on the currently used types of electrolytes, fuel cells are classified into polymer electrolyte membrane fuel cells (PEMFCs), solid oxide fuel cells (SOFCs), phosphoric acid fuel cells (PAFCs), molten carbonate fuel cells (MCFCs), alkaline fuel cells (AFCs), direct methanol fuel cells (DMFCs), zinc air fuel cells (ZAFCs), and photonic ceramic fuel cells (PCFCs) [1].

To date, Polymer Electrolyte Membrane Fuel Cells (PEMFCs), known as PEMFCs, have been considered as the best candidate for the fuel cell vehicle and small and mid-size distributed generators because it has a high power density, solid electrolyte, long stack life, and low corrosion. Besides, PEMFCs operate at low temperatures (50–100 °C), which enables fast start-up. Thus, PEMFCs are particularly attractive for transportation applications that require rapid start ups and fast dynamic responses over transient times (stop and go, acceleration and deceleration).

The fuel cells have a greater efficiency than internal combustion engines. It [2] notes that the efficiency of a fuel cell vehicle using direct hydrogen from the natural gas

is two times greater than that of an internal combustion engine vehicle. However, for the commercialization of fuel cell vehicles, their performance, reliability, durability, cost, fuel availability and cost, and public acceptance should be considered [3]. Specially, the performance of the fuel cell systems during transients is one of key components for success of commercialization of fuel cell vehicles. Therefore, during transients, in order to generate a reliable and efficient power response and to prevent membrane damage as well as detrimental degradation of the fuel cell stack voltage and oxygen depletion, it is necessary to design a better control scheme to achieve optimal air and hydrogen inlet flow rates—i.e., fuel cell control system that can perform air and hydrogen pressure regulation and heat/water management precisely based on the current drawn from the fuel cell system [4, 5].

Since the fuel cell efficiency is closely related to the fuel cell economics, a multi-objective optimization study regarding the efficiency and cost of the fuel cell systems is also needed to get the cost effective fuel cell system.

As for the dynamics responses of fuel cell system, because the fuel cell system has a slow dynamics by nature, it is recommended to have an additional auxiliary power such as ultra-capacitors or battery during transient times to improve system performance in stationary power and transportation applications. With using ultracapacitors or battery and bidirectional converter into a hybrid power generation system, it can be a good solution for compensating the problem regarding the slow dynamics of the fuel cell system.

Hence, in this thesis, the advanced control method of PEM fuel cells system and optimization study and hybridization of the fuel cell system will be delivered as the main topics.

1.2 Fuel cells Overview

A fuel cell is an electrochemical energy device that converts the chemical energy of fuel directly into DC electricity and heat, with water as a byproduct of the reaction.

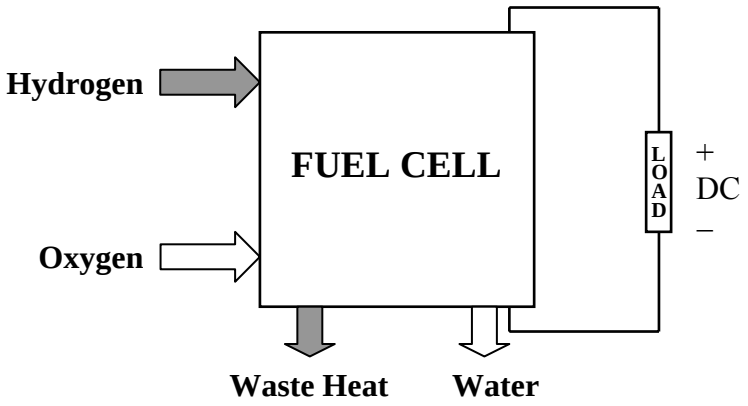

Figure 1.1 Fuel cell directly generates DC electricity

In terms of producing electricity by electrochemical process, a fuel cell is similar to a battery but a fuel cell requires continuous fuel and oxidant supplies to generate electricity constantly, while a battery does not need any external fuel supply except for recharging when external electricity is applied.

As seen in Figure 1.1, a fuel cell generates electricity at efficiencies of 40% to 60% in a single step [4] and it does not involve in any moving part [5]. Due to its high

efficiency and low noises, it can be used in stationary power applications and can be extended to the transportation applications based on selecting a type of fuel cells. In the 1960, the first practical PEM fuel cells were developed and these fuel cells were used in the Gemini program for space applications. Since then, fuel cells have been successful in the U.S. space program but for terrestrial applications, just the last 10 to 15 years have been remarkable for terrestrial applications. In 1993, Ballard Power System demonstrated fuel cell powered buses. All major automotive manufacturers already developed prototypes of fuel cell vehicle in the late 1990s and the early 2000s, which are undergoing test in the U.S, Japan and Europe. For stationary power applications, more than 2500 fuel cell stationary power systems have been installed globally for hospital, building, utility power plants, and so on. In 2005, Samsung Electronics also unveiled a prototype of fuel cells that run a laptop for 15 hours for portable power applications. However, there are many challenges and technical issues of commercialization of fuel cells. The most significant problems are reducing fuel cells costs as well as improving fuel cell operating liability.

1.3 Literature Review

To develop a control algorithm of PEMFCs, in the first step, the PEM fuel cell system has to be accurately modeled to apply a suitable nonlinear control technique. Many PEMFCs models, including both stationary and dynamic models [6–18] have been reported in the literatures or the control design applied to a fuel cell vehicle [6–8, 21] and a distributed generation system [19, 20]. Unfortunately, those models are

mainly for experimental verifications other than control design [9–18] or for prediction of the fuel cell phenomenon by analyzing an electrochemical reaction, the thermodynamics, and the fluid mechanics. Recently, Purkrushpan et al. [6] developed a control-oriented PEMFC model that includes flow characteristics and dynamics of the compressor and the manifold (anode and cathode), reactant partial pressures, and membrane humidity.

However, because of the nonlinear relationship between stack voltage and load current shown in the V–I polarization curve [1] and the state equations [6, 17], it is a challenge to develop a nonlinear controller for the PEMFC. Because of operational parametric uncertainties such as the parametric coefficients for each cell on kinetic, thermodynamic, and electrochemical foundations and the resistivity of the membrane for the electron flow, the linear PEMFC models proposed by Purkrushpan et al. [6-9] and L. Y. Chiu et al. [17] using Jacobian linearization via a Taylor series expansion at the nominal operating point can not easily achieve a satisfactory dynamic performance under large disturbances. An accurate nonlinear dynamic model is required to develop an advanced the fuel cell control system considering the nonlinearity and uncertainty that need to be proposed.

A. Sakhare et al. [22] developed a fuzzy control system for a boost DC/DC converter of a fuel cell system. Neural optimal control was presented for the PEMFC by using artificial a neural network (ANN) in [23]. However, instead of controlling the PEM fuel cell system, the neural optimal control is mainly focused to derive a new

architecture to synthesize an approximated optimal control by means of ANN, where the PEM fuel cell was chosen as a test bed.

In terms of optimization of PEMFCs, at present, although many techniques about optimization of fuel cell systems have been developed, many of them [24, 25] are restricted to only one optimization objective such as its performance or cost. However, because these different optimization objectives are coupled or affected each other, only considering one is not realistic or practical. Lately, a few studies of multi-objectives concerning the cost and performance of fuel cell systems have been reported in the literature [70]. Xue and Dong [70] searched for the optimal design of a Ballard fuel cell system with the consideration of the fuel cell system performance and cost. In their work, two system parameters, the active stack intersection area and air stoichiometric ratio were selected as the design variables in the joint optimization. Frangopoulos and Nakos [48] studied the optimal design of the 5kW PEM fuel cell where the fuel cell power density and the present worth of the life cycle cost of the system were used as the objectives of optimization.

The fuel cell system intrinsically has a slow response time due to its chemical reaction and its voltage varies under the load changes. For instance, the fuel cell voltage reaches to the maximum when no load is applied, while it drops as load currents increases. Particularly for high currents, significant voltage drop can be seen due to the activation overvoltage and ohmic resistance losses in the membrane [1]. Thus, a secondary energy source is needed to satisfy the load demands. Up to date, many studies regarding using the secondary power sources for the fuel cell system have been

performed [28-32]. Most studies have been conducted for transportation applications [28-32]. Lately, U. Unzunoglu and Alam [32] used the ultracapacitor in parallel to fuel cell systems without using a bidirectional converter for residential applications. This control scheme may create a problem regarding efficinetly charging and discharing the ultracapacitor during transients.

By the literature review, the problems regarding control, optimization and power applications of PEMFCs have been identified.

1.4 Research Objective

There are three research objectives in this thesis. First is about modeling and control of PEMFCs. The new dynamic nonlinear model of PEMFCs is proposed, which considers all possible water components in the fuel cells and therefore more accurate fuel cell modeling can be achieved. In terms of control approach of PEMFCs, the feedback linearization, a well-known nonlinear approach, is applied to design a controller based on the proposed nonlinear dynamic fuel cell model, to achieve more robust transient behavior. By doing so, the fuel cell stack life can be prolonged and the fuel cell system can be protected by minimizing the deviations between the anode and cathode gas pressures [7, 21].

The change of the stack temperature dramatically affects the output current and the output power of the fuel cells system. In order to achieve better qualities of output current and output power, a new thermal equivalent circuit of PEMFCs is proposed, which makes it easier to develop the temperature control algorithm for PEMFCs.

Second is the optimization of PEMFCs. A multi-objective optimization technique is applied to optimize two objectives, the efficiency and the cost of the fuel cell system under different operating conditions. By defining the system pressure, hydrogen and air stoichiometric ratios, the cell voltage and current density as design variables, the structure of more cost effective fuel cell system with a high efficiency can be determined.

The last topic is an application of this fuel cell system. Since the fuel cell system has a slow dynamics by nature, it is recommended to have an additional auxiliary power such as ultra-capacitors or battery during transients to improve system performance in stationary power and transportation applications. Using ultracapacitors and bidirectional converter with fuel cell system can compensate the problem of slow dynamics of the fuel cell system. In this study, we present a combined small signal ac equivalent circuit model consisting of a bidirectional converter, a PEM fuel cell, and an ultracapacitor for the purpose to design an appropriate controller for the bidirectional converter. Other things are hybridization and integration of the fuel cell system with other systems solar cell system, ultracapacitor, power conditioning units and reformer.

1.5 Thesis Outline

In Chapter 1, background of the thesis, the fuel cell overview, literature review and the research objective are described. Chapter 2 explains the general information of fuel cell systems and presents a nonlinear dynamic model of PEMFCs to develop its control algorithm. The thermal equivalent circuit is provided to design a suitable

temperature controller. In Chapter 3, a nonlinear controller is designed based on the proposed nonlinear dynamic model to prolong the stack life of PEM fuel cells. Feedback linearization is applied to the PEM fuel cell system so that the pressure deviation between the anode and the cathode in the stack can be kept as small as possible during disturbances or load variations. The proposed dynamic model was tested in Matlab/Simulink environment. The simulation results are provided such that PEMFCs equipped with the proposed nonlinear controller have better transient performances than those with linear controller. In addition to the nonlinear controller, a temperature controller for PEMFCs is proposed and tested using the proposed thermal equivalent circuit model of PEMFCs through Matlab/Simulink simulation.

Chapter 4 involves a multi-objective optimization study of PEMFCs. The efficiency and cost model of PEMFCs for 50kW automotive applications are presented and the efficiency and the cost of the fuel cell system have been optimized under various operating conditions.

In Chapter 5, a small signal transfer function of bidirectional converter with the fuel cell and ultracapaciator is presented. Also, the control scheme design of the charging a discharging for the ultracapacitor via bidirectional converter is explained. The simulation results for the proposed controller are given in the chapter. For a fuel cell based the hybrid power system and its coordination with other systems like ultracapacitor and photovoltaic system, a supervisory control strategy of the hybrid system is also discussed.

Chapter 6 provides a conclusion and future work of the thesis.

CHAPTER 2

PEM FUEL CELLS SYSTEMS MODELING

2.1 Introduction

For preliminary fuel cell power system planning, stability analysis, control strategy synthesis, and evaluation, an appropriate dynamic model of a fuel cell system is desired. Since the existing control oriented models [4, 5, 6] do not contain all water components, which are one of the important factors of fuel cell systems [1], it is difficult to design an accurate dynamic fuel cell model based on the existing models. The main objective of developing a dynamic model of PEMFCs is to design a nonlinear control strategy to prevent fuel cell stack damage and to prolong the stack life by controlling the anode and cathode gases pressures. In this chapter, general knowledge of fuel cell systems is discussed in Section 2.2. For modeling of PEMFCs, the PEMFCs voltage model, its thermal equivalent circuit model, and the state space dynamic model are presented in Sections 2.3, 2.4, and 2.5 respectively. With using these models of the fuel cells, an appropriate controller of fuel cell systems can be designed and the details are described in Chapter 3.

2.2 Fuel Cell Systems

A fuel cell produces electrical energy in a direct manner by converting the chemical energy of fuel directly into electricity and heat, with water as a by product of

the reaction. A single fuel cell consists of an electrolyte and two catalyst-coated electrodes (a porous anode and cathode) in Figure 2.1. Several different types of fuel cells are classified by the kind of electrolyte in Table 2.1.

Table 2.1 Different Types of Fuel Cell [1, 5]

Fuel Cell Type	**Alkaline (AFC)**	**Proton Electrolyte Membrane (PEMFC)**	**Phosphoric acid (PAFC)**	**Molten carbonate (MCFC)**	**Solid Oxide (SOFC)**
Electrolyte	KOH	Perfluro-sulfonated acid polymer	Phosphoric acid	Combination of alkali (Li, Na,K)	Y_2O_3-stabilized ZrO_2(YSZ)
Mobile Ion	OH^-	H^+	H^+	CO_3^{2-}	O^{2-}
Operating Temperature	50–200°C	60-80 °C	150-220 °C	600-700 °C	800-1000 °C
Catalyst	Ni, Ag, and metal oxides	Pt	Pt	Ni(anode) Nickel oxide (cathode)	Co- ZrO_2/ Ni- ZrO_2 (anode), Sr-doped $LaMnO_3$ (cathode)
Application and Notes	Space program (Apollo and space shuttle) since 1960	Automotive and small scale distributed generator and portable power	200kW stationary electric generation (UTC)	Medium to Large scale generation but demonstration stage	2kW to large scale generation but demo stage.

Although PEMFCs need a expensive catalyst (Pt) and many cares especially for water management and other control matters, its operation temperature is lower than other types of fuel cell and its start up time is faster and therefore PEMFCs are the best candidate for automotive applications and small scale distributed power generation(less than 200kW) as well as portable power systems. The basic operation chemical principle

of each fuel cell is the same and the differences are in use of electrolyte and catalyst. So, our research objective is related to PEMFCs and thereby the basic operation of PEMFCs and its voltage model will be explained in the following subchapter.

2.3 PEMFCs and Voltage Model

A PEM fuel cell consists of a polymer electrolyte membrane sandwiched between two electrodes (anode and cathode) in Figure 2.1. In the electrolyte, only ions can pass by, and electrons are not allowed to go through. So, the flow of electrons needs a path like an external circuit from the anode to the cathode to produce electricity because of potential difference between the anode and cathode. The overall electrochemical reactions for a PEM fuel cell fed with hydrogen-containing anode gas and oxygen-containing cathode gas are as follows:

Anode: $2H_2 \leftrightarrow 4H^+ + 4e^-$

Cathode: $O_2 + 4H^+ + 4e^- \leftrightarrow 2H_2O$

Overall reaction: $2H_2 + O_2 \leftrightarrow 2H_2O + \text{electricity} + \text{heat}$

In practice, a 5-kW fuel cell stack, such as a Ballard MK5-E PEMFC stack, uses a pressurized hydrogen tank at 10 atm and oxygen taken from atmospheric air [24, 25]. In case of using reformer, on the anode side, a fuel processor called reformer that generates hydrogen through reforming methane or other fuels like natural gas, can be used instead of the pressurized hydrogen tank.

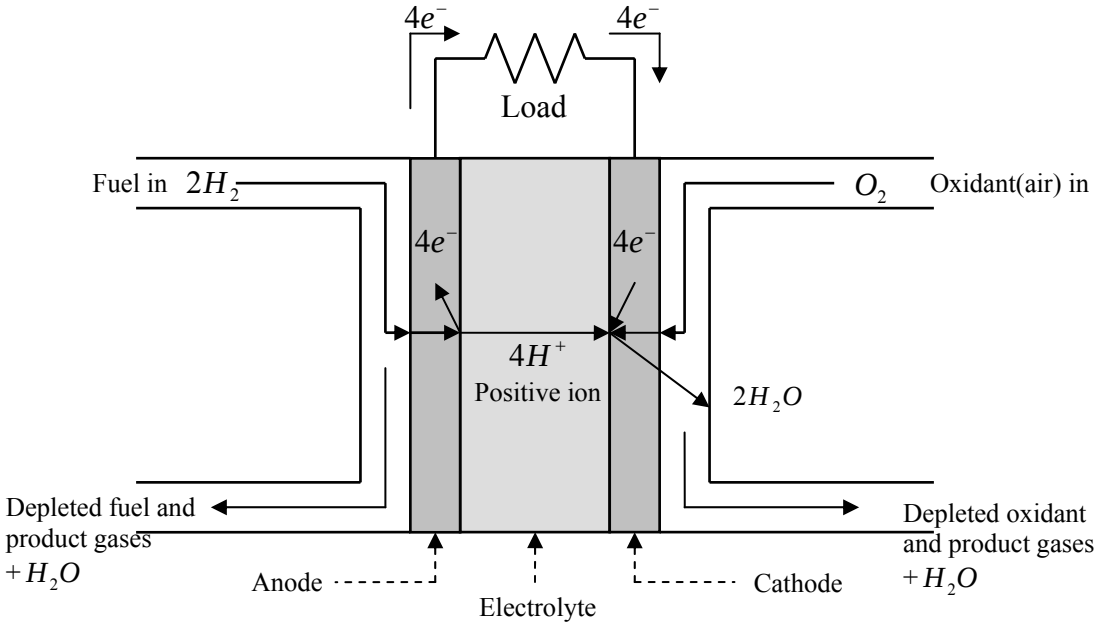

Figure 2.1 Schematic of fuel cell operation

A pressure regulator and purging of the hydrogen component are also required. On the cathode side, an air supply system containing a compressor, an air filter, and an air flow controller are required to maintain the oxygen partial pressure [1, 5, 7, 20]. On both sides, a humidifier is needed to prevent dehydration of fuel cell membrane [1, 5, 7]. In addition, a heat exchanger, a water tank, a water separator, and a pump may be needed for water and heat management in the fuel cell systems [1, 5, 7].

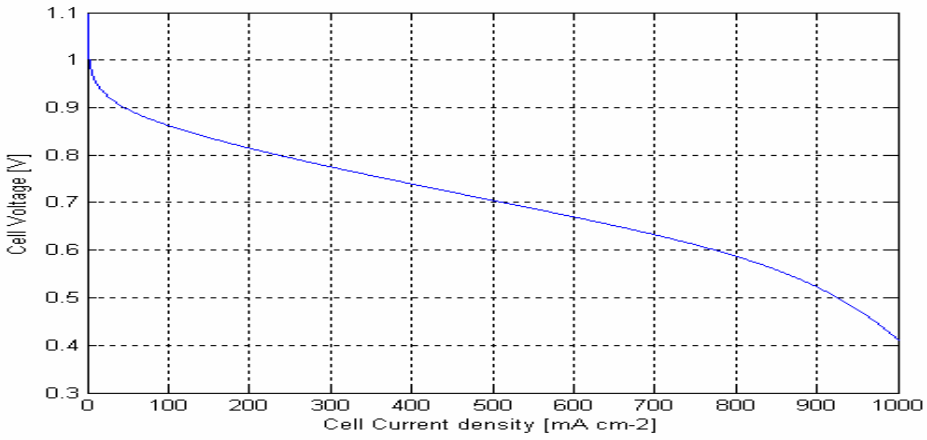

Figure 2.2 Polarization V-I curve (Ballard Mark V PEMFC at 70^{o} C) [1]

To produce a higher voltage, multiple cells have to be connected in series. Typically, a single cell produces voltage between 0 and 1 volt based on the polarization I-V curve, which expresses the relationship between the stack voltage and the load current [1, 5, 7]. Figure 2.2 shows that their relationship is nonlinear and mainly depends on current density, cell temperature, reactant partial pressure, and membrane humidity [1, 5, 7].

The output stack voltage V_{st} [1] is defined as a function of the stack current, reactant partial pressures, fuel cell temperature, and membrane humidity:

$$V_{st} = E - V_{activation} - V_{ohmic} - V_{concentration} \tag{2-1}$$

In the above equation,

$E = N_o \cdot \left[V_o + \frac{RT}{2F} \ln\left(\frac{P_{H_2} \sqrt{P_{O_2}}}{P_{H_2O_c}} \right) \right]$ is the thermodynamic potential of the cell or reversible voltage based on Nernst equation [1], $V_{activation}$ is the voltage loss due to the rate of

reactions on the surface of the electrodes, V_{ohmic} is the ohmic voltage drop from the resistances of proton flow in the electrolyte, and $V_{concentration}$ is the voltage loss from the reduction in concentration gases or the transport of mass of oxygen and hydrogen. Their equations are given as follows:

$$V_{activation} = N \cdot \frac{RT}{2\alpha F} \cdot \ln\left(\frac{I_{fc} + I_n}{I_o}\right) \tag{2-2}$$

$$V_{ohm} = N \cdot I_{fc} \cdot R_{ohm} \tag{2-3}$$

$$V_{concentraton} = N \cdot m\exp(n \cdot I_{fc}) \tag{2-4}$$

In Equation (2-1), P_{H_2}, P_{O_2}, and $P_{H_2O_c}$ are the partial pressures of hydrogen, oxygen, and water, respectively. Subscript *c* means the water partial pressure, which is vented from the cathode side.

Table 2.2 PEMFCs Ballard Mark V Voltage Parameters [1]

Parameter	**Value and Definition**
N	Cell number: 35
V_o	Open-cell voltage: 1.032[V]
R	Universal gas constant [J/mol-k]: 8.314[J/mol-k]
T	Temperature of the fuel cell [K]: 353 [K]
F	Faraday constant [C/mol]: 96485 [C/mol]
α	Charge transfer coefficient: 0.5
M	Constant in the mass transfer voltage: 2.11×10^{-5} [V]
N	Constant in the mass transfer voltage: $8\times10^{-3}[cm^2mA^{-1}]$
R_{ohm}	2.45×10^{-4} [$k\Omega cm^2$]
A_{fc}	Fuel cell active area: 232 [cm^2]
I_0	Exchange current density [A/cm^2]
I_n	Internal current density [A/cm^2]

A detailed explanation of each voltage loss can be found in [1], and other voltage descriptions are also reported in [6-8, 10], where the fuel cell voltage is mainly addressed by the combination of physical and empirical relationships in which many parametric coefficients of the membrane water content, humidity, and temperate, as well as the reactant concentrations are involved. To establish the state equation about the fuel cell voltage, first-order dynamic modeling is also applied [1]. By assuming the size of capacitor C_{fc} in the fuel cell stack to be 1 F and the stack resistor R_a to be 0.22Ω, the time constant of the fuel cell stack is determined to be $\tau_{fc} = R_a \cdot C_{fc} = 0.22$ sec [26]. Therefore, the first-order dynamic modeling of PEMFC is as follows:

$$E - V_{st} = \frac{R_a}{1 + R_a \cdot C_{fc} s} I_{fc} + R_{ohm} \cdot I_{fc} \tag{2-5}$$

where E is the reversible potential of the fuel cell in Equation (2-5). The dynamics model of the fuel cell can be shown in Figure 2.3.

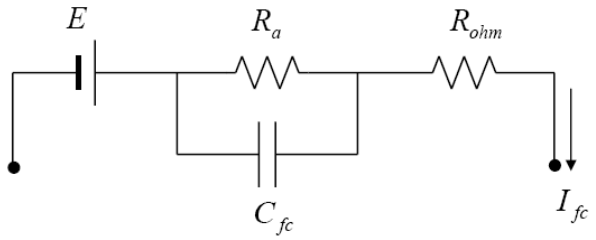

Figure 2.3 Fuel cell equivalent circuit

where R_a is a sum of the activation and concentration resistance, C_{fc} is a capacitive constant, and R_{ohm} is the ohmic resistance. In [26], by assuming that the electrical time constant τ_e ($\tau_e = 0.0004\,\text{sec}$) regarding the ohmic resistance is much small than the fuel

cell time constant, τ_{fc}, ($\tau_{fc} = 0.22\,\text{sec}$), the first order dynamic relation of PEMFCs between the fuel cell stack voltage and the fuel cell stack terminal voltage, V_{fc} can be as follows:

$$V_{fc} = \frac{1}{(1+\tau_{fc}s)} V_{st} \tag{2-6}$$

2.4 Thermal Equivalent Circuit Model of PEMFCs

The temperature of a fuel cell is one of the important factors for the fuel cell mechanism and maintaining the stack temperature to the desired level is directly related to the fuel cell performance [1, 7, 27]. Figure 2.4 shows that the polarization curve is shifted upward as the temperature increases. A quite number of control oriented fuel cell models [6-19, 24, 27] have been developed under the assumption that the operating temperature is constant. Although controlling the temperature is vital for the fuel cell operation, those models [6-19, 24, 27] have not considered the temperature as a state variable due to the complexity and long time constant(over 2000 sec) of temperature in the fuel cell system[11]. In our study, the temperature is defined as one of state variables and a control strategy is developed accordingly for PEMFCs through the study of the transient thermal model [9, 10, 20, 24] of PEMFCs.

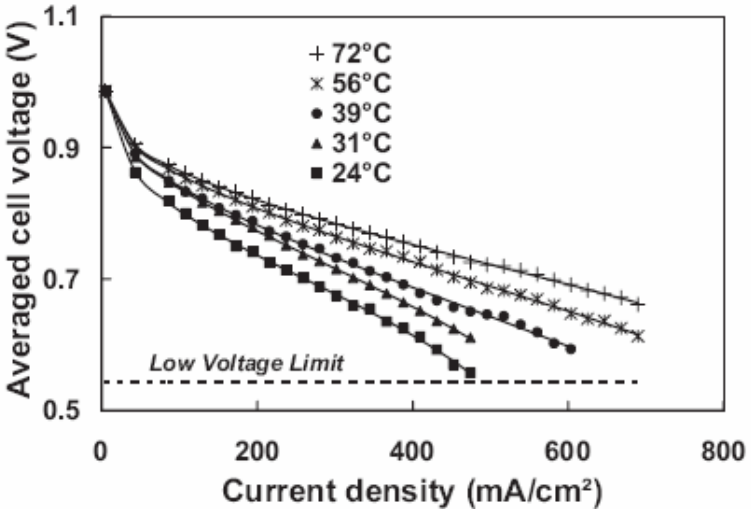

Figure 2.4 Polarization curves for different temperatures [17]

Several thermal models of PEMFC have been reported in [9, 10, 20, 24]. However, those models are not for a controlled oriented but the mathematical analysis and its experimental validation. In our study, based on the use of available transient thermal models [9, 10, 20, 24], the control oriented dynamic thermal model is developed in this section.

A transient energy balance is described by [9, 10, 24]

$$\dot{Q}_{stack} = C_t \frac{dT_s}{dt} = P_{tot} - P_{elec} - \dot{Q}_{cool} - \dot{Q}_{loss} \tag{2-7}$$

where $\dot{Q}_{stack}$ is the rate of heat absorption (Js^{-1}) by the stack, C_t is the thermal capacitance ($J^{o}C^{-1}$), P_{tot} is the total power released by chemical reaction (W), P_{elec} is the power consumed by the load (W), $\dot{Q}_{cool}$ is the heat flow rate of the cooling system (heat exchanger) and $\dot{Q}_{loss}$ is the heat flow rate through the stack surface.

The total energy can be expressed by the rate of hydrogen consumption as Equation (2-8)

$$P_{tot} = \dot{m}_{H_2\_used}\Delta H = \frac{NI_{fc}}{2F}\Delta H \tag{2-8}$$

where ΔH is the enthalpy change for hydrogen (285.5kJ $mols^{-1}$), and $\dot{m}_{H_2\_used}$ is the hydrogen consumption rate.

The electrical power output is given by

$$P_{elec} = V_{st} I_{fc} \tag{2-9}$$

The rate of removal of heat by the cooling water is directly related to the water flow in the heat exchanger. The relationship is as follows [26]

$$\dot{Q}_{cool} = \dot{m}_{cool\_water} \cdot c_p \cdot \Delta T_s \tag{2-10}$$

where $\dot{m}_{cool\_water}$ is the water pump flow (SLPM), c_p is the specific heat coefficient of water (4182J/kg K) and ΔT_s is allowable temperature rise (10K). The water pump flow can be expressed by the time delay and conversion factor as Equation (2-11).

$$\dot{m}_{cool\_water} = \frac{k_c}{(1+\tau_c s)} u_{cl} \tag{2-11}$$

where τ_c is the time delay constant, 70 sec, k_c is the conversion factor, 1.5, which means that if the control input u_{cl} for the heat exchanger ranges in 0~10(V), $\dot{m}_{cool\_water}$ ranges in 0-15 (SLPM) with 70 seconds delay.

The heat loss by the surface of the stack is calculated by Equation (2-12)

$$\dot{Q}_{loss} = hA_{stack} \cdot (T_s - T_{amb}) = \frac{T_s - T_{amb}}{R_t} \tag{2-12}$$

where hA_{stack}, stack heat transfer coefficient, is 17WK^{-1} [6, 7, 11], T_{amb} is the ambient temperature 25^{o}C (298.15K)±5% and R_t is the thermal resistance of the stack, which is the reciprocal of hA_{stack} is 0.0588 (KW^{-1}).

The thermal time constant of the fuel cell is given by

$$\tau = R_t C_t = \frac{MC}{hA_{stack}} \tag{2-13}$$

where MC is the product of stack mass and average specific heat, 35(kJK^{-1}), the thermal capacitance C_t is 35(kJK^{-1}), and τ is 2,059 seconds [11].

As seen in Equation (2-6), the thermal equivalent circuit model with four dependent sources can be developed by employing the circuit analogy [12].

$$C\frac{dv}{dt} = i \tag{2-14}$$

where the stack temperature corresponds to voltage, energy flows (P_{tot}, P_{elec}, $\dot{Q}_{cool}$, and $\dot{Q}_{loss}$) corresponds to current, and the thermal capacitance C_t corresponds to capacitance.

In Figure 2.5, various load changes cause the changes of fuel cell stack temperature, and therefore the fuel cell voltage and current can be used as an external inputs or disturbance and therefore the stack temperature is used for an output when designing the controller. The total power, P_{tot} depends on the hydrogen consumption

based on the load changes and the electrical power, P_{elec} depends on the load current. And the cooling power $\dot{Q}_{cool}$ and the heat loss by the surface of the stack, $\dot{Q}_{loss}$ are a function of the fuel cell stack temperature change. For this reason, four dependent energy flow sources are involved in the thermal equivalent circuit of the fuel cell in Figure 2.5.

The u_{cl} in the water pump flow is defined as a control variable input.

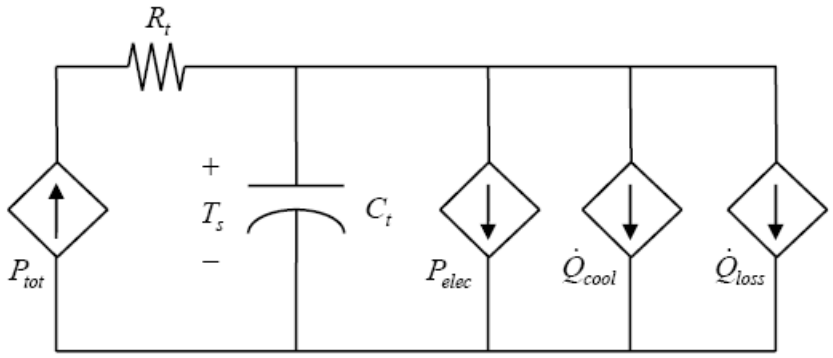

Figure 2.5 Thermal equivalent circuit of the fuel cell

2.5 State Space Dynamic Model of PEMFCs

To derive a simplified nonlinear dynamic PEMFC model, the following assumptions are made:

• Due to slower dynamics of the stack temperature, the average stack temperature is assumed to be constant.

• The relative humidity can be well controlled to a little over 100%, and thereby the liquid water always forms the stack. This liquid water is perfectly managed

by the water tank and water separator and the water flooding effects can be controlled.

• A continuous supply of reactants is fed to the fuel cell to allow operation at a sufficiently high flow rate.

• The mole fractions of inlet reactants are assumed to be constant in order to build the simplified dynamic PEMFC model. In other words, pure hydrogen (99.99%) is fed to the anode, and the air that is uniformly mixed with nitrogen and oxygen by a ratio of, say, 21:79, is supplied to the cathode.

• The full state has to be measured to utilize feedback linearization [27].

The ideal gas law and the mole conservation rule are employed. Each partial pressure of hydrogen, the water from the anode, and the oxygen, nitrogen, and water from the cathode are defined as state variables of the PEMFC. The relationship between inlet gases and outgases is described in Figure 2.6 [28].

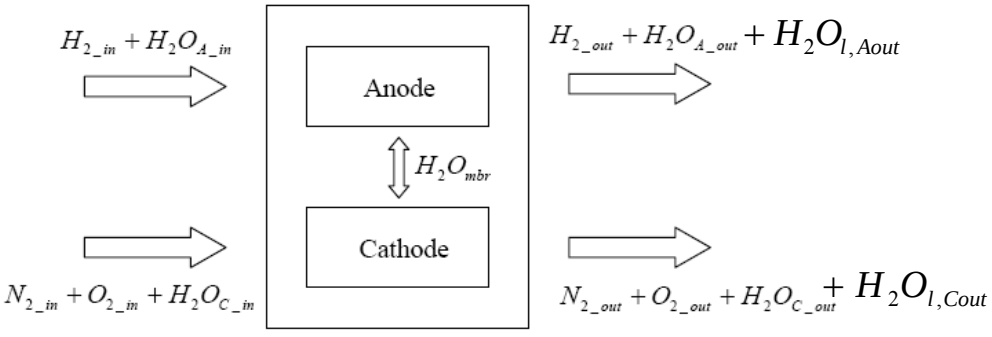

Figure 2.6 Gas flows of PEMFCs

The partial-pressure derivatives are given by the following equations.

Anode mole conservation:

$$\frac{dP_{H_2}}{dt} = \frac{RT}{V_A}(H_{2in} - H_{2used} - H_{2out})$$
$$\frac{dP_{H_2O_A}}{dt} = \frac{RT}{V_A}(H_2O_{Ain} - H_2O_{Aout} - H_2O_{mbr} + H_2O_{back} - H_2O_{l,Aout}) \quad (2\text{-}15a)$$

Cathode mole conservation:

$$\frac{dP_{O_2}}{dt} = \frac{RT}{V_C}(O_{2in} - O_{2used} - O_{2out})$$
$$\frac{dP_{N_2}}{dt} = \frac{RT}{V_C}(N_{2in} - N_{2out}) \quad (2\text{-}15b)$$
$$\frac{dP_{H_2O_C}}{dt} = \frac{RT}{V_C}(H_2O_{Cin} + H_2O_{Cproduced} - H_2O_{Cout} + H_2O_{mbr} - H_2O_{mbr} - H_2O_{l,Cout})$$

where $H_{2in}, O_{2in}, N_{2in}, H_2O_{Ain}$, and H_2O_{Cin} are the inlet flow rates of hydrogen, oxygen, nitrogen, the anode-side water, and the cathode-side water, respectively. In addition, $H_{2out}, O_{2out}, N_{2out}, H_2O_{Aout}$, and H_2O_{Cout} are the outlet flow rates of each gas. H_{2used}, O_{2used}, and $H_2O_{Cproduced}$ are the usage and the production of the gases, respectively. In general, the membrane water inlet flow rate H_2O_{mbr} across the membrane is a function of the stack current and the membrane water content λ_m. By assuming that $\lambda_m = 14$ [7, 29], H_2O_{mbr} is defined as a function of the current density only, and $H_2O_{mbr} = 1.2684\frac{N \cdot A_{fc} \cdot I_{fc}}{F}$ [7, 29], where $A_{fc}(cm^2)$ is the fuel cell active area, N is the number of the fuel cells, and I_{fc} is the fuel cell current density.

Furthermore, in order to describe a more accurate dynamic model, the back-diffusion of water from the cathode to the anode can be defined with $H_2O_{v,back} = \gamma \cdot H_2O_{v,mbr}$ [5]. The back-diffusion coefficient β is measured as $6 \times 10^{-6} (cm^2 / s)$ with the water content being $\lambda_m = 14$ [5]. The flow rates of liquid water leaving the anode and cathode are given by $H_2O_{l,Aout}$ and $H_2O_{l,Cout}$, which are dependent upon the saturation state of each gas [7]. To estimate the liquid water, the maximum mass of vapor has to be calculated from the vapor saturation pressure as follows:

$$m_{v,\max,A \text{ or C}} = \frac{p_{vs} V_{A \text{ or C}}}{R_v T_{st}}. \tag{2-16}$$

The saturation pressure p_{vs} is calculated from an equation presented in [30]:

$$\log_{10}(p_{vs}) = -1.69 \times 10^{-10} T^4 + 3.85 \times 10^{-7} T^3 - 3.39 \times 10^{-4} T^2 + 0.143T - 20.92 \tag{2-17}$$

where the saturation pressure p_{vs} is in kPa and temperature T is in Kelvin. If the mass of water calculated in Equation (2-15a) and (2-15b) is greater than the maximum mass of vapor in Equation (2-16), the liquid water formation occurs simultaneously. The mass of liquid water and vapor is calculated by follows [7]:

Logic 1:

if $m_{w,A \text{ or C}} \le m_{v,\max A \text{ or C}} \rightarrow m_{v,A \text{ or C}} = m_{w,A \text{ or C}}$, $m_{l,A \text{ or C}} = 0$;

if $m_{w,A \text{ or C}} > m_{v,\max A \text{ or C}} \rightarrow m_{v,A \text{ or C}} = m_{v,\max A \text{ or C}}$

$m_{l,A \text{ or C}} = m_{w,A \text{ or C}} - m_{v,\max A \text{ or C}}$.

Thereby, $\beta_{A\,\mathrm{or\,C}}$ can be used to estimate the liquid water formation in Equation (2-18). According to logic 1, if $m_{w,A\,\mathrm{or\,C}} \le m_{v,\max A\,\mathrm{or\,C}}$, then $\beta_{A\,\mathrm{or\,C}} = 0$, otherwise $\beta_{A\,\mathrm{or\,C}} = 1$, and therefore $H_2O_{l,Aout}$ and $H_2O_{l,Cout}$ are defined by

$$H_2O_{l,A\,\mathrm{or\,C}\,out} = \beta_{a\,\mathrm{or\,c}} \left| \frac{p_{H_2O_{A\,\mathrm{or\,C}}} V_{A\,\mathrm{or\,C}}}{\mathrm{R_v} T_{st}} - \frac{p_{\mathrm{vs}} V_{A\,\mathrm{or\,C}}}{\mathrm{R_v} T_{st}} \right| / M_{H_2O} \tag{2-18}$$

where M_{H_2O} is the water molar mass, 18.02 g/mol. All units of flow rates, usages, and the production of gases are defined as mol s^{-1}. However, because the liquid water is considered based on our assumption that each relative humidity stays over 100%, $\beta_{a\,\mathrm{or\,c}}$ will be 1, which means that $p_{H_2O_{A\,\mathrm{or\,C}}} > P_{vs}$ during the simulation. V_a, and V_c are the anode and cathode volumes, respectively, and their units are m^3. According to the basic electrochemical relationships, the usage and production of the gases are functions of the cell current density I_{fc} [1], as follows:

$$H_{2used} = 2O_{2used} = H_2O_{Cproduced} = \frac{N \cdot A_{fc} \cdot I_{fc}}{2F} \tag{2-19}$$

For simplicity, let us define

$\frac{N \cdot A_{fc}}{2F} = C_1$, and $1.2684 \frac{N \cdot A_{fc}}{F} = C_2$.

Thus, in Equations (2-15a) and (2-15b), H_2O_{mbr} and $H_2O_{v,back}$ can be simplified with C_1 and C_2. With the measured inlet flow rates and the stack current, the outlet flow rates are given by the summation of the anode and cathode inlet flow rates—that is, $Anode_{in}$ and $Cath_{in}$, minus the usage and production of gases as well as the pressure fraction

proposed by [20]. The $Anode_{in}$ is defined by $H_{2in} + H_2O_{Ain}$, and the $Cath_{in}$ is defined by $O_{2in} + N_{2in} + H_2O_{Cin}$.

The outlet flow rates on the anode side are

$$\begin{aligned} H_{2out} &= (H_{2in} - C_1 \cdot I_{fc})F_{H_2} \\ H_2O_{Aout} &= (H_2O_{Ain} - C_2 \cdot I_{fc} + \gamma \cdot C_2 \cdot I_{fc})F_{H_2O_A} \end{aligned} \tag{2-20}$$

and the outlet flow rates on the cathode side are

$$\begin{aligned} O_{2out} &= (O_{2in} - \frac{C_1}{2} I_{fc})F_{O_2} \\ N_{2out} &= N_{2in} \cdot F_{N_2} \\ H_2O_{Cout} &= (H_2O_{Cin} + C_1 \cdot I_{fc} + C_2 \cdot I_{fc} - \gamma \cdot C_2 \cdot I_{fc})F_{H_2O_C} \end{aligned} \tag{2-21}$$

where $F_{H_2}, F_{H_2O_A}, F_{O_2}, F_{N_2}$, and $F_{H_2O_C}$ are the pressure fractions of gases inside the fuel cell, given as follows [17]:

$$F_{H_2} = \frac{P_{H_2}}{P_{H_2} + P_{H_2O_A}} \qquad F_{O_2} = \frac{P_{O_2}}{P_{O_2} + P_{N_2} + P_{H_2O_C}}$$

$$, \qquad F_{N_2} = \frac{P_{N_2}}{P_{O_2} + P_{N_2} + P_{H_2O_C}} \quad . \tag{2-22}$$

$$F_{H_2O_A} = \frac{P_{H_2O_A}}{P_{H_2} + P_{H_2O_A}} \qquad F_{H_2O_C} = \frac{P_{H_2O_C}}{P_{O_2} + P_{N_2} + P_{H_2O_C}}$$

To analyze the transient behavior of fuel cells, we take into account the pressure fraction of each gas proposed by L.Y. Chiu et al. [17]. In [17], only the three pressure fractions F_{H_2}, F_{O_2}, and $F_{H_2O_C}$ are considered, but in our study, by considering all pressure fractions of gases, a more accurate dynamic fuel cell model is achieved and a better analysis of the transient behavior of fuel cells is possible than in previous studies [6, 7,

11, 17]. The state Equations (2-23) and (2-24) are obtained by substituting Equations (2-20) and (2-22) into Equations (2-15a) and (2-15b).

The new state equations on the anode side are

$$\begin{aligned}\frac{dP_{H_2}}{dt} &= \frac{RT}{V_A}\left[H_{2in} - C_1 \cdot I_{fc} - (H_{2in} - C_1 \cdot I_{fc})F_{H_2}\right] \\ \frac{dP_{H_2O_a}}{dt} &= \frac{RT}{V_A}\left[H_2O_{Ain} - (H_2O_{Ain} - C_2 \cdot I_{fc} + C_2 \cdot I_{fc})F_{H_2O_A} - C_2 \cdot I_{fc} + \gamma \cdot C_2 \cdot I_{fc}\right]\end{aligned} \tag{2-23}$$

and the state equations on the cathode side are

$$\begin{aligned}\frac{dP_{O_2}}{dt} &= \frac{RT}{V_C}\left[O_{2in} - \frac{C_1}{2} I_{fc} - (O_{2in} - \frac{C_1}{2} I_{fc})F_{O_2}\right] \\ \frac{dP_{N_2}}{dt} &= \frac{RT}{V_C}\left[N_{2in} - N_{2in} \cdot F_{N_2}\right] \\ \frac{dP_{H_2O_C}}{dt} &= \frac{RT}{V_C}\left[H_2O_{Cin} + C_1 \cdot I_{st} - (H_2O_{Cin} + C_1 \cdot I_{st} + C_2 \cdot I_{st} - C_2 \cdot I_{st})F_{H_2O_C} + C_2 \cdot I_{st} - \gamma \cdot C_2 \cdot I_{st}\right]\end{aligned} \tag{2-24}$$

Because the initial mole fractions Y_{H_2}, Y_{O_2}, and Y_{N_2} are set to be 0.99, 0.21, and 0.79, respectively [6, 7, 11], the input values H_{2in}, O_{2in}, and N_{2in} are defined by the mole fractions, which are given as

$$\begin{aligned} H_{2in} &= Y_{H_2} \cdot Anode_{in} \\ O_{2in} &= Y_{O_2} \cdot Anode_{in} \\ N_{2in} &= Y_{N_2} \cdot Cath_{in} \end{aligned} \tag{2-25}$$

The water inlet flow rates on the anode and the cathode are expressed in terms of the relative humidity, saturation pressure, and total pressure on each side, as follows [5].

$$\begin{aligned} H_2O_{Ain} &= \frac{\varphi_a P_{vs}}{P_A - \varphi_a P_{vs}} \cdot Anode_{in} \\ H_2O_{Cin} &= \frac{\varphi_c P_{vs}}{P_C - \varphi_c P_{vs}} \cdot Cath_{in} \end{aligned}, \tag{2-26}$$

where φ_a and φ_c are the relative humidity on the anode and the cathode sides, respectively; $P_A = P_{H_2} + P_{H_2O_A}$ is the summation of partial pressures of the anode; and $P_C = P_{O_2} + P_{N_2} + P_{H_2O_C}$ is the summation of partial pressures of the cathode. P_{vs} is the saturation pressure, which can be found in the thermodynamics tables [31]. The relative humidity φ_a and φ_c are defined from the water injection input u_{a_h} for the anode, and u_{c_h} for the cathode. Furthermore, $Anode_{in}$ and $Cath_{in}$ are defined as the products of the input control variables u_a and u_c and the conversion factors k_a and k_c [11, 24] on each side, which are translated from standard litres per minute (SLPM) to mols^{-1}. In other words:

$$\begin{aligned} Anode_{in} &= u_a \cdot k_a \\ Cath_{in} &= u_c \cdot k_c \end{aligned}, \tag{2-27}$$

where the conversion factors k_a and k_c are 0.065 mol s^{-1}, respectively. The hydrogen and the air stoichiometric ratios are assumed to be constant to keep the reactants flowing through the stack [31]. Hence, both of these reactants are able to be fed to the fuel cell continuously, and the fuel cell control system can be mainly dependent upon the input control variables u_a and u_c. First, the anode gas pressure $P_a = P_{H_2} + P_{H_2O_A}$ and the cathode gas pressure $P_c = P_{N_2} + P_{O_2} + P_{H_2O}$ will be controlled by u_a and u_c,

respectively, to avoid an unwanted pressure fluctuation and prevent membrane electrode assembly (MEA) damage, thus it can lead to prolong the fuel cell stack life [28]. In terms of control for the relative humidity on both sides, the first-order time-delay water injection inputs u_{a_h} and u_{c_h} will be applied because the water injection system has a very slow time constant τ_d of about 70 sec [26]. Thus, in our dynamics model of PEMFC the first-order time-delay model for the water injection is considered and the state equation from the relationship between the water injection input and relative humidity is derived as follows:

$$\varphi_a = \frac{1}{1+\tau_d s} u_{a\_\mathrm{h}}; \qquad \varphi_b = \frac{1}{1+\tau_d s} u_{b\_\mathrm{h}} \tag{2-28}$$

where φ is a relative humidity. As seen in Equation (2-26), because each water input is a function of humidity, the water injection inputs also affect the pressure controls. So, we can establish a dynamic model of PEMFCs and the details of control design will be described in the next chapter.

CHAPTER 3

CONTROL OF PEM FUEL CELLS SYSTEMS

3.1 Introduction

As mentioned in Chapter 1, since PEM fuel cells system model is involved in a nonlinear relationship, existing linear fuel cell models [7, 8, 10, 11, 17, 18] may not be suitable to achieve a satisfactory dynamic performance for all operating points. Furthermore, even though it is inevitable to exist the liquid water in the fuel cell operation, many studies [7, 8, 10, 11, 17, 18] regarding dynamic modeling and the control of PEMFC have not considered all possible water components, but assumed that the liquid water does not leave the stack and evaporate into gas. By doing so, only vapor water components are reflected in the dynamic modeling of PEMFC. Thereby [7, 8, 10, 11, 17], since the time delays of fuel cell voltage output, and the water injection for humidity control are not accurately modeled as well as eliminating the liquid water, it is difficult to investigate the dynamic performance of fuel cell systems. In the study [27], due to the relative degree, the internal dynamic problem can not be solved until the simulation results show that all states lie in boundaries in order to reduce the pressure difference between the anode and cathode. Thus, in this study, by introducing time delay constants in the fuel cell control systems and establishing all possible water effects in the fuel cell, the internal dynamics problem can be solved but also a more accurate nonlinear dynamic PEMFC model can be presented. Therefore, a nonlinear

control design technique that takes into consideration the nonlinearity of PEMFC is proposed and tested in Matlab Simulink™ environment. It is expected to perform fast transient responses under load variations. Here, a nonlinear controller using feedback linearization based on the proposed nonlinear dynamic fuel cell model is employed to achieve more robust transient behaviors than linear controllers. Furthermore, the fuel cell stack life can be prolonged and stack systems can be protected by minimizing the deviations between the anode and cathode partial pressures through the proposed nonlinear controller [7, 32].

In last few years, feedback linearization for nonlinear dynamic models has been widely used [27, 33-36]. Feedback linearization uses a nonlinear transformation to transform an original nonlinear dynamic model into a linear model by diffeomorphism mapping [27, 33–36]. An optimal control theory is also applied to obtain a linear control that is transformed back to the original space by using the nonlinear mapping.

In this chapter, based on the new dynamic nonlinear model in Chapter II, the proposed controller, which is expected to perform rapid transient responses under load variations, is tested in MATLAB /Simulink environment.

With respect to temperature control, even though the temperature has a large effect on the performance of the fuel cell system, the control strategy for temperature so far does not exist. In the existing control approaches for PEMFCs [7, 8, 10, 11, 17, 18], because the temperature of PEMFCs has a slow dynamics comparing with other parameters like air and pressure, the stack temperature is assumed to be constant so that a simplified control oriented dynamic model was derived. However, in reality, the

change of the stack temperature dramatically affects the output power as well as the pressures of the fuel cells system. In order to achieve a better quality of output current and larger output power, a controlled oriented new thermal equivalent circuit of PEMFC is proposed in Chapter 2. According to this thermal model, a temperature control algorithm for PEMFC is developed and analyzed.

Chapter 3 is organized as follows: Section 3.2 gives a brief introduction to feedback linearization. Section 3.3 addresses the design of a nonlinear controller for PEMFCs and provides the simulation results for the proposed controller. In section 3.4, the design of PEMFC temperature controller is presented and analyzed through the Matlab/Simulink simulation.

3.2 Nonlinear Control by Feedback Linearization

For decades, a significant progress has been made in control designs based on nonlinear concepts. In particular, nonlinear control theory developed from differential geometry, known as exact linearization or feedback linearization, has become more and more attractive for chemical process control because many chemical processes are basically of high nonlinearity [33, 34]. Hence, one of the main motivations of utilizing feedback linearization for the fuel cell system is that the operation of PEMFC is inherently a nonlinear chemical process. In this section, feedback linearization of nonlinear systems is briefly introduced. More details of nonlinear control based on differential geometry are available in [34-37].

Consider a single-input single-output (SISO) nonlinear system described by the following state equation:

$$\begin{aligned} x &= f(x) + g(x)u \\ y &= h(x) \end{aligned} \tag{3-1}$$

where x is an n-dimensional state vector that is assumed to be measurable, u is a scalar input, and y is a scalar output.

The objective of feedback linearization is to create a linear differential relation between the output y and a newly defined input v. The notation and concepts of differential geometry are essential to understand this approach. The Lie derivative of a scalar function $h(x)$ with respect to a vector function $f(x)$ is defined as

$$L_f h(x) = \nabla h \cdot f = \frac{\partial h(x)}{\partial x} f(x) \tag{3-2}$$

Repeated Lie derivatives can be defined recursively as

$$\begin{aligned} L_f^k h(x) &= L_f (L_f^{k-1} h) = \nabla (L_f^{k-1} h) \cdot f \\ L_f^0 h(x) &= h(x) \end{aligned} \tag{3-3}$$

for $k = 1,2,\ldots$

Similarly, in case of another vector field g,

$$L_g L_f h = \nabla (L_f h) g \, . \tag{3-4}$$

The output needs to be differentiated for r times until it is directly related to the input u. The number r is called the relative degree of the system.

The system is said to have a relative r at a point x_0 if

(1) $L_g L_f^k h(x) = 0$ for all x in the neighborhood of x_0 and

for $k < r-1$

(2) $L_g L_f^{r-1} h(x_0) \neq 0$.

Thus, according to the above condition, with a defined relative degree, the r time derivatives of y are described as

$$y^{(k)} = L_f^k(x)h(x) \qquad \text{for } k = 0,1,\ldots,r-1$$

$$y^{(r)} = L_f^r(x)h(x) + L_g L_f^{r-1} h(x)u\,. \tag{3-5}$$

The control law is

$$u = \frac{1}{L_g L_f^{r-1} h(x)}(-L_f^r h(x) + v) \tag{3-6}$$

where $y^{(r)} = v$. This control law can transform the nonlinear system into a linear one. Esides, a nonlinear transformation of a coordinate in the state space

$$z = \phi(x) \tag{3-7}$$

is called a local diffeomorphism in which the map between the new input v and the output is exactly linear for all x in the neighborhood of x_0.

This feedback linearization theory can be used to design multiple–input, multiple-output (MIMO) nonlinear system:

$$\begin{aligned} \dot{x} &= f(x) + \sum_{i=1}^{m} g_i(x) u_i \\ y_i &= h(x), \qquad i = 1,2,\ldots,m \end{aligned} \tag{3-8}$$

where x is an n-dimensional state vector and u and y are m-dimensional input and output vectors. The system is said to have a vector relative degree $\{r_1, r_2, \cdots, r_m\}$ at a point x_0 if

(1) $L_{g_j} L_f^k h_i(x) = 0$ for all $1 \le j \le m$, all $1 \le i \le m$ and

$k < r_i - 1$, and for all x in the neighborhood of x_0

(2) The $m \times m$ matrix

$$A(x) = \begin{bmatrix} L_{g_1} L_f^{r_1 - 1} h_1(x) & \cdots & L_{g_m} L_f^{r_1 - 1} h_1(x) \\ \vdots & \cdots & \vdots \\ L_{g_1} L_f^{r_m - 1} h_m(x) & \cdots & L_{g_m} L_f^{r_m - 1} h_m(x) \end{bmatrix} \tag{3-9}$$

is nonsingular at $x = x_0$, which is called as a decoupling matrix.

Based on the defined relative degree, the control law of a MIMO nonlinear system is defined as

$$u = -A^{-1}(x) b(x) + A^{-1}(x) v \tag{3-10}$$

where

$$b(x) = \begin{bmatrix} L_f^{r_1} h_i(x) \\ \vdots \\ L_f^{r_m} h_m(x) \end{bmatrix} \qquad v = \begin{bmatrix} v_1 \\ \vdots \\ v_m \end{bmatrix} = \begin{bmatrix} y_1^{(r_1)} \\ \vdots \\ y_1^{(r_m)} \end{bmatrix}$$

Note that the control law in Equation (3-10) transforms the nonlinear system into a linear one in which the above input-output relation is linearized and decoupled. In this research, feedback linearization for a MIMO nonlinear system is utilized due to the MIMO dynamic nonlinear model of PEMFC.

3.3 Nonlinear Control of MIMO PEMFCs

In this section, a MIMO dynamic nonlinear model of PEMFCs is derived from Equations (2-18) and (2-23) and feedback linearization is utilized to design a nonlinear controller in order to control the anode and cathode gas pressures, humidity, and the stack voltage. Also, each relative humidity state can be defined by the first-order time-delay water injection inputs on both sides, and the state equation for the voltage control can be derived from the first-order dynamic model in Equation (2-5). According to the study [28], since only hydrogen and oxygen partial pressures are controlled to minimize the pressure difference between the anode and cathode, the system is unobservable and the internal dynamics problem is exposed. Thus, the other states—nitrogen and water partial pressures from the anode and cathode—were not controlled but were checked in bounded states through the simulation. However, in the proposed MIMO model, by choosing P_A, P_C , V_{st} , φ_a , and φ_b as the outputs, and with four inputs $u_a, u_c, u_{a\_h}, u_{c\_h}$ and with the fuel cell current density I_{fc} being considered an input as well [17], the internal dynamics problem of this MIMO PEMFC model can be solved as follows. The nonlinear dynamic system model of PEMFC is written as:

$$\dot{X} = f(x) + g_1(x)u_1 + g_2(x)u_2 + g_3(x)u_3 + g_4(x)u_4 + g_5(x)u_5 \tag{3-11}$$

$$\begin{bmatrix} y_1 \\ y_2 \\ y_3 \\ y_4 \\ y_5 \end{bmatrix} = \begin{bmatrix} x_1 + x_2 \\ x_3 + x_4 + x_5 \\ x_7 \\ x_8 \\ V_{st} \end{bmatrix} = \begin{bmatrix} h_1(x) \\ h_2(x) \\ h_3(x) \\ h_4(x) \\ h_5(x) \end{bmatrix}, \quad \text{where} \quad X = \begin{bmatrix} P_{H_2} \\ P_{H_2O_A} \\ P_{O_2} \\ P_{N_2} \\ P_{H_2O_C} \\ V_{fc} \\ \varphi_a \\ \varphi_b \end{bmatrix} = \begin{bmatrix} x_1 \\ x_2 \\ x_3 \\ x_4 \\ x_5 \\ x_6 \\ x_7 \\ x_8 \end{bmatrix}; \quad U = \begin{bmatrix} u_a \\ u_c \\ u_{a\_h} \\ u_{c\_h} \\ I_{fc} \end{bmatrix} = \begin{bmatrix} u_1 \\ u_2 \\ u_3 \\ u_4 \\ u_5 \end{bmatrix};$$

$$\mathrm{f}(x) = \begin{bmatrix} 0 \\ -\left|\mathrm{x}_2 - p_{vs}\right| / M_{H_2O} \\ 0 \\ 0 \\ -\left|\mathrm{x}_5 - p_{vs}\right| / M_{H_2O} \\ -x_6 / \tau_{fc} \\ -x_7 / \tau_d \\ -x_8 / \tau_d \end{bmatrix}; \quad \mathrm{g}_1(x) = RT \begin{bmatrix} \dfrac{k_a \cdot Y_{H_2}}{V_A} - \dfrac{k_a}{V_A} \dfrac{x_1}{x_1 + x_2} \\ \dfrac{k_a \cdot x_7 \cdot p_{vs}}{V_A(x_1 + x_2 - x_7 \cdot p_{vs})} \cdot \dfrac{x_1}{(x_1 + x_2)} \\ 0 \\ \vdots \\ 0 \end{bmatrix};$$

$$\mathrm{g}_2(x) = RT \begin{bmatrix} 0 \\ 0 \\ \dfrac{k_c \cdot Y_{O_2}}{V_C} - \dfrac{k_c}{V_C} \dfrac{x_3}{x_3 + x_4 + x_5} \\ \dfrac{k_c \cdot Y_{N_2}}{V_C} - \dfrac{k_c}{V_C} \dfrac{x_4}{x_3 + x_4 + x_5} \\ \dfrac{k_c \cdot x_8 \cdot p_{vs}}{V_c(x_3 + x_4 + x_5 - x_8 \cdot p_{vs})} \cdot \dfrac{x_3 + x_4}{(x_3 + x_4 + x_5)} \\ 0 \\ \vdots \\ 0 \end{bmatrix}; \; g_3(x) = \begin{bmatrix} 0 \\ \vdots \\ 0 \\ \dfrac{1}{\tau_d} \\ 0 \end{bmatrix}; \; g_4(x) = \begin{bmatrix} 0 \\ \vdots \\ 0 \\ 0 \\ \dfrac{1}{\tau_d} \end{bmatrix};$$

$$g_5(x) = RT \begin{bmatrix} -\frac{C_1}{V_A} + \frac{C_1 \cdot x_1}{V_A(x_1 + x_2)} \\ \frac{C_2 \cdot x_2}{V_A(x_1 + x_2)} - \frac{C_2}{V_A} + \frac{\gamma \cdot C_2}{V_A} \\ -\frac{C_1}{2V_C} + \frac{C_1 \cdot x_3}{2V_C(x_3 + x_4 + x_5)} \\ 0 \\ \frac{C_1}{V_C} - \frac{C_1 \cdot x_5}{V_C(x_3 + x_4 + x_5)} - \frac{C_2 \cdot x_5}{V_C(x_3 + x_4 + x_5)} + \frac{C_2}{V_C} - \frac{\gamma \cdot C_2}{V_C} \\ V_{st} / \tau_{fc} \\ 0 \\ 0 \end{bmatrix}$$

Equation (3-11) implies that the input-output behavior of the system is nonlinear and coupled. To apply the feedback linearization-based nonlinear control algorithm, the relative degree vector has to be checked such that the internal dynamics problem is avoided. Otherwise, the feedback linearization with $n < r$ (n: the system order, r: the sum of relative degree) renders the system partially linearized and decoupled [35, 36].

Without solving the internal dynamics issue, the tracking controller would be practically meaningless because the instability of the internal dynamics causes undesirable phenomena such as a poor response and critical damage to the system. Therefore, the relative degrees associated with the feedback linearization must be the same as the order of the system so that the nonlinear system is fully linearized and has a satisfactory controller.

According to Equation (3-11), the system order, *n,* is 8, and the relative degree vector with respect to the outputs $[r_1, r_2, r_3, r_4, r_5] = [2,2,1,1,2]$ because all control inputs show up after the second derivative of outputs y_1, y_2, and y_5, whereas in terms of

y_3 and y_4 the control inputs u_{a_h} and u_{c_h} appear through the first derivative of the output. Because the system order 8 is equal to the sum of the relative degrees, there is no internal dynamic problem, and the nonlinear system becomes fully linearized via feedback linearization. From Equation (3-11), a full-state MIMO nonlinear system is ready to develop a nonlinear control law. This condition renders the following control law [36, 38].

$$U = -A^{-1}(x)b(x) + A^{-1}(x)v \tag{3-12}$$

where $A(x) = \begin{bmatrix} L_{g_1} L_f^{r_1-1} h_1(x) & \cdots & L_{g_m} L_f^{r_1-1} h_1(x) \\ \vdots & \cdots & \vdots \\ L_{g_1} L_f^{r_m-1} h_m(x) & \cdots & L_{g_m} L_f^{r_m-1} h_m(x) \end{bmatrix}$,

where $b(x) = \begin{bmatrix} L_f^{r_1} h_i(x) \\ \vdots \\ L_f^{r_m} h_m(x) \end{bmatrix}$ $\quad v = \begin{bmatrix} v_1 \\ \vdots \\ v_m \end{bmatrix} = \begin{bmatrix} y_1^{(r_1)} \\ \vdots \\ y_1^{(r_m)} \end{bmatrix}$,

Once we have obtained a nonlinear control law that can not only compensate nonlinearities, but also decouple and linearize the input and output behaviors, we can impose the poles of the closed loop so that the outputs y_1 and y_2 track asymptotically the desired trajectory 3 atm by adding a proportional integral controller. In contrast, the other output humidity y_3 and y_4 and the fuel cell output voltage $y_5 = V_{st}$ are not usually considered as control objectives due to the slow time constant of the fuel cell system compared to electrical time constant, which is within a few millisecond during fast dynamics operation such as fast load change like acceleration or deceleration of the fuel cell vehicle.

Therefore, in our research, the main control objective is to control the pressures of anode and cathode gases. In other words, the transient responses of humidity and fuel cell voltage control through the feedback linearization are not useful in practice because the humidity responses react so slowly and the fuel cell voltage will be replaced with a secondary voltage source such as a battery or an ultra-capacitor if the fast transient response is required for fuel cell vehicle applications or other fast load change stationary applications. However, to investigate the dynamic performance of the fuel cell, such a control study taking into consideration the relative humidity and the fuel cell voltage might be very beneficial.

The decoupling matrix *A(x)* is defined as

$$A(x)=\begin{bmatrix} L_{g_1}L_f h_1 & 0 & 0 & 0 & L_{g_5}L_f h_1 \\ 0 & L_{g_2}L_f h_2 & 0 & 0 & L_{g_5}L_f h_2 \\ 0 & 0 & L_{g_3}h_3 & 0 & 0 \\ 0 & 0 & 0 & L_{g_4}h_4 & 0 \\ 0 & L_{g_2}L_f h_5 & 0 & 0 & L_{g_5}L_f h_5 \end{bmatrix} \tag{3-13}$$

which is nonsingular at $x = x_0$. In addition, the matrix parameters $b(x)$ and v in Equation (3-13) are given as follows:

$$b(x)=\begin{bmatrix} L_f^2 h_1(x) \\ L_f^2 h_2(x) \\ L_f^1 h_3(x) \\ L_f^1 h_4(x) \\ L_f^2 h_5(x) \end{bmatrix}; \qquad v=\begin{bmatrix} \ddot{y}_1 \\ \ddot{y}_2 \\ \dot{y}_3 \\ \dot{y}_4 \\ \ddot{y}_5 \end{bmatrix} \quad . \tag{3-14}$$

The control law given in Equation (3-12) yields decoupled and linearized input-output behavior (see Figure 3-11):

$$\begin{aligned} \ddot{y}_1 &= v_1 \\ \ddot{y}_2 &= v_2 \\ \dot{y}_3 &= v_3 \\ \dot{y}_4 &= v_4 \\ \ddot{y}_4 &= v_5 \end{aligned} \tag{3-15}$$

The outputs $y_1, \ldots, y_4$ and y_5 are decoupled in terms of the new inputs $v_1, \ldots, v_4,$ and v_5. Therefore, five linear subsystems are obtained. In order to ensure that each output is adjusted to the corresponding desired values, $y_{1\_s} = y_{2\_s} = 3[\text{atm}], y_{2\_s} = y_{4\_s} = 1.05,$ and $y_{5\_s} = V_{st}^*$. In terms of the fuel cell voltage, it can often vary based on the load change, and then it is difficult to define the reference voltage for the frequent load change though, V_{st}^* is set to 32 V to establish this control design. One of the stabilizing controllers is designed by a linear control theory using the pole placement strategy [36]. The new control inputs are given by:

$$\begin{bmatrix} v_1 \\ v_2 \\ v_3 \\ v_4 \\ v_5 \end{bmatrix} = \begin{bmatrix} \ddot{y}_{1\_S} - k_{11}\dot{e}_1 - k_{12}e_1 \\ \ddot{y}_{2\_S} - k_{21}\dot{e}_2 - k_{22}e_2 \\ \dot{y}_{3\_S} - k_{31}e_3 \\ \dot{y}_{4\_S} - k_{41}e_4 \\ \ddot{y}_{5\_S} - k_{51}\dot{e}_5 - k_{52}e_5 \end{bmatrix} \tag{3-16}$$

where $e_1, \ldots, e_4 = y_1 - y_{1\_S}, \ldots, y_4 - y_{4\_S}$ and $e_5 = y_5 - y_{5\_S}$. Even though the nonlinear system PEMFC is exactly linearized by the feedback linearization, there may exist a tracking error in the parameter variations, especially when there are frequent load

changes. To eliminate this tracking error, the integral terms are added in the closed-loop error equation, as in [34, 36]:

$$\begin{bmatrix} v_1 \\ v_2 \\ v_3 \\ v_4 \\ v_5 \end{bmatrix} = \begin{bmatrix} \ddot{y}_{1\_S} - k_{11}\dot{e}_1 - k_{12}e_1 - k_{13}\int e_1 \\ \ddot{y}_{2\_S} - k_{21}\dot{e}_2 - k_{22}e_2 - k_{23}\int e_2 \\ \dot{y}_{3\_S} - k_{31}e_3 - k_{32}\int e_3 \\ \dot{y}_{4\_S} - k_{41}e_4 - k_{42}\int e_4 \\ \ddot{y}_{5\_S} - k_{51}\dot{e}_5 - k_{52}e_5 - k_{53}\int e_5 \end{bmatrix} \tag{3-17}$$

From Equation (3-17), the error dynamics can be obtained as follows:

$$\begin{aligned} \dddot{e}_1 + k_{11}\ddot{e}_1 + k_{12}\dot{e}_1 + k_{13}e = 0 \\ \dddot{e}_2 + k_{21}\ddot{e}_2 + k_{22}\dot{e}_2 + k_{23}e = 0 \\ \ddot{e}_3 + k_{31}\dot{e}_3 + k_{32}e_3 = 0 \\ \ddot{e}_4 + k_{41}\dot{e}_4 + k_{42}e_4 = 0 \\ \dddot{e}_5 + k_{51}\ddot{e}_5 + k_{52}\dot{e}_5 + k_{53}e = 0 \end{aligned} \tag{3-18}$$

By appropriately choosing the desired pole of the characteristics of Equation (3-18) on the left half plane, the gains k_{ij} are calculated and asymptotic tracking control is achieved; that is, $x_1,\ldots,x_4 \to y_{1\_s},\ldots,y_{4\_s}$, and $x_5 \to y_{5\_s}$ as $t \to \infty$.

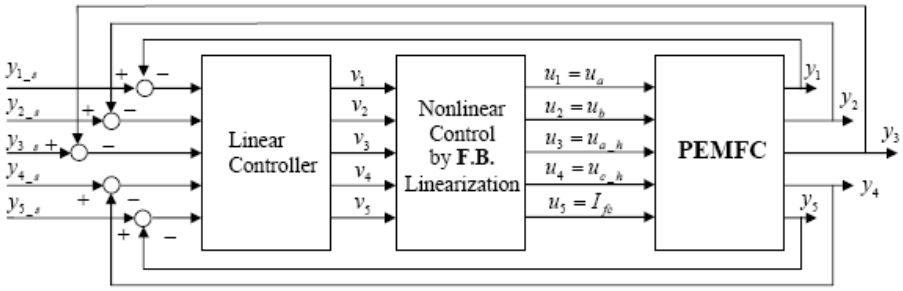

Figure 3.1 Overall control block diagram of PEMFC

As shown in Figure 3.1, the main objective of this control scheme is to design a nonlinear controller by appropriately defining a transformation mapping method that transforms the original nonlinear system into a linear and controllable closed system so that a linear controller can be designed by the pole placement technique for tracking purposes.

3.4 Model Validation and Simulation Results Regarding Nonlinear Control of MIMO PEMFC

This feedback linearization-based nonlinear control method has been applied to the proposed dynamic PEMFC model based on the Matlab-Simulink^{TM} environment. For the simulation, until now, only voltage and current data for the fuel cell have been available, and therefore the experimental data from J. Hamelin et al. [39] were used to justify the validity of the proposed dynamic model of PEM fuel cells. The corresponding stack current and voltage transients are plotted in Figure 3.2, where the experimental data [39] are indicated by solid lines. The details of load profile are shown in Figure 3.3. Due to a fast electrical response, the voltage and current data are almost the same as the results in [28]. However, because the anode and cathode partial pressure can be controlled, there is an obvious discrepancy between these pressure results and the data in [28]. To compare the efficiency of the proposed nonlinear feedback linearization controller (NFLC), the linear controller (PI) is also implemented for the fuel cell system.

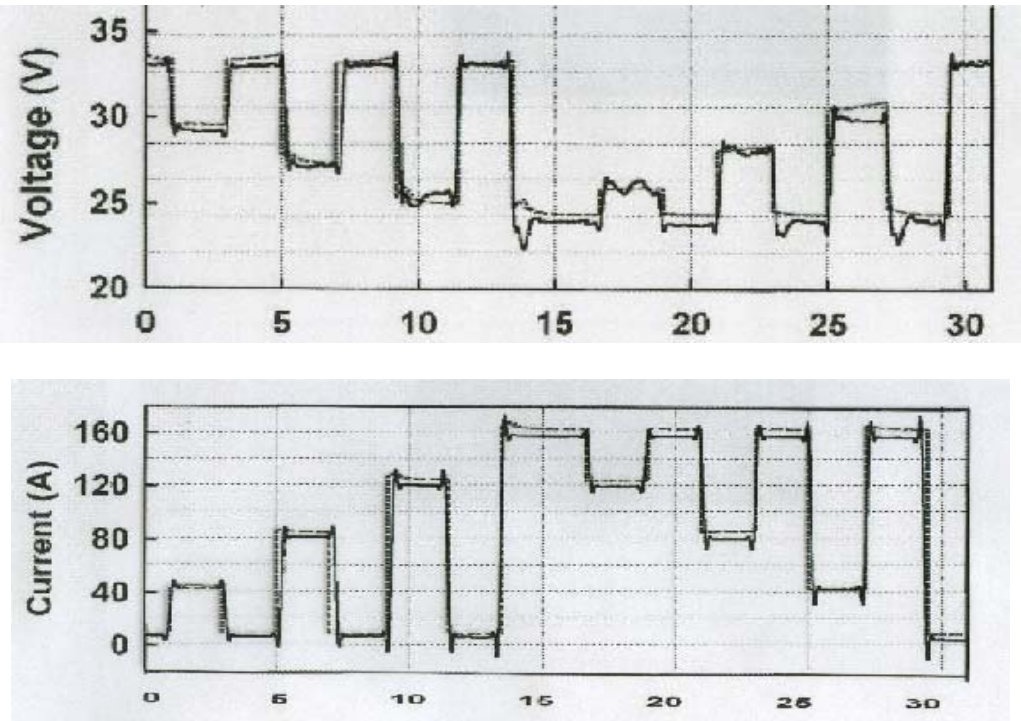

Figure 3.2 Voltage and current under load variations

The controller gains, especially $k_{11} \cdots k_{23}$, of Equation (3-18) were calculated from the desired poles, which are located on $s_{1,2} = -400 \pm i300$ and $s_3 = -70$ for the pressure control so that a lower number of overshoots may be achieved. The detailed description of controller gains for the humidity control and fuel cell voltage control will not be considered in our study because the development of these humidity and fuel cell voltage control algorithms might not be good for practical applications due to slow response of humidity and the use of a secondary power source for transient. In other words, in terms of fuel cell voltage control, because the fuel cell system cannot compensate for a fast power demand such as an acceleration and deceleration or other

fast load changes of the fuel cell vehicle without a secondary power source, the fuel cell voltage will be kept varying based on the load profile, as in [39].

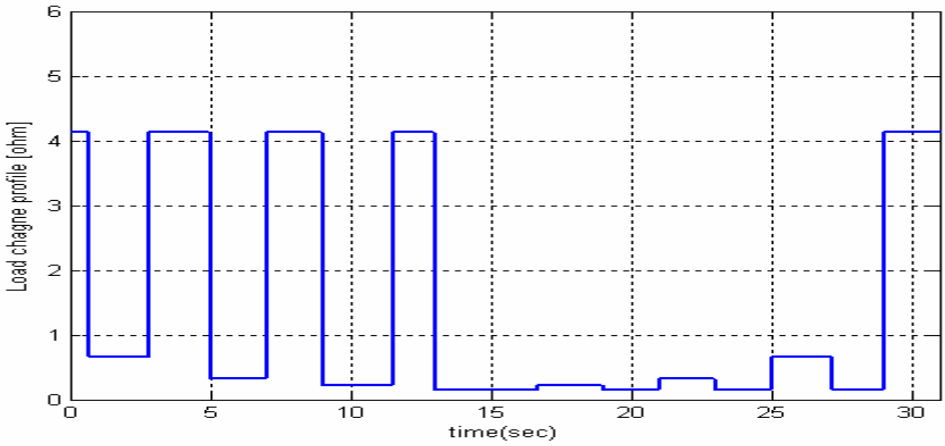

Figure 3.3 Load variation profile

For the voltage, current, and power, the discrepancies between the nonlinear control and the linear control are not obvious due to the fast response time, which is less than a few mili second, as in [28]. However, other simulation results in Figures 3.4–3.8 indicate that better transient performances are observed when a nonlinear controller is used because the PI controller not employing feedback linearization is more dependent upon the operating point, while the nonlinear controller is independent of the operating point due to the feedback linearization.

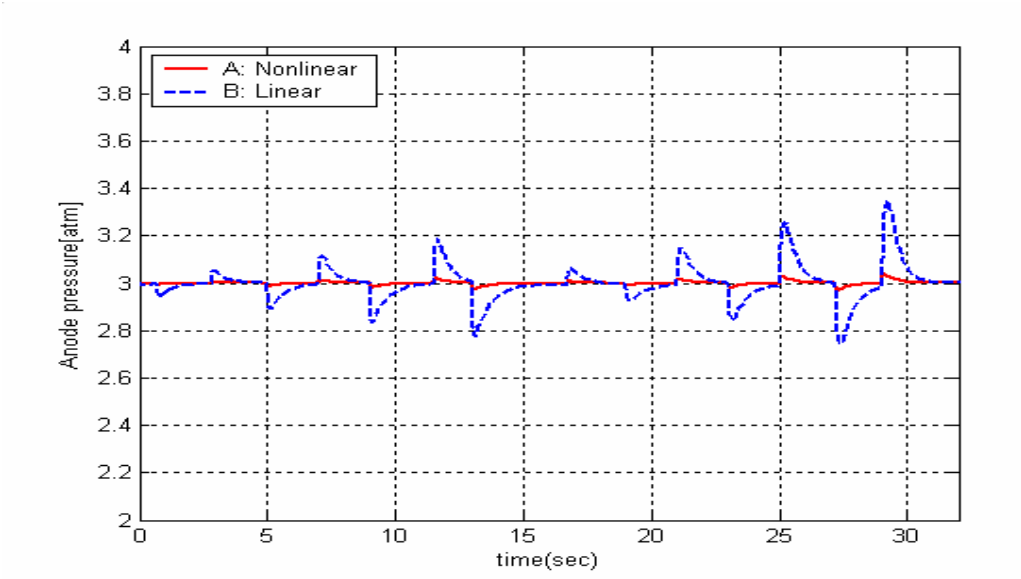

Figure 3.4 Variations of anode pressure

Figures 3.7 and 3.8 give the responses of the anode and the cathode flow rates under load variations. The anode flow rate and cathode flow rate are varied between 0 [slpm] to 5 [slpm], while the cathode flow rate varies from 0 [slpm] to 10 [slpm]. It can be seen that the cathode flow rate has much larger variations than those of the anode because the cathode flow rate is more sensitive to the load variation than is the anode flow rate. For this reason, a development of an optimal air management system related to the cathode flow rate is another hot topic in fuel cell control studies.

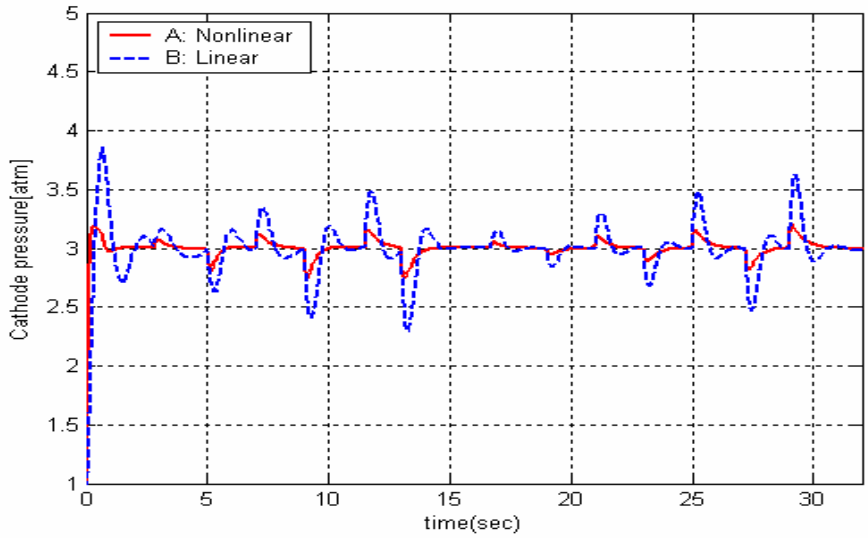

Figure 3.5 Variations of cathode pressure

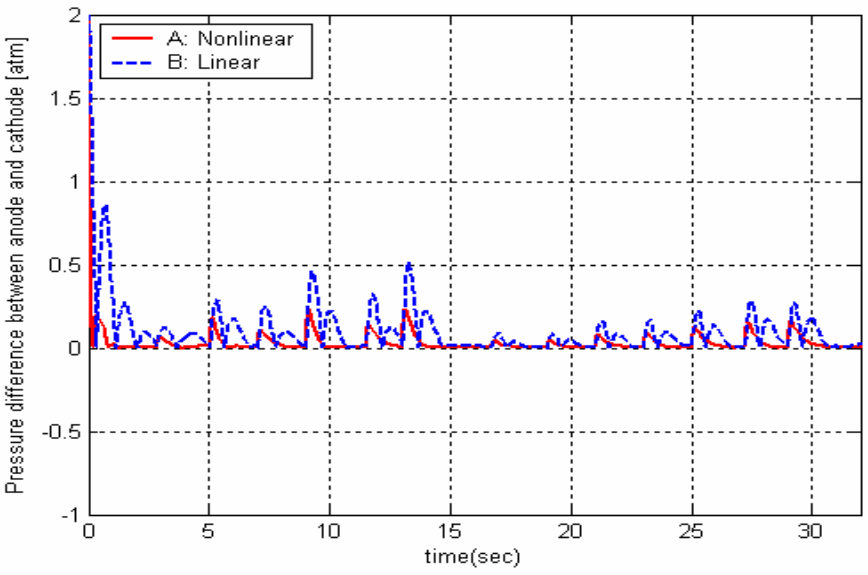

Figure 3.6 Pressure deviations between anode and cathode

In [28], the states $P_{H_2O_A}$, $P_{H_2O_c}$, and P_{N_2} are not controlled under the load variations but are simply checked for stability to see whether the state is bounded or not.

However, in our study the anode and cathode pressures are controlled, and thus the proposed nonlinear control can achieve a better dynamic response than the PI controller except for the relative humidity and fuel cell stack voltage. Figure 3.9 illustrates the relative humidity change. Due to the slow response time with regard to the relative humidity, with a time delay of 70 seconds, it changes very slowly over 150 seconds, as shown in Figure 3.9, and no specific discrepancy between the nonlinear control and the linear control for the relative humidity is observed.

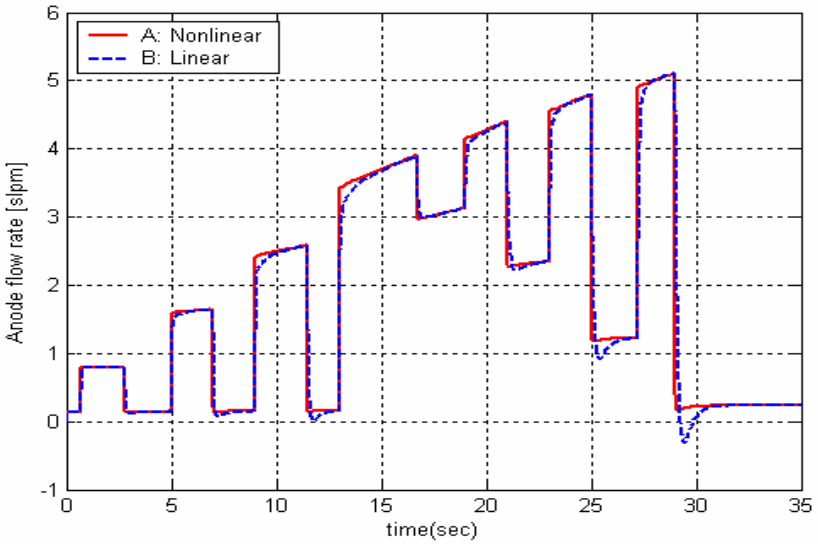

Figure 3.7 Variations of anode flow rate

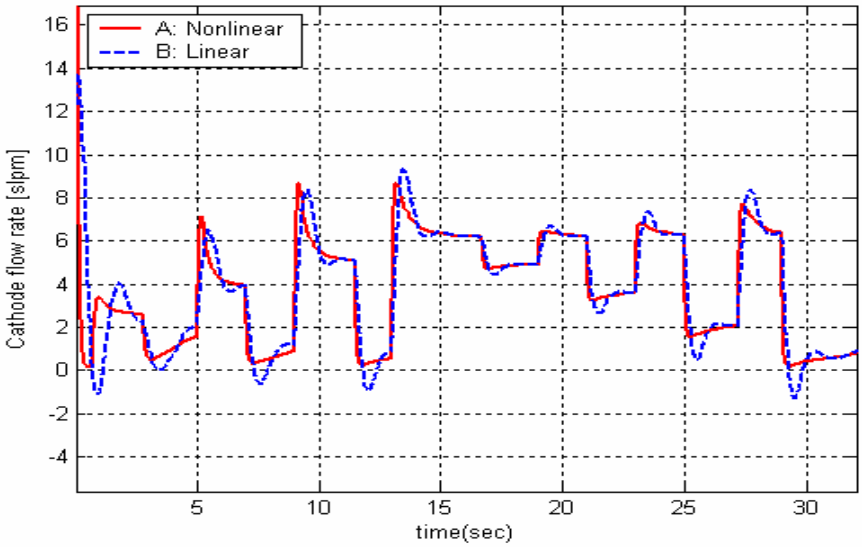

Figure 3.8 Variations of Cathode flow rate

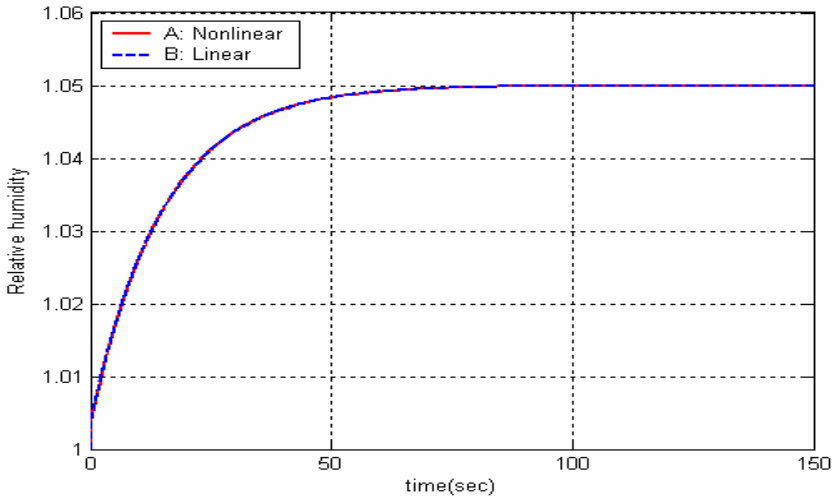

Figure 3.9 Variations of Relative humidity

3.5 Design of PEMFCs Temperature Controller

In Section 3.4, a MIMO PEMFCs model and nonlinear control algorithm for PEMFC have been proposed. However, the temperature controller was not considered in the model due to the long time constant. In here, the more details about temperature

controller will be presented and simulated using Matlab/Simulink modeling. In PEMFCs, the temperature $T_s(t)$ is a function of the fuel cell voltage V_{st}, the fuel cell current I_{fc}, the cooling pump control variable u_{cl} and other temperature values like ambient temperature T_{amb} ,which is assumed to be perturbed in the range of $\pm 5\%$ of current ambient temperature. In order to obtain a stable temperature under any disturbances, it is necessary to adjust the cooling pump control variable u_{cl} in the cooling system or heat exchanger. The typical open loop PEMFCs for the temperature control is illustrated in Figure 3.10. Because the voltage is dependent on the current in the fuel cell system, only two disturbances i_{fc} and t_{amb} can be considered. To adjust the u_{cl} automatically under any circumstances, the feedback control system [40] is utilized in Figure 3.11. The output stack temperature $t_s(t)$ is measured using a temperature sensor with gain $H(s)$. The sensor circuit is usually a voltage divider using high precision resistors. The sensor output signal $H(s)t_s(s)$ is compared with the reference input temperature $t_{ref}(s)$ and then the objective is to make $H(s)t_s(s)$ equal to $t_{ref}(s)$ so that $t_s(s)$ follows $t_{ref}(s)$ during disturbances in the system.

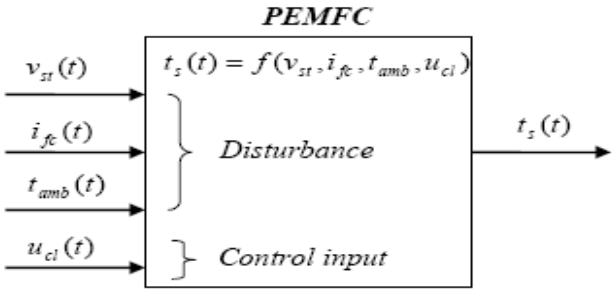

Figure 3.10 Open loop PEMFC for temperature control

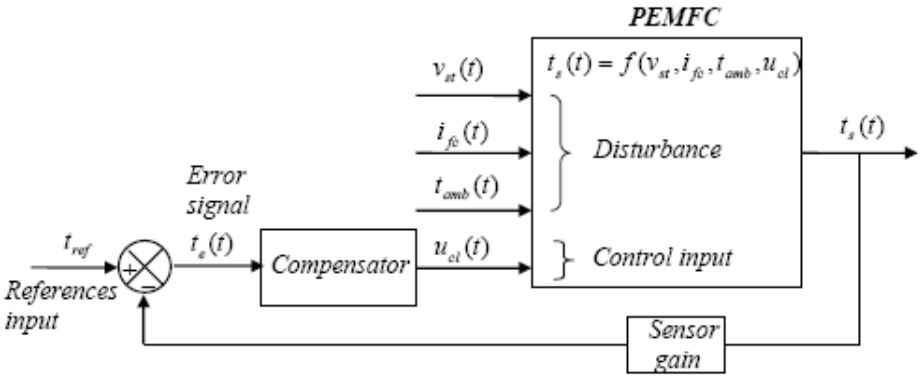

Figure 3.11 Feedback loop PEMFC for temperature control

We can derive a small signal ac network transfer functions of a thermal equivalent circuit by defining that $\hat{t}_s(t), \hat{i}_{fc}(t), \hat{t}_{amb}(t)$ and $\hat{u}_{cl}$ are small variations of each component [40]. According to the transient energy balance Equation (2-6) and Figure 3.10, the stack temperature variation can be expressed as follows

$$\hat{t}_s(s) = G_{ti}(s)\hat{i}_{fc}(s) - G_{tu}(s)\hat{u}_{cl}(s) + G_{tt}(s)\hat{t}_{amb}(s) \tag{3-19}$$

where

$G_{ti}(s) = \left.\dfrac{\dfrac{N}{2F}\Delta H - \hat{v}_{st}(s)}{sC_t + (1/R_t)}\right|_{\substack{\hat{u}_{cl}=0 \\ \hat{t}_{amb}=0}}$: fuel cell current to output thermal transfer function,

$G_{tu}(s) = G_d(s)/\left(sC_t + (1/R_t)\right)\big|_{\substack{i_{fc}=0 \\ t_{amb}=0}}$: control input to output transfer function in where

$G_d(s) = k_c/(1+\lambda_c s)$,

$G_{tt}(s) = \left(\hat{t}_{amb}(s)/R_t\right)/\left(sC_t + (1/R_t)\right)\big|_{\substack{\hat{i}_{fc}=0 \\ \hat{u}_{cl}=0}}$: ambient temperature to output transfer function.

To analyze this system, let us define the reference and error of the stack temperature perturbed as follows:

$$t_{ref}(t) = T_{ref} + \hat{t}_{ref}(t)$$
$$t_e(t) = T_e + \hat{t}_e(t) \tag{3-20}$$

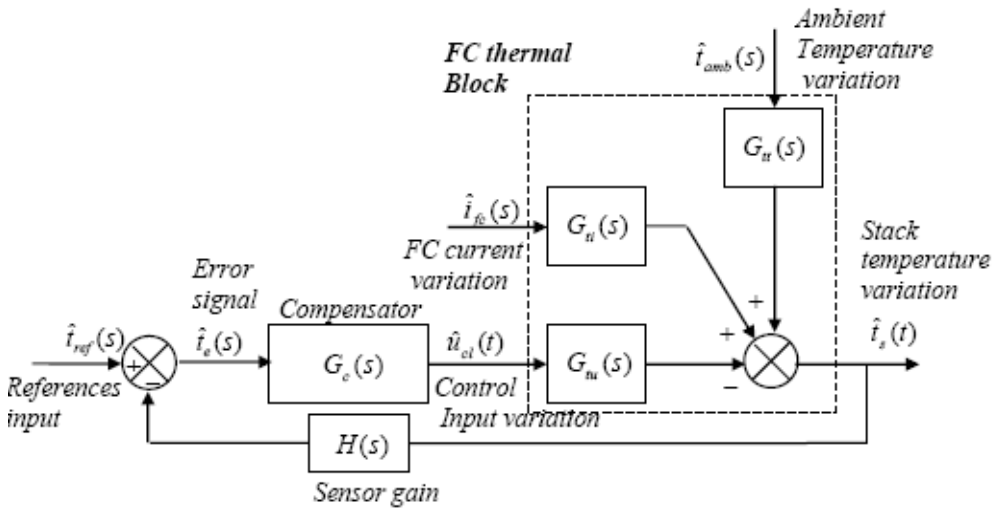

Figure 3.12 Complete Feedback loop PEMFC for temperature control

Using this small signal ac network transfer function of a thermal equivalent circuit, the PEMFCs block in Figure 3.11 can be replaced with the FC block described by Equation (3-19).

The output stack temperature variation $\hat{t}_s$ can be expressed as Equation (3-21):

$$\hat{t}_s = -\hat{t}_{ref}\frac{G_c G_{tu}}{1 + HG_c G_{tu}} + \hat{i}_{fc}\frac{G_{ti}}{1 + HG_c G_{tu}} + \hat{t}_{amb}\frac{G_{tt}}{1 + HG_c G_{tu}} \tag{3-21}$$

which can be rewritten by assuming that $L = HG_c G_{tu}$.

$$\hat{t}_s = -\hat{t}_{ref}\frac{1}{L}\frac{L}{1+L} + \hat{i}_{fc}\frac{G_{ti}}{1+L} + \hat{t}_{amb}\frac{G_{tt}}{1+L} \tag{3-22}$$

where $L(s) = H(s)G_c(s)G_{tu}(s)$

The loop gain *L(s)* in Equation (3-22) will be an important quantity to identify the system performance when a controller is adapted. Further detailed analysis of the loop gain is described in the following section.

3.5.1 Analysis of the PEMFCs Thermal Transfer Functions

To analyze a transfer function, in general, a Bode plot is used. First of all, the loop gain *L(s)* is constructed by the specific transfer function $H(s), G_c(s)$ and $G_{tu}(s)$ to plot the Bode plot. The loop gain *L(s)* is

$$L(s) = \frac{0.15}{\tau_s \tau_c C_t} \frac{\left(sk_p + k_i\right)}{s\left(s + \frac{1}{\tau_s}\right)\left(s + \frac{1}{\tau_c}\right)\left(s + \frac{1}{R_t C_t}\right)} \tag{3-23}$$

where $H(s) = \frac{0.1}{(1+\tau_s s)}$ is representing the sensor gain function with the sensor time delay 70 sec, which means, in case of 100^{o}C stack temperature, 10 V is used for the controller input and 0^{o}C is 0V as an input and the lag compensator G_c, PI controller with gain k_i and k_p, $G_c(s) = \frac{k_i + k_p s}{s}$ is used in Equation (3-23) because the lag compensator is used to increase a low frequency loop gain, which leads to a rejection of low frequency disturbance.

Normally, the variation of temperatures usually exists in the low frequency region. The Bode diagram of *L(s)* are illustrated in Figure 3.13 when the k_i is changed from 0.1 to 50 and k_p from 1 to 50. As seen in Figure 3.13, the small gains (k_i=0.1, k_p=1) are desired to make the system stable because the phase margin φ_L of the loop gain *L* is to be positive and the *L(s)* contains no right half plane pole.

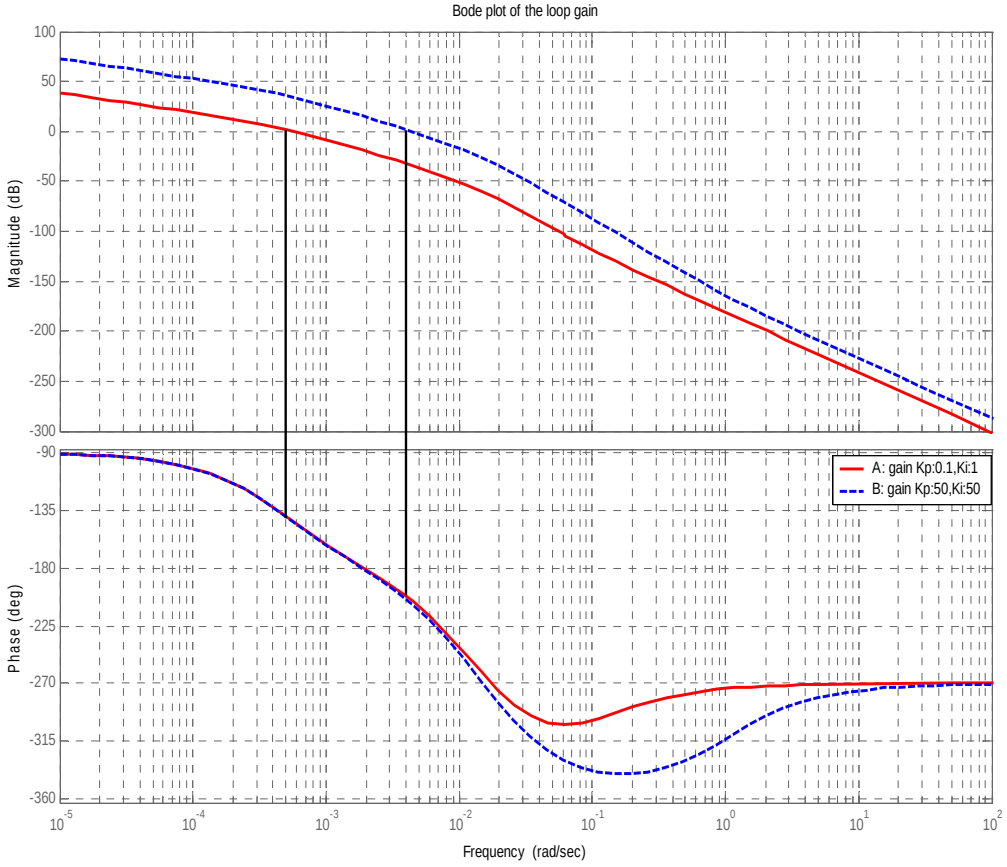

Figure 3.13 Bode plots of loop gain *L(s)* with lag compensator

So, the phase margin can be calculated by:

$$\varphi_L = 180^o + \angle L(2\pi f_c) \tag{3-24}$$

where f_c is the crossover frequency where the magnitude of the loop gain is unity:

$$\|T(j2\pi f_c)\| = 1 \Rightarrow 0 \text{ dB} \tag{3-25}$$

Hence, the phase margin of *L(s)* is approximately +40° in the case of the small gain of the lag compensator, i.e. k_i=0.1 and k_p=1. So, since the large gains (k_i=50, k_p=50) become the phase gain negative, the system with this large gain PI compensator makes the system unstable, which is absolutely not recommended.

3.5.2 Simulation Results of PEMFCs Temperature Controller

For the model verification, the experimental results (Ballard MK5-E) [9] by Amphlett et al are compared with our simulation results during the load step up condition. As shown in Figure 3.14, at 0 sec, the load step up change occurs based on the assumption that the start up times of the fuel cell is not considered, but in our works, at 2500 seconds after thermal time constant 2059 seconds mentioned in the chapter II, the load step up is imposed. For this step up condition, since the temperature is increased just from 40 to 60°C and the proposed temperature controller is designed so that operating fuel cell system temperature is within 80°C, this case does not need to activate a temperature controller. In Figure 3.14 [39], at 72°C, the better V-I polarization curve can be achieved but in high temperature, cooling system(temperature controller) should work to prevent degrading the fuel cell characteristics due to high thermal effects.

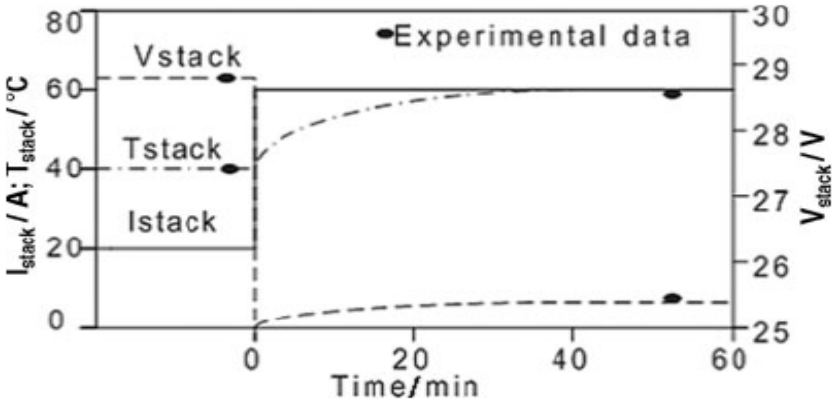

Figure 3.14 Load step up condition [9, 41]

In Figure 3.15, the simulation results are matched with the experiment results less 5 % error. Especially the thermal time constant (2,059 seconds) is almost same.

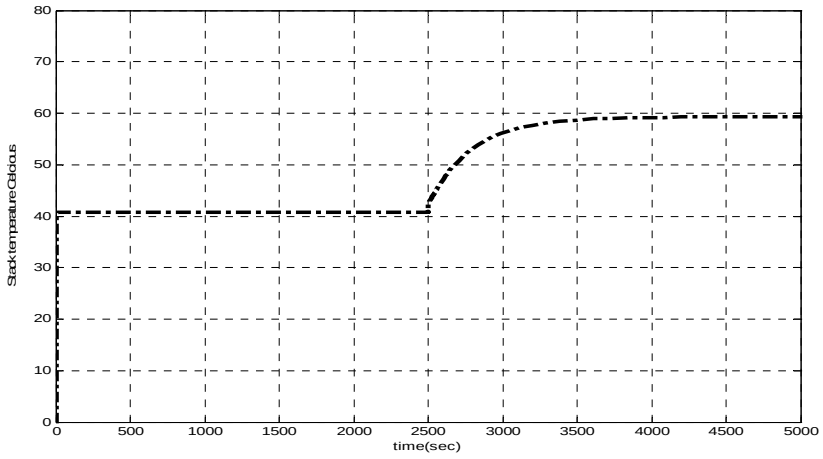

Figure 3.15 Temperature changes by using proposed model

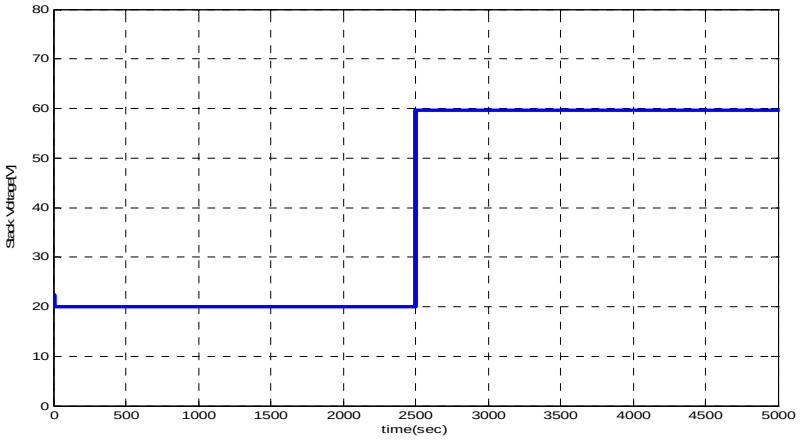

Figure 3.16 Stack Current changes by using proposed model

Simulated stack current changes in Figure 3.16 are almost equal to the experiment results [21], but the more stack voltage drops in Figure 3.14 is observed than the simulated voltage in Figure 3.17 because the practical fuel cell system exists more losses than the ideal fuel cell model in the simulation.

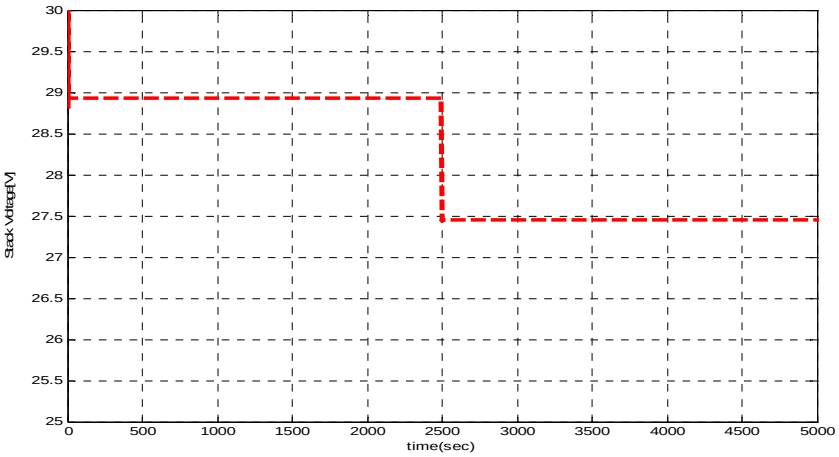

Figure 3.17 Stack Voltage changes by using proposed model

Up to date, data related to the fuel cell temperature controller are not available. Hence, using simulation results, a validity of the proposed temperature controller can be

estimated. During the sudden big load change from 20A to 190A as seen in Figure 3.19, the temperature changes can be found in Figure 3.18. As shown in Figure 3.18, the dotted line is temperature changes with no controller and the solid line is temperature changes with the proposed controller.

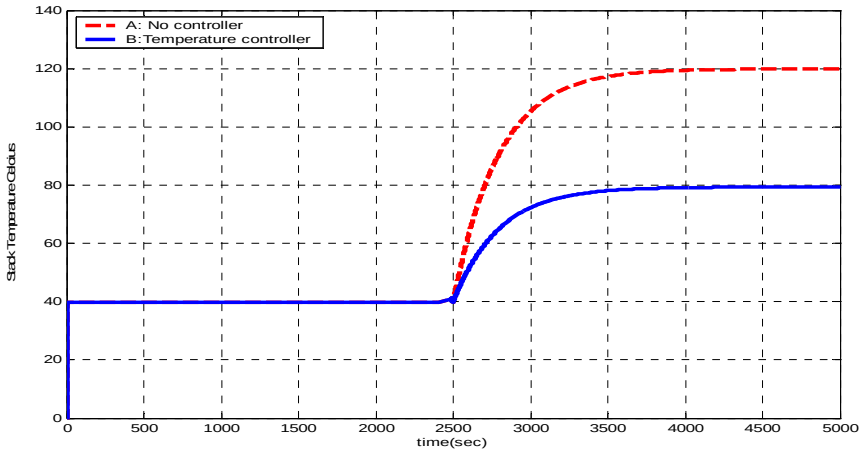

Figure 3.18 Temperature changes comparison

With the temperature controller, the operating temperature is limited to 80^{o}C, but without the controller the temperature is increased to 120^{o}C.

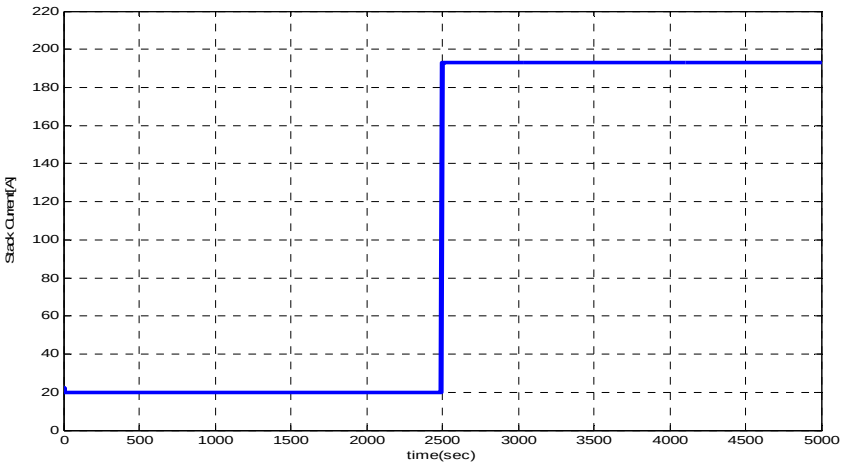

Figure 3.19 Stack Current changes (20A →190A)

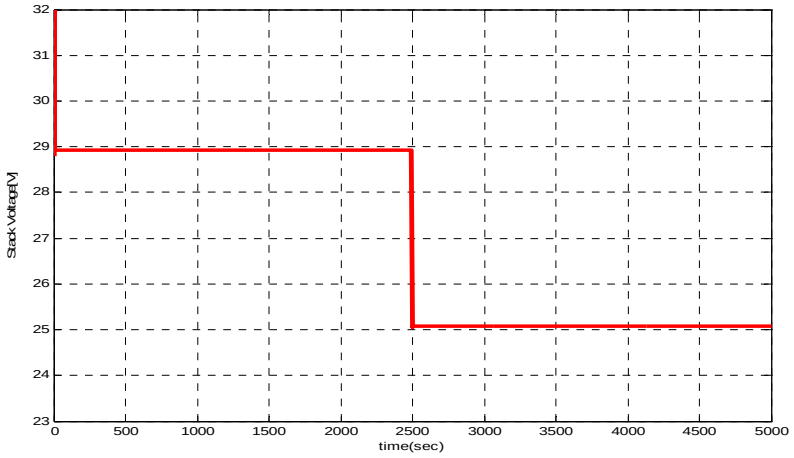

Figure 3.20 Stack Voltage changes

During this load change (20A →190A), the voltage drop can be observed to 25 V in the simulation. In practice, more voltage drop can be expected. The analysis for the design of the PEMFC temperature controller is performed by using Bode plots of the thermal equivalent circuit transfer functions. The Bode plots shows that lag compensator with small PI gains is a good option for the design of the temperature controller for PEMFC.

3.6 Nonlinear Control Design of PEMFCs with Inverter and Reformer

In this section, using a simplified multiple-input, single-output (MISO) PEMFC model, nonlinear control design of PEMFC with inverter and reformer is presented. Consider the following multiple-input, single-output nonlinear system:

$$\begin{aligned} \dot{x} &= f(x) + \sum_{i=1}^{m} g_i(x) u_i \qquad i = 1,2,...,m \\ y &= h(x) \end{aligned} \quad , \tag{3-26}$$

where $x \in X \subset R^n$ is the state, $u \in U \subset R^m$ is the input or control vector, and $y \in Y \subset R^P$ is the output vector of the system. Equations (3-27a) and (3-27b) imply the following simplified MISO nonlinear dynamic system model of PEMFCs by considering three partial pressures, pH_2, pO_2, and pH_2O_c :

$$\begin{bmatrix} \dot{x}_1 \\ \dot{x}_2 \\ \dot{x}_3 \end{bmatrix} = \begin{bmatrix} \frac{RT}{V_A}\left(1 - \frac{x_1}{p_{op}}\right) \\ 0 \\ 0 \end{bmatrix} u_1 + \begin{bmatrix} 0 \\ \frac{RT}{V_C}\left(1 - \frac{x_2}{p_{op}}\right) \\ -\frac{RT}{V_A \cdot p_{op}} x_3 \end{bmatrix} u_2 + \begin{bmatrix} \frac{RT}{V_C \cdot p_{op}}\left(-2K_r A_c + 2K_r A_c \times x_1\right) \\ \frac{RT}{V_C \cdot p_{op}}\left(-K_r A_c + 2K_r A_c \times x_2\right) \\ \frac{RT}{V_C \cdot p_{op}}\left(2K_r A_c - 2K_r A_c \times x_3\right) \end{bmatrix} u_3 \tag{3-27a}$$

$$y = V = N\left(E^0 + \frac{RT}{2F} \ln\left\{\frac{pH_2 (pO_2 / P_{std})^{0.5}}{pH_2O}\right\} - L\right) \tag{3-27b}$$

where

$$x = \begin{bmatrix} pH_2 & pO_2 & pH_2O_C \end{bmatrix}^T$$
$$u = \begin{bmatrix} H_{2\_in} & O_{2\_in} & i \end{bmatrix}^T$$
$$y = V$$

In the above nonlinear model, because the number of outputs is less than that of inputs, which means that the decoupling matrix for exact linearization is not square, the exact linearization approach for multiple-input, multiple output (MIMO) systems cannot be directly applied. The problem of non-square can be solved by using an extended system [36, 38]. In other words, additional states and outputs are chosen and added in such a way that a square system appears and the decoupling matrix is nonsingular.

One possible way to make the decoupling matrix square and nonsingular is to define *m-p* extra states:

$$\begin{aligned} \dot{x}_{n+1} &= u_{i_1} \\ &\vdots \\ \dot{x}_{n+m-p} &= u_{i_{m-p}} \end{aligned} \tag{3-28}$$

and to append the output vector with

$$\begin{aligned} y_{p+1} &= x_{n+1} \\ &\vdots \\ y_m &= x_{n+m-p} \end{aligned} \tag{3-29}$$

With the addition of two extra states, x_4 and x_5 , and two extra outputs, y_2 and y_3, MISO nonlinear system Equation (3-27a) and (3-27b) can be converted into a MIMO system described by Equation (3-30a) and (3-30b) as bellow so that the decoupling matrix is nonsingular.

$$\begin{bmatrix}\dot{x}_1\\ \dot{x}_2\\ \dot{x}_3\\ \dot{x}_4\\ \dot{x}_5\end{bmatrix}=\begin{bmatrix}\frac{RT}{V_A}(1-\frac{x_1}{p_{op}})\\ 0\\ 0\\ 0\\ 0\end{bmatrix}u_1+\begin{bmatrix}0\\ \frac{RT}{V_C}(1-\frac{x_2}{p_{op}})\\ -\frac{RT}{V_C}\frac{x_3}{p_{op}}\\ 1\\ 0\end{bmatrix}u_2+\begin{bmatrix}\frac{RT}{V_A}(-2K_rA_c+2K_rA_c\frac{x_1}{p_{op}})\\ \frac{RT}{V_C}(-K_rA_c+K_rA_c\frac{x_2}{p_{op}})\\ \frac{RT}{V_C}(2K_rA_c-2K_rA_c\frac{x_3}{p_{op}})\\ 0\\ 1\end{bmatrix}u_3 \qquad (3\text{-}30a)$$

$$\begin{bmatrix}y_1\\ y_2\\ y_3\end{bmatrix}=\begin{bmatrix}V\\ x_4\\ x_5\end{bmatrix}=\begin{bmatrix}h_1(x)\\ h_2(x)\\ h_3(x)\end{bmatrix}. \qquad (3\text{-}30b)$$

If decoupling matrix E(x) is nonsingular, the nonlinear state feedback control law can be obtained using Equation (3-31):

$$U=-E^{-1}\begin{bmatrix}L_f^{r_1}h_1(x)\\ \cdots\\ \cdots\\ L_f^{r_m}h_m(x)\end{bmatrix}+E^{-1}\begin{bmatrix}v_1\\ \cdots\\ \cdots\\ v_m\end{bmatrix} \qquad (3\text{-}31)$$

Where

$$E(x)=\begin{bmatrix}L_{g_1}L_f^{r_1-1}h_1 & \cdots & \cdots & L_{g_m}L_f^{r_1-1}h_1\\ \vdots & \vdots & \vdots & \vdots\\ \vdots & \vdots & \vdots & \vdots\\ L_{g_1}L_f^{r_1-1}h_m & \cdots & \cdots & L_{g_m}L_f^{r_m-1}h_m\end{bmatrix}. \qquad (3\text{-}32)$$

Since the relative degree for each input $u_1, u_2,$ and u_3 in Equations (3-30a) and (3-30b) is equal to 1, E(x) can be described by Equation (3-33)

$$E(x)=\frac{NR^2T^2}{2F}\begin{bmatrix} \frac{1}{V_A}\left(\frac{1}{x_1}-\frac{1}{p_{op}}\right) & \frac{1}{2V_C}\left(\frac{1}{x_2}-\frac{1}{p_{op}}\right)+\frac{1}{V_C p_{op}} & K_r A_C\left[\frac{2}{V_A}\left(-\frac{1}{x_1}+\frac{1}{p_{op}}\right)+\frac{1}{2V_C}\left(-\frac{1}{x_2}+\frac{1}{p_{op}}\right)-\frac{1}{V_C}\left(\frac{2}{x_3}-\frac{1}{p_{op}}\right)\right. \\ 0 & 1 & 0 \\ 0 & 0 & 1 \end{bmatrix} \quad (3\text{-}33)$$

$$E^{-1}(x)=\frac{2F}{NR^2T^2}\begin{bmatrix} \frac{V_A x_1 p_{op}}{p_{op}-x_1} & -\left[\frac{1}{2V_C}\left(\frac{1}{x_2}-\frac{1}{p_{op}}\right)+\frac{1}{V_C p_{op}}\right]*\left[\frac{V_A x_1 p_{op}}{p_{op}-x_1}\right] & -K_r A_C\left[\frac{2}{V_A}\left(-\frac{1}{x_1}+\frac{1}{p_{op}}\right)+\frac{1}{2V_C}\left(-\frac{1}{x_2}+\frac{1}{p_{op}}\right)-\frac{1}{V_C}\left(\frac{2}{x_3}-\frac{1}{p_{op}}\right)\right]*\left[\frac{V_A x_1 p_{op}}{p_{op}-x_1}\right] \\ 0 & 1 & 0 \\ 0 & 0 & 1 \end{bmatrix} \quad (3\text{-}34)$$

$$u_1=\frac{2F}{NR^2T^2}\left[\frac{V_A x_1 p_{op}}{p_{op}-x_1}v_1-\left[\frac{1}{2V_C}\left(\frac{1}{x_2}-\frac{1}{p_{op}}\right)+\frac{1}{V_C p_{op}}\right]*\left[\frac{V_A x_1 p_{op}}{p_{op}-x_1}\right]v_2+K_r A_C\left[\frac{2}{V_A}\left(-\frac{1}{x_1}+\frac{1}{p_{op}}\right)+\frac{1}{2V_C}\left(-\frac{1}{x_2}+\frac{1}{p_{op}}\right)-\frac{1}{V_C}\left(\frac{2}{x_3}-\frac{1}{p_{op}}\right)\right]*\left[\frac{V_A x_1 p_{op}}{p_{op}-x_1}\right]v_3\right] \quad (3\text{-}35)$$

Substituting Equation (3-34) into Equation (3-31) results in a linear differential relation between the output y and the new input v:

$$\begin{bmatrix} \dot{y}_1 \\ \dot{y}_2 \\ \dot{y}_3 \end{bmatrix} = \begin{bmatrix} v_1 \\ v_2 \\ v_3 \end{bmatrix} \quad (3\text{-}36)$$

Since v_2 and v_3 are the same as u_2 and u_3, only v_1 can be used for tracking control, the new control input is obtained by

$$v_1 = \dot{y}_{1ref} - k_{11}e_1 \quad (3\text{-}37)$$

where the tracking error $e_1 = y_1 - y_{1ref}$.

In this form of the nonlinear control, a tracking error may exist due to parameter uncertainty. To obtain more robust control, an integral control term is added to Equation (3-37) as in [69].

$$v_1 = \dot{y}_{1ref} - k_{11}e_1 - k_{12}\int e_1 dt \tag{3-38}$$

Then the output error dynamics from Equation (3-37) are described as follows:

$$\ddot{e}_1 + k_{11}\dot{e}_1 + k_{12}e_1 = 0 \tag{3-39}$$

The asymptotic tracking is achieved by selecting the gains k_{11} and k_{12} appropriately, so as to place the desired closed-loop system poles located in the left-hand plane. These control gains, k_{11} and k_{12}, are calculated by the desired poles, which are located at $-200 \pm j20$. Also, substituting Equation (3-37) into Equation (3-31) yields the control law for u_1, which is given above in Equation (3-26). Nonlinear control law u_1 is fed back for comparison with the inlet flow rate of hydrogen q_{H_2} from the reformer model [20, 58]. The oxygen flow is dependent on hydrogen-oxygen flow ratio r_{H-O} [20, 58]. Since the feedback fuel cell stack current is fed to the reformer and the PEMFCs, respectively, the inlet flow rates of hydrogen and oxygen are appropriately supplied to the PEMFCs based on load changes. Figure 3.21 is a block diagram of a nonlinear PEMFCs model with feedback linearization control.

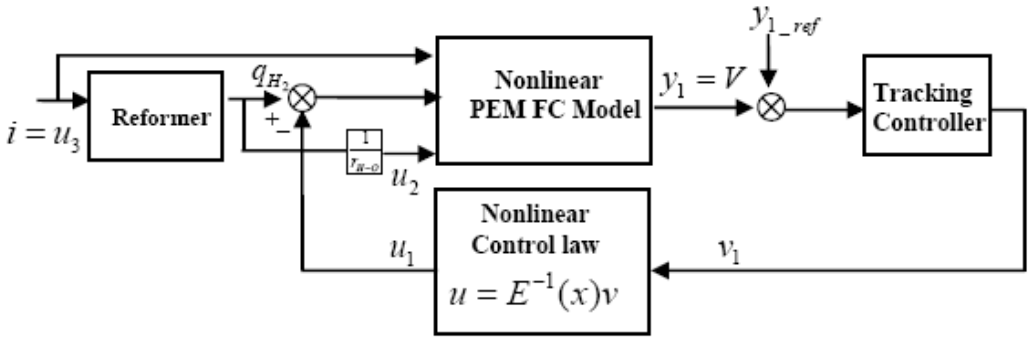

Figure 3.21 Block diagram of nonlinear PEM FC model
with feedback linearization control

3.6.1 Simulation Results

To demonstrate the performance of the proposed nonlinear control law, the system is simulated using the simplified models connected to a load through a DC/DC converter and a three-phase inverter. A conventional PI controller is used for the purpose of comparison. For simplicity, a DC/DC converter is built as a lossless step-up transformer with a ratio 1:10.

Model parameters used in our simulation are given as follows:

- Cell active area: $A_c = 136.7\text{cm}^2$
- Volume of anode: $V_a = 6.495\text{cm}^2$
- Volume of cathode: $V_c = 12.96\,\text{cm}^2$
- Number of cells: $N = 35$
- Operating pressure : 101kPa
- Operating cell temperature: 338.5 K

- No load voltage: $E_0 = 0.6$ V
- Utilization factor: 0.8
- Reformer time constant: 2 sec
- Conversion factor: 2
- Methane reference signal: 0.000015 kmol/s
- Hydrogen-oxygen flow ratio r_{H-O}: 1.1168.

The simulation has been conducted in the SIMULINK environment. Figure 3.22 shows the design of a PEM FC dynamic model with nonlinear control and a DC/AC inverter.

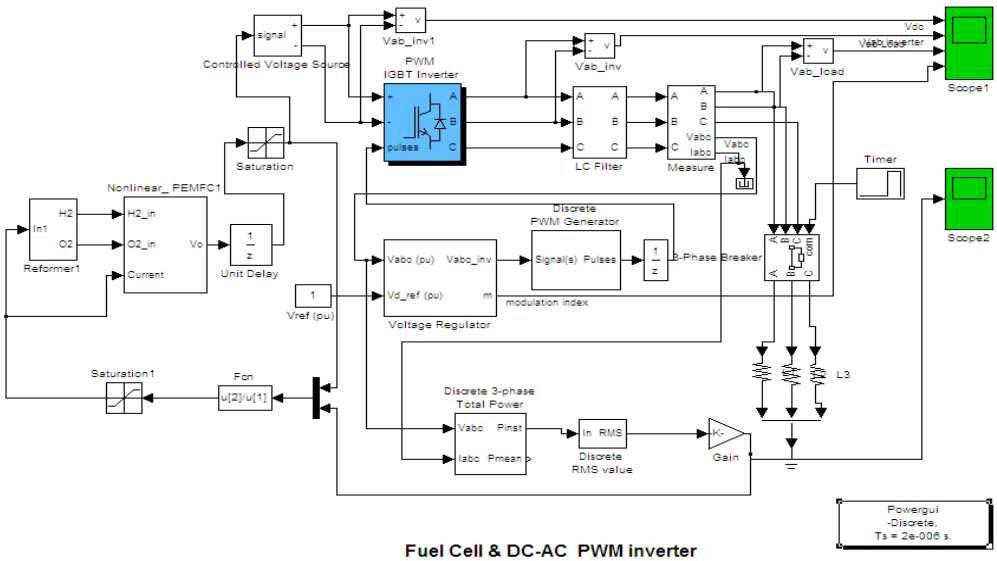

Figure 3.22 PEM FC dynamic model with nonlinear control and DC/AC inverter in SIMULINK

Figure 3.23 displays the design of the reformer, which is the source of the hydrogen and oxygen supplied to the fuel cell.

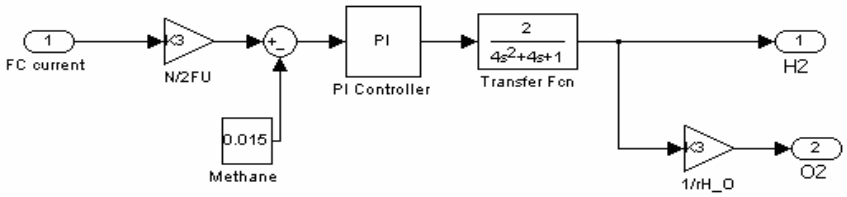

Figure 3.23 Reformer based on SIMULINK

The reformer model and its parameters are selected the same as in [20, 58]. The only difference is that the hydrogen flow rate is compared with the output of nonlinear controller and the difference is defined as the input to the fuel cell. Figure 3.24 shows the dynamic model of a PEM fuel cell with the implementation of nonlinear control. Inputs to the fuel cell are hydrogen, oxygen, and load current, while the output is the voltage. To test the transient behaviors of fuel cells with nonlinear control, we change the pure resistive load from 10 Ω to 5 Ω at time $t = 1.0$ s and from 5 Ω to 10 Ω at time $t = 1.5$ s. Figure 3.25 gives the fuel cell output voltage for the load step change. It is obvious to see that the fuel cell output voltage by nonlinear control remains quite stable under the disturbances caused by load changes. In this case, both linear and nonlinear controller do not consider a secondary energy buffer such as battery and ultracapacitor.

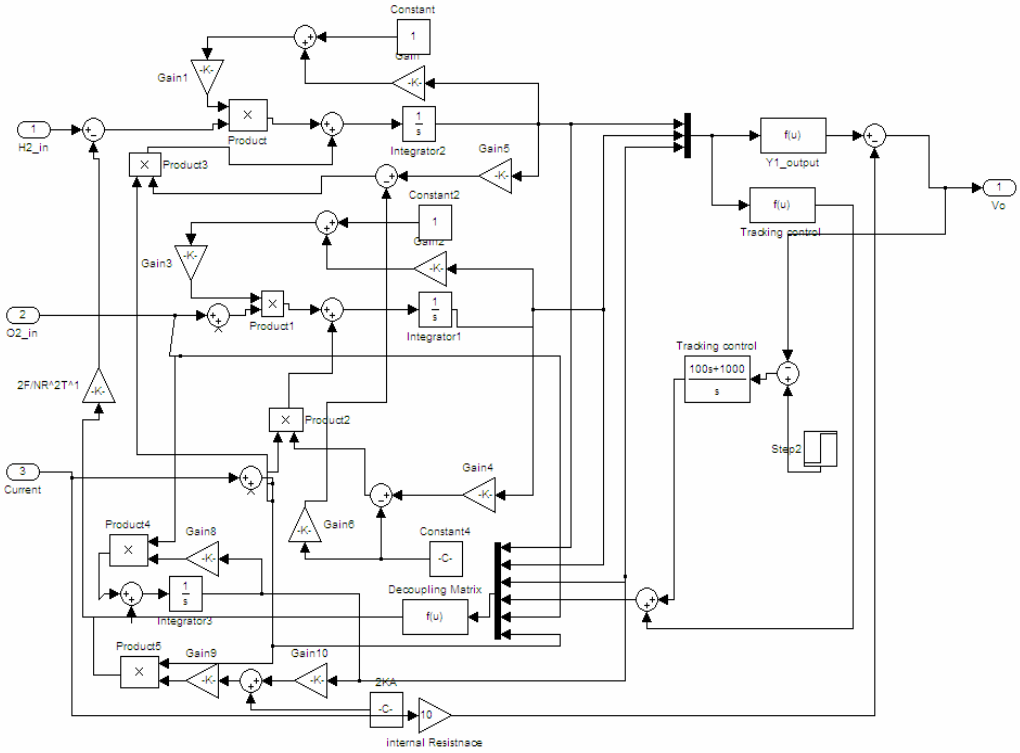

Figure 3.24 PEM FC dynamic model with nonlinear control

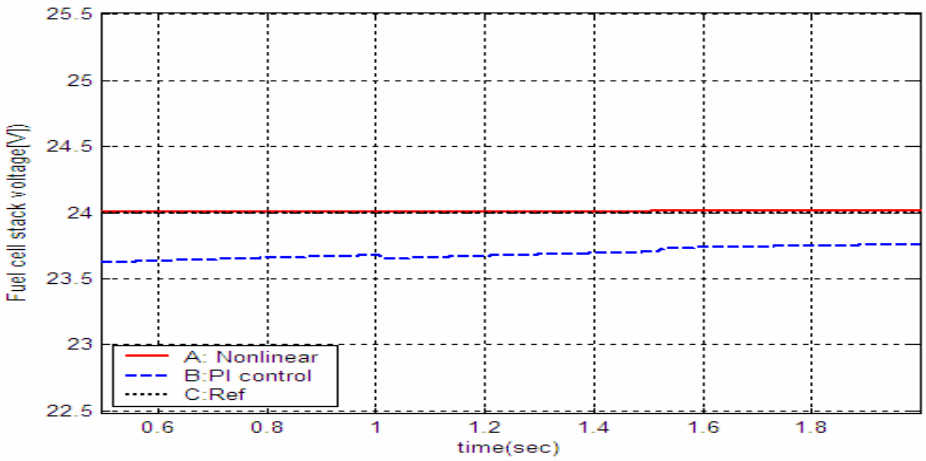

Figure 3.25 Fuel cell output voltage for the load step change

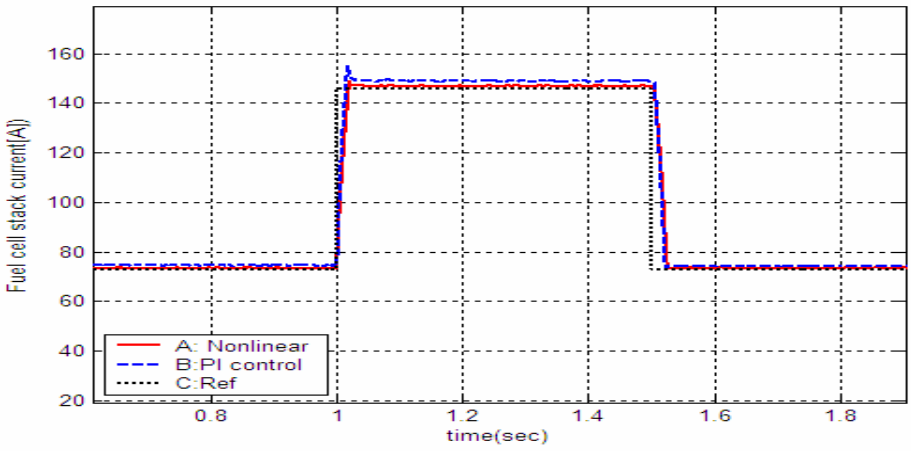

(a)

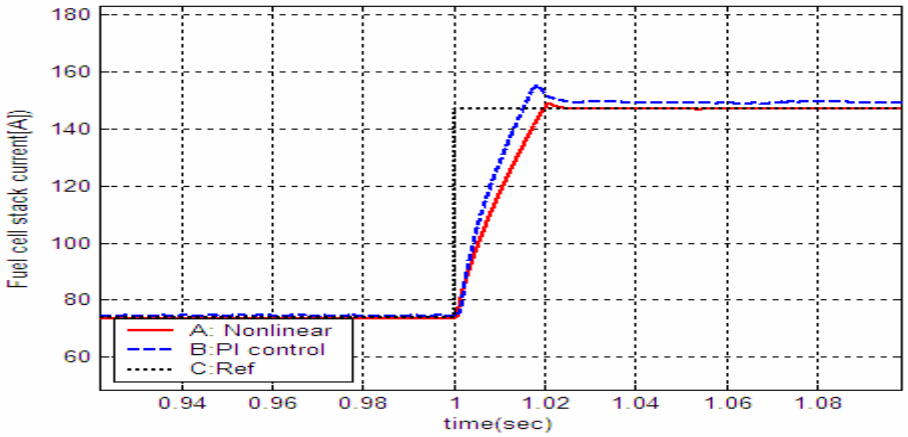

(b)

Figure 3.26 Fuel cell output current for the load step change: (a) Zoom out view, (b) Zoom in of Figure3.26 (a) around t = 1.0 seconds

The fuel cell current under the change of load is shown in Figure 3.26. The transient response of the fuel cell with nonlinear control has less overshoot than with linear control and also reaches the reference faster.

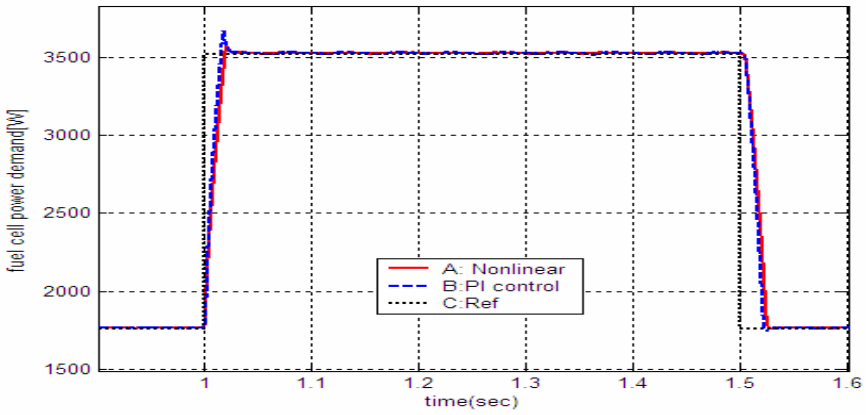

(a)

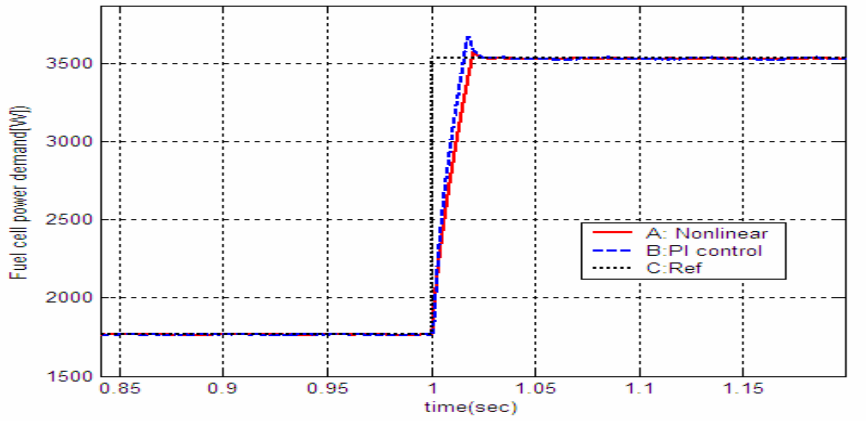

(b)

Figure 3.27 Fuel cell power demand for the load step change: (a) Zoom out view, (b) Zoom in of Figure 3.27(a) around $t = 1.0$ seconds

Fuel cell power demand is provided in Figure 3.27. From this figure, we can see that the fuel cell with nonlinear has very quick responses with less overshoot to the disturbances caused by the load changes.

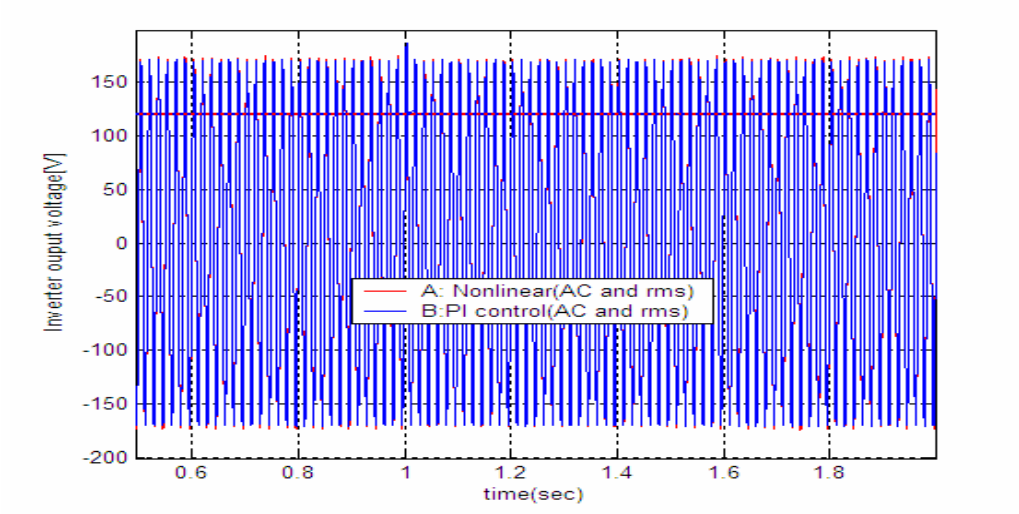

Figure 3.28 Inverter output voltage (line to line) for the load step change: (Solid line indicates RMS value)

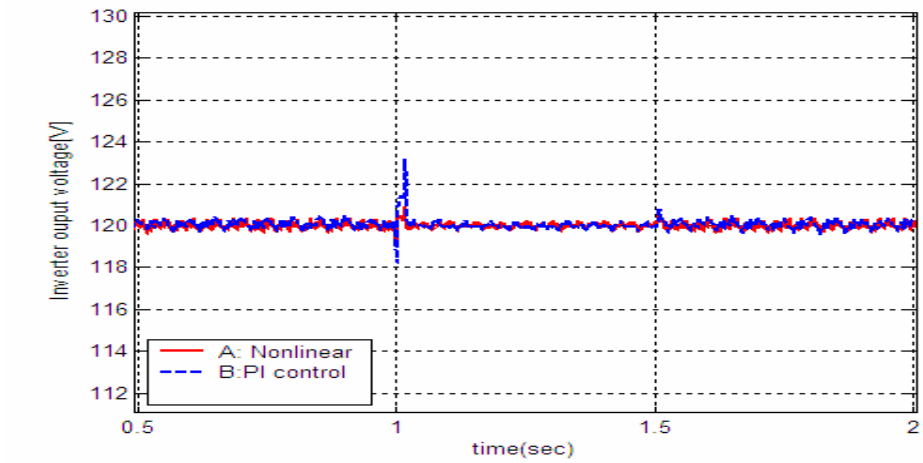

Figure 3.29 Inverter output voltage (RMS value) for load change

Figures 3.28 and 3.29 show the comparison of the inverter line-to-line output voltages and their RMS values between nonlinear and linear controllers. The nonlinear controlled fuel cell has less ripple and fast transient response to the load change. Figure 3.30 gives the inverter output currents and their RMS values.

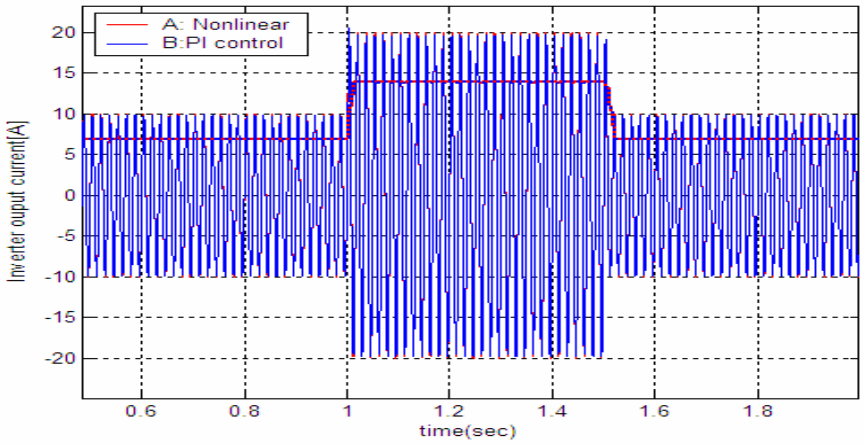

(a)

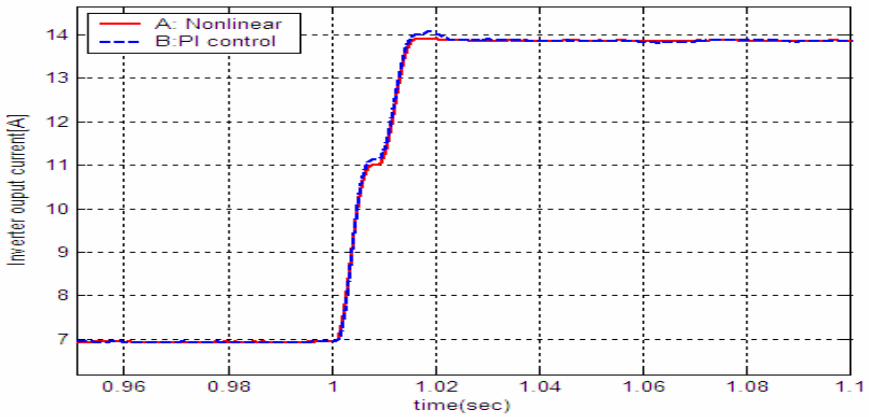

(b)

Figure 3.30 Inverter output current (line to ground) for the load step change (Solid line indicates RMS value): (a) Zoom out view, (b) Zoom in of Figure 3.30 around *t = 1.0* seconds (Inverter output current (RMS) for load change)

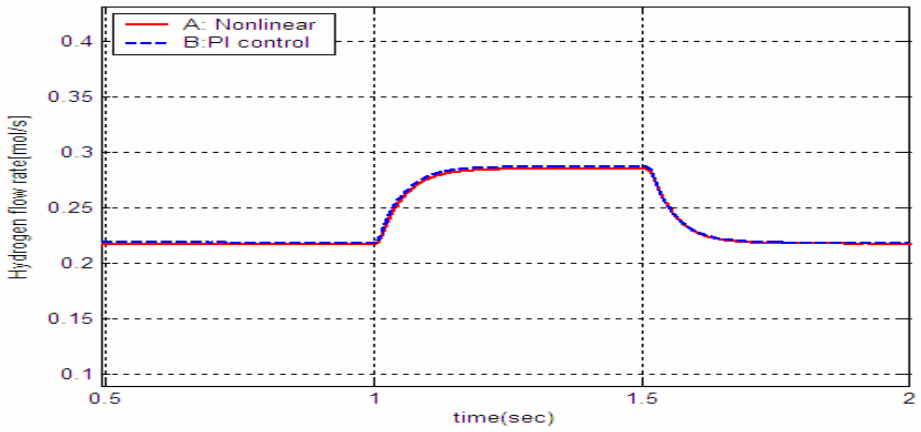

Figure 3.31 Hydrogen flow rate from the reformer

The hydrogen flow rate directly from the reformer caused by load changes is displayed in Figure 3.31. The oxygen flow rate has the same pattern as that in Figure 3.31 but with smaller magnitude because oxygen flow rate is simply determined by the hydrogen-oxygen flow ratio. Since the proportional integral (PI) controller is used to control the flow of methane in the reformer, and hydrogen and oxygen flow rates mainly depend upon reformer parameters such as the fuel utilization factor, PI gains, and the reformer time constant, these flow rates under the nonlinear and linear controls are not significantly different. Figure 3.32 shows fuel cell boost DC/DC converter output voltage. For simplicity, a boost DC/DC converter is built as a lossless step-up transformer. Thus, the fuel stack voltage is boosted according to the ratio 1:10.

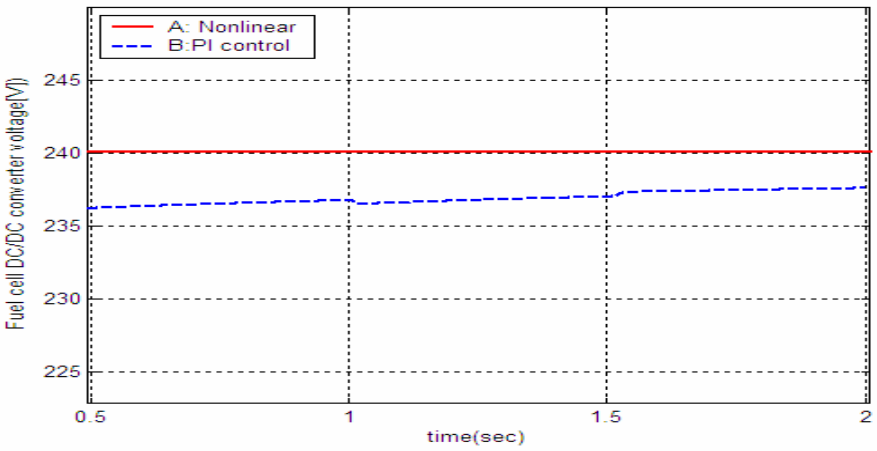

Figure 3.32 Fuel cell boost DC/DC converter voltage output

CHAPTER 4

OPTIMIZATION OF PEMFCs SYSTEMS

4.1 Introduction

Due to these multiple advantages of PEMFCs mentioned in Chapter 1, the PEMFCs become popular for an alternative power source in transportations and stationary power systems. First of all, to commercialize the PEMFC, the cost and the efficiency need to be taken into account simultaneously. So, an optimal PEMFCs system design considering cost and efficiency of PEMFCs together has become a hot topic in recent years. For stationary and transportation applications, the efficiency of fuel cells is required to achieve higher or equal to 40% comparing the internal combustion engine [3].

However, since the efficiency decreases as the power output increases [3], more cells requesting causes more expenses need to be integrated to achieve a high efficiency for the maximum power output. In this chapter, using a multi-objective optimization technique, the SQP (sequential quadratic programming) method, the efficiency and the cost of fuel cell system have been optimized under various operating conditions. The system pressure, hydrogen and air stoichiometric ratios, the fuel cell current density and the fuel cell temperature are defined as design variables.

Section 4.2 gives a concept of PEMFCs' efficiency. Section 4.3 addresses the design of PEMFCs cost model for the optimization. In Section 4.4, the multi-objective

optimization for the PEMFC is presented. Section 4.5 provides the results and discussion in regard to the optimization.

4.2 PEMFCs Efficiency Model

In the practice, specially, the Ballard mark V[1], its fuel cell voltage per cell is described in the Equation1, which has specific coefficients given by the table 4.1 .

$$V_c = E_{oc} - r \cdot i - C\ln(i) - m\exp(ni) \tag{4-1}$$

Table 4.1 Ballard Mark V PEMFC Coefficient [39]

Coefficients	**Values (T in ^{o}C)**
$E_{oc}[V]$	1.05
$C[V]$	$4.01\times10^{-2} - 1.4\times10^{-4}T$
$r\ [k\Omega / cm^2]$	$4.77\times10^{-4} - 3.32\times10^{-6}T$
$m[V]\mathrm{T} \geq 39^{o}\mathrm{C}$	$1.1\times10^{-4} - 1.2\times10^{-6}T$
$m[V]\mathrm{T} \leq 39^{o}\mathrm{C}$	$3.3\times10^{-3} - 8.2\times10^{-5}T$
n [cm^2/mA]	8.0×10^{-3}

The detailed explanation of each voltage loss can be found in [1]. In the Nernst equation, the ideal standard potential E_o for a PEMFC is 1.229 volts with liquid water product, or 1.18 volts with gaseous water product [41]. Under the assumption that pressure on both the cathode and the anode is approximately the same, the Nernst equation is transferred into a function of the system pressure P_{sys} [1, 42] given as follows.

$$E = N\left[E_o + \frac{RT}{2F}\ln\left(\frac{\alpha\cdot\beta^{\frac{1}{2}}}{\delta}\right) + \frac{RT}{4F}\ln(P_{sys})\right] \tag{4-2}$$

where α, β and δ are constants depending on the molar masses and concentrations of H_2, O_2 and H_2O. Each partial pressure can be expressed by these constants and the system pressures.

$$\begin{aligned} P_{H_2} &= \alpha P_{sys} \\ P_{O_2} &= \beta P_{sys} \\ P_{H_2O} &= \delta P_{sys} \end{aligned} \tag{4-3}$$

With assuming that α, β and δ are constants, Equation (4-3) shows that the EMF of a fuel cell is increased by the system pressure P_{sys}. Although P_{sys} is able to use as one of optimization design variables, the predefined α, β and δ are required for the optimization, so the system pressure can be considered in the compressor model Equation (4-7). For the multi-objective optimization, the specification of the fuel cell stacks has to be identified in advance and then each optimization model will be delivered.

Table 4.2 Specification of the Fuel Cell System based on the [1]

Items	**Specification**
Nominal power output	50 kW
Stack temperature	353 K (80^oC)
Inlet H_2/air humidity	100 %
Cell open voltage, E_o	1.05 V
Entry air temperature , T_e	288K (15^oC)
Specific heat constant, c_p	1,004 $JK^{-1}kg^{-1}$
Compressor efficiency, η_c	0.75
Compressor connecting efficiency, η_m	0.85
Inlet pressure , P_{in}	10^5 Pa

First, the fuel cell efficiency optimization model is derived based on [43], the output power of the fuel cell system is described by the following equations.

$$P_{fcs} = P_{stack} - P_{prs} \tag{4-4}$$

$$P_{stack} = N \cdot i \cdot V_c \cdot A = 50kW \tag{4-5}$$

$$P_{prs} = P_{comp} + P_{oth} \tag{4-6}$$

$$P_{comp} = c_p \frac{T_e}{\eta_m \cdot \eta_{mt}} \left(\left(\frac{P_{sys}}{P_{in}} \right)^{0.286} - 1 \right) \cdot \dot{m} \tag{4-7}$$

$$\dot{m} = 3.57 \times 10^{-7} \times \lambda_{air} \times i \times A \times N \ \text{kgs}^{-1} \tag{4-8}$$

Where P_{fcs} is net power of the fuel cell system and P_{stack} is the stack output power. The parasitic power consumed by the compressor is P_{comp} and the others, P_{oth}. Even though P_{oth} was assumed to be a constant of 2 kW in [43] based on 62.5kW rated stack power, in here, it is a 5 percent of the nominal power out, 50kW due to including unexpected power consumption, so to speak, P_{oth} is assumed to be 2.5 kW. The flow rate of air $\dot{m}$ is related to the air stoichimetry, the cell current density, and active cell area. Before proceeding to build the efficiency optimization model, let us consider how to decide the optimal cell number and cell area. Once an optimal current density and a cell voltage have been achieved, the total active cell area($N \times A$) is able to be calculated by using optimal power density, the product of V_c and i, namely, we can decide a number of cell as long as a single active cell area is given. The system pressure of the fuel cell is

always higher than the atmospheric pressure in a certain range because the compressor can not provide a pressure under the atmospheric pressure.

According to [44], P_{sys} must be 0.02 MPa higher than the inlet air pressure P_{in} and therefore this requirement is included as one of constraints in the optimization study. Thus, if using the lower heating value (LHV), the fuel cell efficiency optimization model is obtained to achieve a maximum efficiency of the fuel cell as Equation (4-9).

$$\max \quad \eta_{fc}\left(P_{sys},\lambda_{H_2},\lambda_{air},V_c,i\right)=\frac{V_c\cdot u_f\cdot(P_{stack}-P_{prs})}{1.25\cdot P_{stack}}$$

s.t.

$$\begin{aligned} &P_{sys}\geq 0.12MPa \\ &\lambda_{H_2}\geq 1 \\ &\lambda_{air}\geq 1 \\ &V_c\geq 0\ \mathrm{V} \\ &i\geq 0\ mA/cm^2 \end{aligned} \tag{4-9}$$

Where u_f is the fuel utilization rate, which is the reverse of hydrogen stoichiometric ratio [45]. The air stoichiometric ratio must be over the minimum limit in order to prevent the depletion of oxygen at this minimum limit. The hydrogen stoichiometric ratio is also greater than 1 unless it runs in the hydrogen dead-ended mode [45]. Normally higher air and hydrogen stoichiometric ratio are preferred in low power ranges. The ranges of cell voltage and current density will be based on the V-I polization curve. Since the cell voltage is a function of the cell current density as seen in Equation (4-1), we can reduce to four optimization parameters such as system pressure,

air and hydrogen stoichiometric ratios and cell current density. By using four optimization parameters, the fuel cell efficiency optimization model has been built. In the following section, the fuel cell cost optimization model will be described.

4.3 PEMFCs Cost Model

For this analysis, we are particularly interested in the small and middle size fuel cell systems. We use a 50 kW PEM fuel cell system for transportation applications as the example of our study. For the fuel cell cost model for optimization, the cost of fuel cell stack and balance of plant (BOP) components for water, thermal and fuel management have been assessed. Due to lack of latest data about hydrogen storage, power electronics, electric drive motor, and hybrid batteries for PEM fuel cell system, the fuel storage and fuel generation components were excluded from the scope of this study. The target cost is the cost of the fuel cell stack and BOP system given as follows.

$$C = C_{st} + C_{BOP} \tag{4-10}$$

where C_{st} is the cost of the fuel cell stack and C_{BOP} is the cost of balance of plants. For assessing of fuel cell stack cost C_{st}, currently two types of fuel cell stack cost models are available in [46, 47]. One is represented by the following equation [47].

$$C_{st1} = M \cdot \left[\left(\frac{A - 105.4}{10} + \frac{17.56 \cdot L_p \cdot C_p}{380} \right) \cdot \frac{P_G \cdot (1+d)^N}{P_d} + B \right] \tag{4-11}$$

where,

M = Fixed cost markup (1.1 default),

A, B = Cost parameter that depends on production volume (See table 4.3),

L_p = Fuel cell platinum loading for both electrodes (mg/cm^2),

C_p = Cost of platinum ($/troy ounce),

P_G = Fuel cell gross DC peak power (kW),

P_d = Fuel cell power density (W/cm^2),

d = Annual fuel cell degradation (%/year), and

N = Planned fuel cell lifetime (years)

The parameter A is the power dependent term in terms of dollar per square meter of membrane area, and the parameter B is the fixed cost for the fuel cell stack.

Table 4.3 Fuel Cell Stack Cost Parameters [13]

Production Volume	**Cost parameter, A ($/m$^{2)}$)**	**Cost parameter, B ($)**
100	811.77	1311.3
1,000	722.54	363.33
10,000	454.45	428.51
30,000	329.24	405.79
60,000	312.26	160.98

In [46], the annual fuel cell degradation is assumed to be a 6% drop per year and the planned fuel cell lifetime is assumed to be 87,600 hours, 10 years. The platinum loading, L_p is defined as 0.4 mg/cm^2 and the cost of platinum, C_p is 1160 $/troy ounce. Although this C_{st1} ($) model is used in the paper [48], it is not logically understandable because suddenly many constants and parameters M, A, and B are involved in Equation

(4-11) without justification. Thus, more reasonable stack cost model C_{st2} [49, 50] is chosen for our study. The C_{st2} ($/kW) is described as follows:

$$C_{st2} = \frac{(C_m + C_e + C_b + C_{pt} + C_o)}{P} + C_a \qquad (4\text{-}12a)$$

$$C_{pt} = C_{wpt} \times Y_{pt} \qquad (4\text{-}12b)$$

$$P = 10 \times V_c \times i \qquad (4\text{-}12c)$$

where, C_{st2} is the fuel cell stack cost per kW($/kW), C_m the membrane cost ($/m^2), C_e the electrode cost ($/m^2), C_b the bipolar plates cost ($/m^2), C_{pt} the cost of platinum catalyst loading ($/m^2), C_{wpt} the weight of platinum catalyst loading (g/m^2), Y_{pt} the unit cost of platinum($/g), C_o the cost of peripheral materials ($/m^2) which include end plates, plastic frame and thrust volts, C_a the assembly cost ($/kW), V_c the cell voltage, and i the cell current density(A/cm^2). In [49, 50], the cost of each component of 50 kW PEM fuel cell stack was estimated based on an automatic production line with an annual production capacity of 18,000 vehicles. Table 4.4 shows specific cost for components in PEM fuel cell stack.

Table 4.4 Specific Cost for Components in PEM Fuel Cell Stack [49, 50]

Components	**Cost**
Nafion membrane	500 ($/m^2)
Platinum(2-4g/m^2)	32-64($/m^2)
Electrode (max. 0.8 mm for single cell)	177($/m^2)
Bipolar plate (max. 4 mm)	1650($/m^2)
Peripheral parts	15.6($/m^2)
Assembly	7.7($/kW)

With respect to the cost of balance of plants C_{BOP}, the cost model can be found in [46]. C_{BOP}, including the air blower, humidification, radiator, stainless pump, iron pump, control electronics, actuation, piping and valves, which is approximately by a quadratic equation in the fuel cell output power and varies with the production volume as the following Equations [46].

For 100 Production Units:

$$C_a = 3343.5 + 39.942 \cdot P_G - 0.0454 \cdot P_G^2 \quad \text{(4-13a)}$$

For 10,000 Production Units:

$$C_a = 2980.2 + 35.654 \cdot P_G - 0.0422 \cdot P_G^2 \quad \text{(4-13b)}$$

Unfortunately, since Equations (4-13a) and (4-13b) are not only with respect to stationary PEM fuel cell, but also out of date, which was published in 1999, they cannot be applied to this analysis. Therefore, using most updated data [49], C_{BOP} is estimated to 34 percent of fuel cell system cost as C_{st} including assembly, that is assumed to be contributing approximately 66 percent of fuel cell system cost. Even though the breakdown of the fuel cell system is for 80 kW direct hydrogen system, the same breakdown is applied to use for 50 kW fuel cell system because the cost analysis is only integrated in the stack and BOP costs.

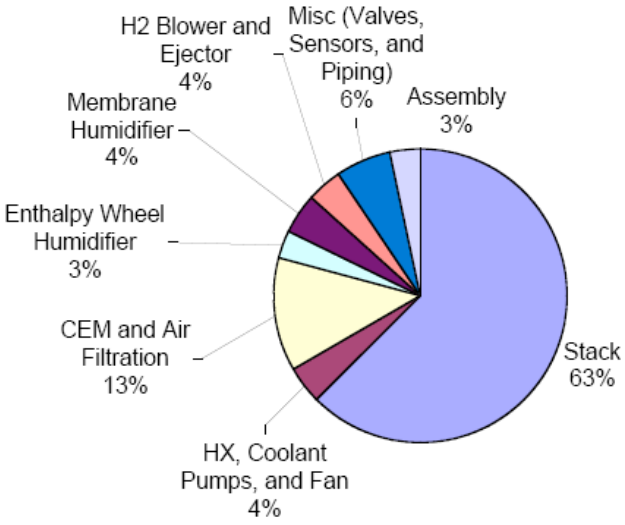

Figure 4.1 Breakdown in Stack and BOP component Cost contribution for an 80 kW direct hydrogen fuel cell system [51]

In order to build the cost model sharing same optimization parameters, the cost model is likely to be a function of the efficiency as Equation 4-14, which is able to investigate the impact of the cell voltage, V_c and current density, i as well as other optimization parameters on the fuel cell cost. In our study, the costs of the fuel cell stack and balance of plant (BOP) are considered. And the maximum fuel cells system cost is obtained as the maximum efficiency is achieved. Thus, this cost optimization model can share same optimization parameters with the system efficiency optimization model and each feasible range of the parameters will be used as a constraint of this optimization problem. The base production volume is chosen as 18,000 units, which can be a mass production for the mobile 50 kW PEM fuel cell system.

$$\min \quad C_{FC}\left(P_{sys}, \lambda_{H_2}, \lambda_{air}, V_c, i\right) = \left(C_{st} + C_{BOP}\right) \times \eta_{fc}$$

s.t.

$$
\begin{aligned}
&P_{sys} \geq 0.12MPa \\
&\lambda_{H_2} \geq 1 \\
&\lambda_{air} \geq 1 \\
&V_c \geq 0\ \mathrm{V} \\
&i \geq 0\ mA/cm^2
\end{aligned}
\tag{4-14}
$$

As explained in the section the cell voltage and current density, two of the optimization parameters of the cost model could be reduced to just the cell current density.

In the following section, the multi-objective optimization will be presented with the consideration of both the efficiency and the cost optimization.

4.4. Multiobjective Optimization of PEMFCs

According to the above considerations, the multi-objective optimization problem is formulated as follows:

$$
\min \quad \eta_{fc}\left(P_{sys}, \lambda_{H_2}, \lambda_{air}, i\right) = (-1) \cdot \frac{V_c \cdot u_f \cdot (P_{stack} - P_{prs})}{1.25 \cdot P_{stack}}
$$

$$
\min \quad C_{FC}\left(P_{sys}, \lambda_{H_2}, \lambda_{air}, i\right) = (C_{st} + C_{BOP}) \times \eta_{fc}
$$

s.t.

$$
\begin{aligned}
&P_{sys} \geq 0.12MPa \\
&\lambda_{H_2} \geq 1 \\
&\lambda_{air} \geq 1 \\
&i \geq 0 mA/cm^2
\end{aligned}
\tag{4-15}
$$

In the multi-objective optimization problem, both objective functions have to be minimized simultaneously. Normally, the objectives in such a problem have often the issue of the conflict between the objectives. From Equation 4-15, when the efficiency is

increased, the cost is increased as well. Thus, during the optimization process for such a problem, there is no single optimum solution to improve the both objectives, which means a number of optimal solutions exit. As the solution to the multi-objective problem is a set of points that represent the best trade-offs between the objective functions, for each solution, there is no way to further improve an objective function without worsening at least another one. Such points are called Pareto Optimal points or noninferior points. The set of all the Pareto Optimal points is called the Pareto Optimal Set or the Pareto frontier.

In this study, the MATLAB Optimization toolbox [52] for multi-objective optimization problem is used to find the Pareto frontier solution set. MATLAB has two functions to solve a multi-objective problem: fminimax and fgoalattain. Even though both the methods use the popular nonlinear programming algorithm, a Sequential Quadratic Programming (SQP), the fminimax method is more appropriate to be applied to our optimization study than the fgoalattain method because the fgoalattain method is more complicated than the fminimax due to the defining weighting coefficients. The general form of fminimax method is:

$$\min_{x} \quad \max_{f} \quad \{f_1, f_2, \ldots, f_m\}$$

such that

$$\begin{aligned} &Ax \le b \\ &A_{eq}x = b_{eq} \\ &C(x) \le 0 \\ &C_{eq}(x) = 0 \\ &L_b \le x \le U_b \end{aligned} \tag{4-16}$$

where x is the design variable vector; $f_1, f_2, \ldots, f_m$ are the objective functions; matrix A and vector b are the coefficients of the linear inequality constraints; matrix A_{eq} and vector b_{eq} are the coefficients of the linear equality constraints; C contains the nonlinear inequality constraints; C_{eq} contains the nonlinear equality constraints; and L_b and U_b are the lower and upper bounds, respectively.

In order to search for an optimal design value x, the fminimax method iteratively minimizes the worst case value (or maximum) of the objective functions subject to the constraints. The advantage of this method is to easily find the optimum design point from an arbitrary initial design point. Furthermore, less function and gradient evaluation are required compared to other constrained nonlinear optimization. However, the main disadvantage of both methods, fminimax and fgoalattain, is that the objective functions must be continuous and each method has a limitation to search for global solutions.

4.5 Results and Discussion

In this section, the fminimax method is executed to solve the multi-objective optimization. To avoid the unrealistic design criterion, the upper bounds of the system pressure, air and hydrogen stoichiometric ratios are specified at 10 Mpa, 10 and 10, respectively. According to the polarization V-I curve in Figure 2.2, the cell current density will lie within the range of 0 to 1A/cm^2, which is used as one of bound limits for the optimization. The bound limits of the design variables are given as follows:

$$
\begin{aligned}
&0.12MPa \le P_{sys} \le 10MPa \\
&1 \le \lambda_{H_2} \le 10 \\
&1 \le \lambda_{air} \le 10 \\
&0 \le i \le 1A/cm^2
\end{aligned}
\tag{4-17}
$$

With various initial conditions of the design parameters, P_{sys}, λ_{H_2}, λ_{air}, and i, corresponding tradeoffs (Pareto) solutions are obtained. So to speak, these solutions are in the Pareto set, that is, as one objective is improved in the set the other is worsened.

For simplicity, the initial conditions is able to be described in the column vector, like [P_{sys}, λ_{H_2}, λ_{air}, i]. If an arbitrary initial condition is defined as the vector, In1= [0.12MPa, 2, 2, 800mA/cm^2], Figure 4.2 shows the trade-off solution based on the vector In1. In Figure 4.2, as the efficiency is improved in the set, the cost is increased as well. In changing the initial condition, this Pareto frontier will be changed because the fminimax method will find local solution in the changed initial condition.

Firstly, when In1 is changed to ln2= [0.24MPa, 2, 2, 800mA/cm^2], that is, the system pressure becomes two times bigger than the one of the In1, Figure 4.2 shows how this change affects the optimization of the fuel cell system. As seen in Figure 4.2, the higher system pressure is able to achieve the cost effective and high performance model comparing with the model given by the ln1. For instance, in Figure 4.2, at the efficiency 0.45, the ln2 Pareto frontier is corresponding to to about 420 $/kW, whereas, ln1 Pareto frontier is almost over 700 $/kW, that mean In1 is less economic condition than the ln2.

However, in the case of much higher pressure, the change from the ln1 to ln3= [0.36MPa, 2, 2, 800mA/cm^2] as shown in the Figure 4.3, although the better optimum model than In2 is obtained, the efficiency range of the ln3 becomes unrealistic because the fuel cell system efficiency is not normally greater than 0.6 [1]. Hence, the initial condition ln2 is more recommendable than the ln3. Secondly, if the initial hydrogen stoichiomertic ratio is changed from 2 to 1.5 such as ln4 = [0.12MPa, 1.5, 1, 800mA/cm^2], the less cost effective and bad performance model is found in Figure 4.5. Hence, around the hydrogen stoichiomertic ratio 2 is more preferable than 1.5.

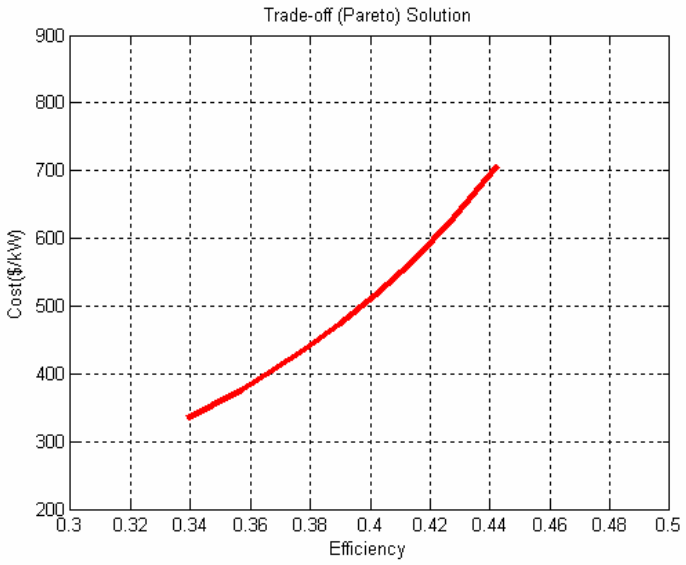

Figure 4.2 Pareto frontier based on the In1
(In1= [0.12MPa, 2, 2, 800mA/cm^2])

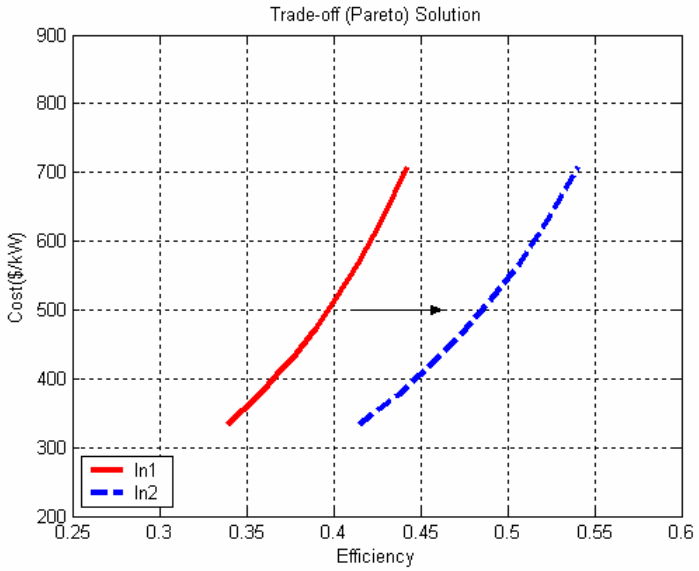

Figure 4.3 Pareto frontier change from In1 to In2
(In2= [0.24MPa, 2, 2, 800mA/cm^2])

In the case that the air stoichiometric ratio is changed from 2 to 1.5 as the In5=[0.12MPa, 1.5, 1, 800mA/cm^2], more cost and efficiency effective model is achieved in Figure 4.6. However if the air stoichiometric ratio keeps decreasing to 1, the efficiency is not applicable to the real system as seen in the Figure 4.6. Hence, the ratio around 1.5 is more preferable than 2 and 1. For the current density, as it decreases, the cost and efficiency effective model is achieved. Through the trial and error, the optimal current density is approximately estimated to 450 mA/cm^2. With comparing with In1, the In7 has a better efficiency and cost effective model as shown in Figure 4.8. With the recommend current density 450 mA/cm^2 and V-I polarization curve Figure 2.2, the optimal cell voltage can be calculated to 0.72 V and the power density will be 3.2 kW/m^2. If 50kW rate power output is selected, then the total active cell area is 15.625 m^2, which means the stack will need to contain 174 layers of a single cell with 30 cm

×30cm active cell area. Thus, the optimal current density allows us to determine the total active cell area and even provide the information about the cell number to be required for the target stack if the a single cell area is given.

Figures 4.3 - 4.10 indicate that the change of each design variable gives a severe impact on the cost and efficiency of the fuel cell. Specially, since the current density is closely associated with the fuel cell area, it affects more directly on the fuel cell cost and efficiency rather than any other variables.

When selecting the preferable initial condition, In8= [0.24MPa, 2, 1.5, 450mA/cm^2] based on the above discussion, the Pareto solution is achieved in Figure 4.9, but it is definitely not applicable to the real system due to an impractical high efficiency. Therefore, In8 must be adjusted such that the Parteto solution lies in the realistic ranges. As In8=[0.24MPa, 2, 1.5, 450mA/cm^2] is adjusted to In9=[0.24MPa, 1.75, 1.5, 450mA/cm^2], this condition can be used for the design of economic and high performance fuel cell. Any initial condition can be chosen as long as it is within the bound limits and the corresponding Pareto solutions are applicable in practice.

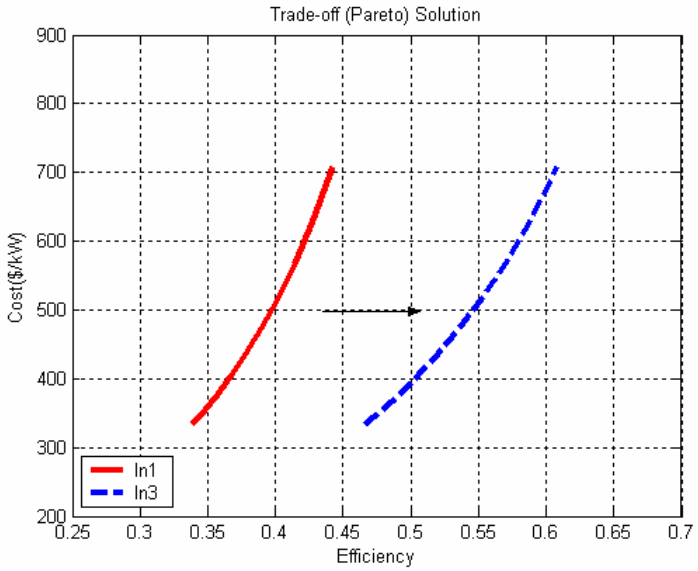

Figure 4.4 Pareto frontier change from In1 to In3
(In3 =[0.36MPa, 2, 2, 800mA/cm^2])

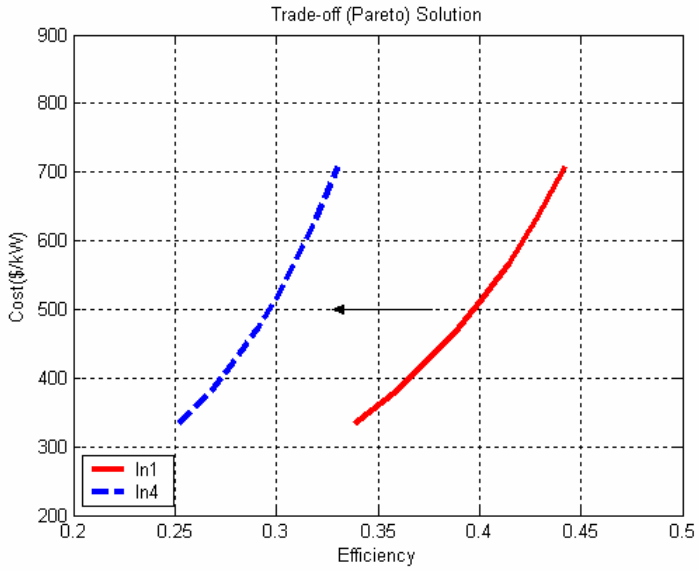

Figure 4.5 Pareto frontier change from In1 to In4
(In4=[0.12MPa, 1.5, 2, 800mA/cm^2])

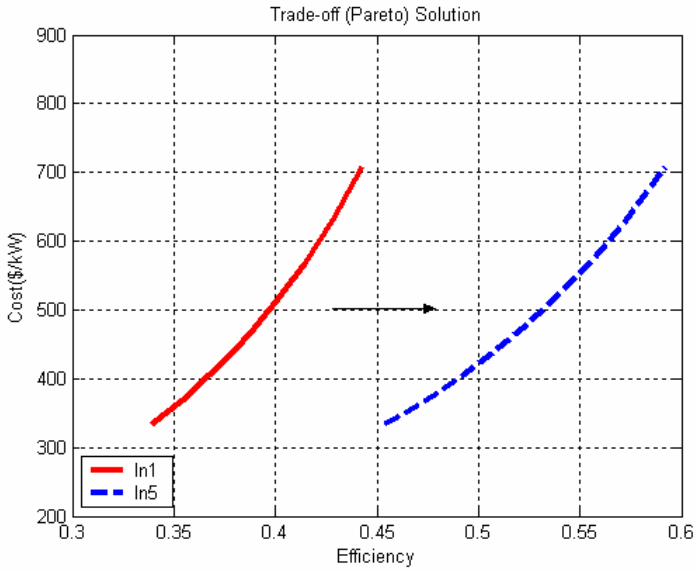

Figure 4.6 Pareto frontier change from In1 to In5 (In5=[0.12MPa, 2,1.5, 800mA/cm^2])

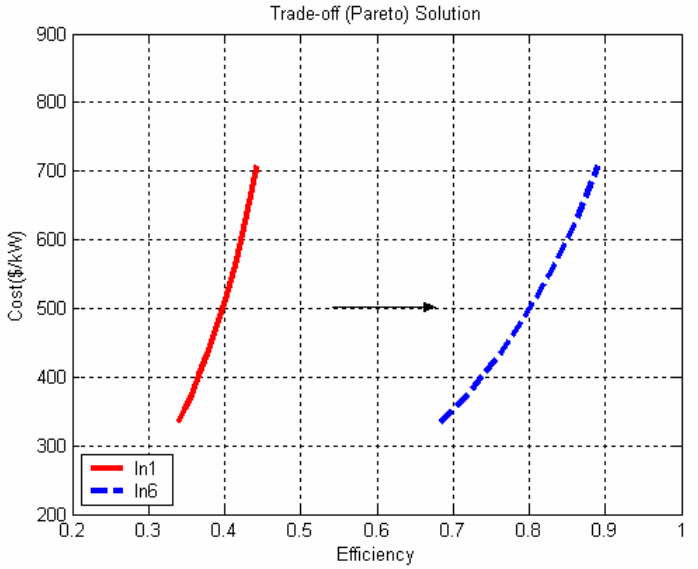

Figure 4.7 Pareto frontier change from In1 to In6 (In6=[0.12MPa, 2,1, 800mA/cm^2])

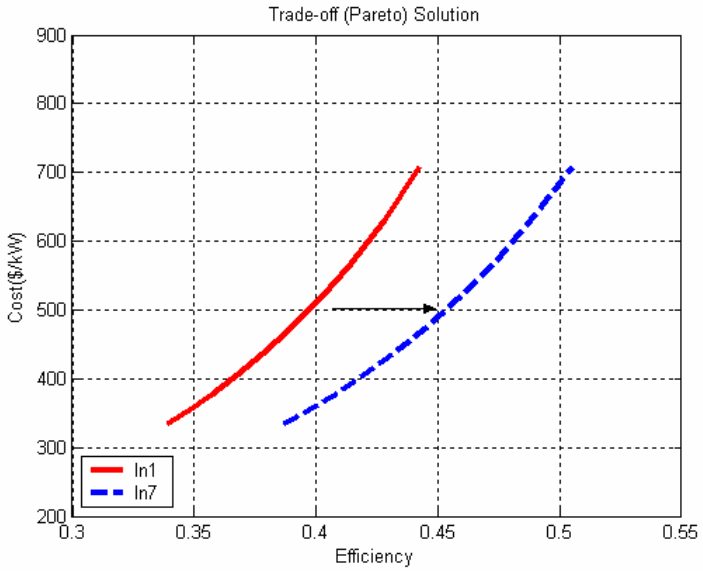

Figure 4.8 Pareto frontier change from In1 to In7
(In7=[0.12MPa, 2,2, 450mA/cm2])

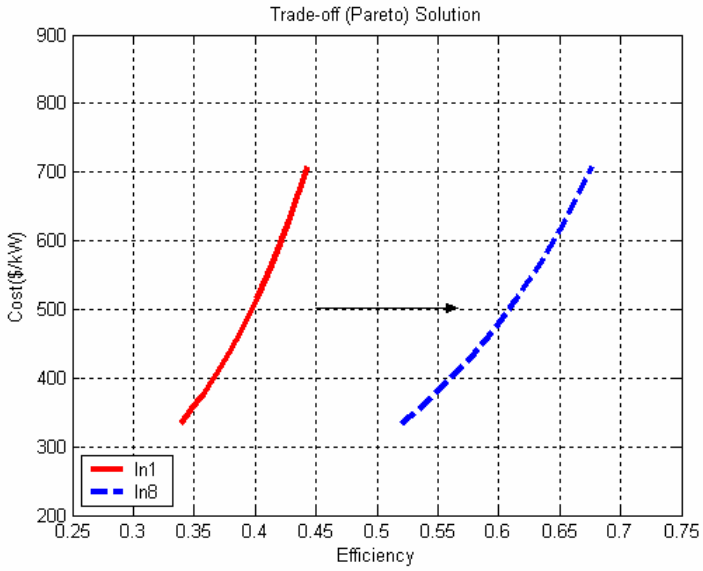

Figure 4.9 Pareto frontier change from In1 to In8
(In8=[0.24MPa, 2,1.5, 450mA/cm^2])

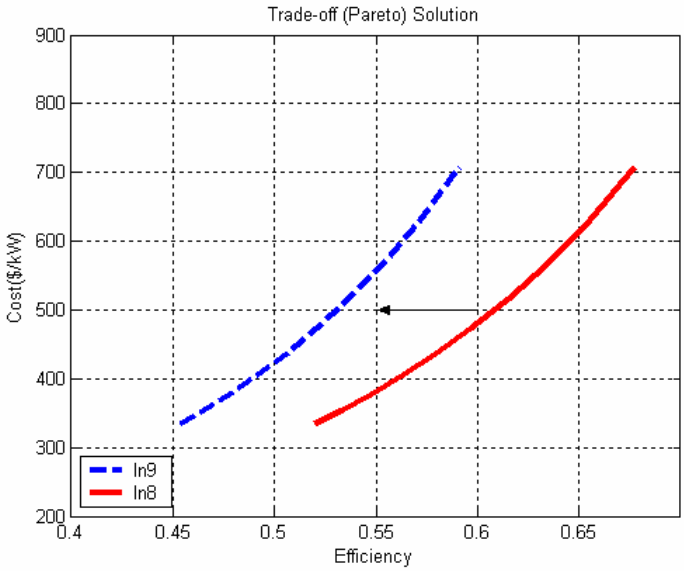

Figure 4.10 Pareto frontier change from In8 to In9 (In9=[0.24MPa, 1.75,1.5, 450mA/cm^2])

CHAPTER 5

POWER INTERFACE DESIGN AND SUPERVISORY CONTROL OF FUEL CELL BASED HYBRID POWER SYSTEM

5.1 Power Interface Design of PEM Fuel Cell Systems

5.1.1 Introduction

A fuel cell voltage varies under the load changes. For instance, the fuel cell voltage reaches to the maximum when no load is applied while it drops as load currents increases. Particularly for high currents, significant voltage drop can be seen due to the activation overvoltage and ohmic resistance losses in the membrane [1]. Thus, a secondary energy source is needed to satisfy the load demands. Presently, many studies regarding using the secondary power sources for the fuel cell system have been performed [53-57]. Most studies have been conducted for transportation applications [53-57].

Lately, U. Unzunoglu and Alam [57] used an ultracapacitor in parallel to fuel cell systems without using a bidirectional converter for residential applications. This will create a problem when optimally charging and discharing the ultracapacitor during transient processes especially for transportation applications. In this study, I proposed the fuel cell based hybrid power system in which the ultracapacitor is connected to the fuel cell terminal voltage through the bidirectional converter for stationary power applications.

The controller for the bidirectional converter is designed so that any substantial voltage drop of the fuel cell can be prevented during transient energy deliveries and peak power demand periods. The control analysis is performed in boost (charging) and buck (discharging) mode separately. A 5kW PEM fuel cell system is considered for the residential system and the nominal voltage of ultracapacitor is set to 74V [54]. For the fast load changing, the fuel cell current slope is limited to $4As^{-1}$[55] in order to prevent the fuel cell damage because a frequent fast step up and down load may apply an unnecessary stress to the fuel cell control systems such as pumps, valves, compressors and etc.

Although, during the peak power period, the total maximum power was assumed to be 7.4 kW in [57], in the simulation, the total power demand can be up to 10 kW. So, the additional power exceeding the fuel cell power can be compensated by the ultracapacitor through the bidirectional converter during that period. In the normal load (less 5kW) and steady state conditions, the ultracapacitor also can be charged by controlling the converter. This fuel cell based hybrid system was tested using Matlab Simulink.

5.1.2 Small Signal Transfer Function of Bidirectional Converter

The configuration of bidirectional converter is shown in Figure 5.1. The ultracapacitor bank C_u is considered as energy storage because it offers not only a higher energy density than conventional capacitors and batteries, but also minimal maintenances [8]. It is actually a buck-boost structure. It can be analyzed in two

different modes separately. In the boost mode, if the switch S_2 and the diode D_1 are in active, then the ultracapacitor can absorb the energy from the fuel cell system. In the buck mode, if the switch S_1 and the diode D_2 are in active, then the energy from the capacitor can be released to the fuel cell terminal. The main objective of this system is to quickly provide the transient energy to the load from the ultracapacitor and to transfer the steady states energy to ultracapacitor. Let us consider the boost mode first.

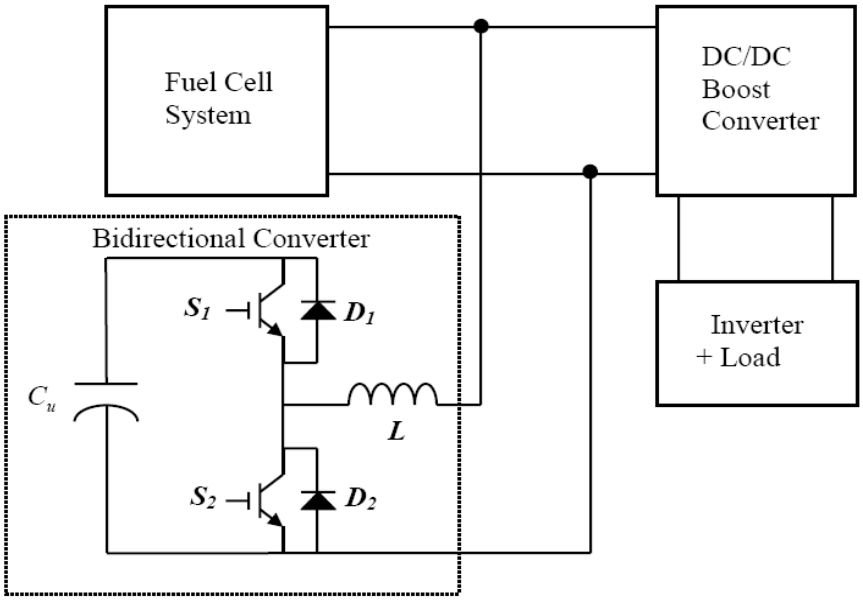

Figure 5.1 Functional diagram of the system

■ Boost mode

Since the fuel cell voltage varies from 36 V to 24 V between the lightest load and the heaviest load, the nominal voltage of ultracapacitor is set to 74V [54]. The voltage of the ultracapacitor can be charged when the fuel cell system operates in steady states by the boost operation of converter. In this mode, average small signal circuit model [40] is often derived as seen in Figure 5.2 to build up the system

transfer functions.

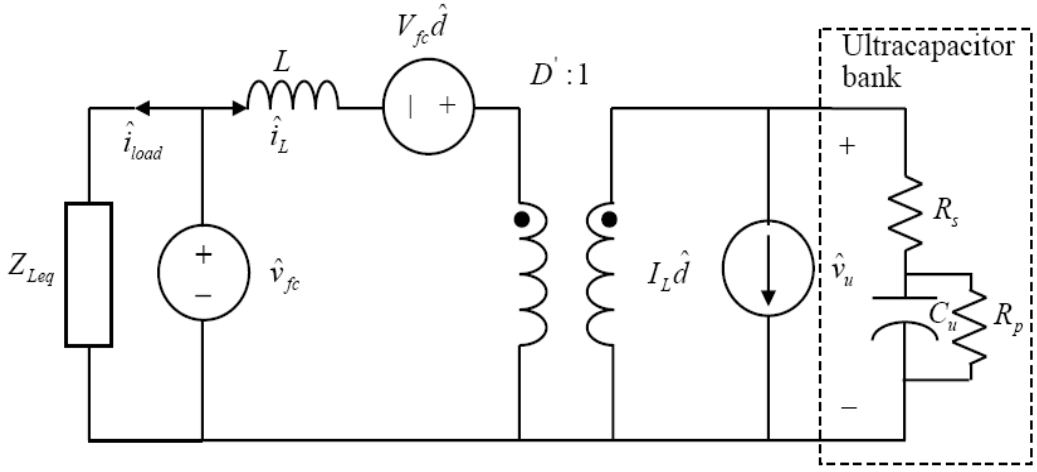

Figure 5.2 Average small signal circuit model of boost converter

Where:

$\hat{v}_{fc}$: Fuel cell terminal voltage variation,

$\hat{i}_L$: Inductor current variation,

$\hat{d}$: Duty cycle variation,

$D^{'}$: DC values of 1-*d*,

$L, V_{fc}, I_L, R_s, R_P,$ and C_u : DC values, and

Z_{Leq} : Load impedance

The ultracapacitor bank in Figure 5.2 is comprised of the equivalent series resistance R_s and the parallel resistance R_p and the capacitance C_u [58]. In the boost mode, the fuel cell voltage works like a constant voltage source, while in the buck mode, the fuel cell system is modeled with open voltage and RC model [1]. In our

study, the parallel resistance R_p is not considered in the transfer functions because R_p is significantly larger than R_s which is set to be infinite in most of analysis [58]. The transfer functions from the duty cycle to the inductor current and to the ultracapacitor voltage can be obtained based on Figure 5.2, respectively.

$$\frac{\hat{i}_L}{\hat{d}} = G_{di1}(s) = V_{fc} \cdot D' \frac{\frac{s}{L}}{s^2 + \frac{R_s (D')^2}{L} s + \frac{(D')^2}{LC_u}} \tag{5-1}$$

$$\frac{\hat{v}_u}{\hat{d}} = G_{dv1}(s) = V_u \cdot D' \frac{\frac{R_s}{L} s + \frac{1}{LC_u}}{s^2 + \frac{R_s (D')^2}{L} s + \frac{(D')^2}{LC_u}} \tag{5-2}$$

The transfer functions from the fuel cell voltage to ultracap voltage is

$$\frac{\hat{v}_u}{\hat{v}_{fc}} = G_{vv1}(s) = (D') \frac{R_s C s + 1}{LCs^2 + R_s C \cdot (D')^2 s + (D')^2} \tag{5-3}$$

The transfer function from the ultracapacitor voltage to the inductor current is as in Equation (5-4)

$$\frac{\hat{i}_L}{\hat{v}_u} = G_{vi1}(s) = \frac{Cs}{D'} \tag{5-4}$$

Each transfer function from Equation (5-1) to Equation (5-4) is very useful to construct the control system block diagram in Section 5.1.3 and analyze frequency responses through the Bode plot.

■ Buck mode

When the load current is increased, the ultracapacitor is discharged through the

buck mode converter to stabilize the fuel cell terminal voltage. Like the boost mode, an average small signal circuit model is derived.

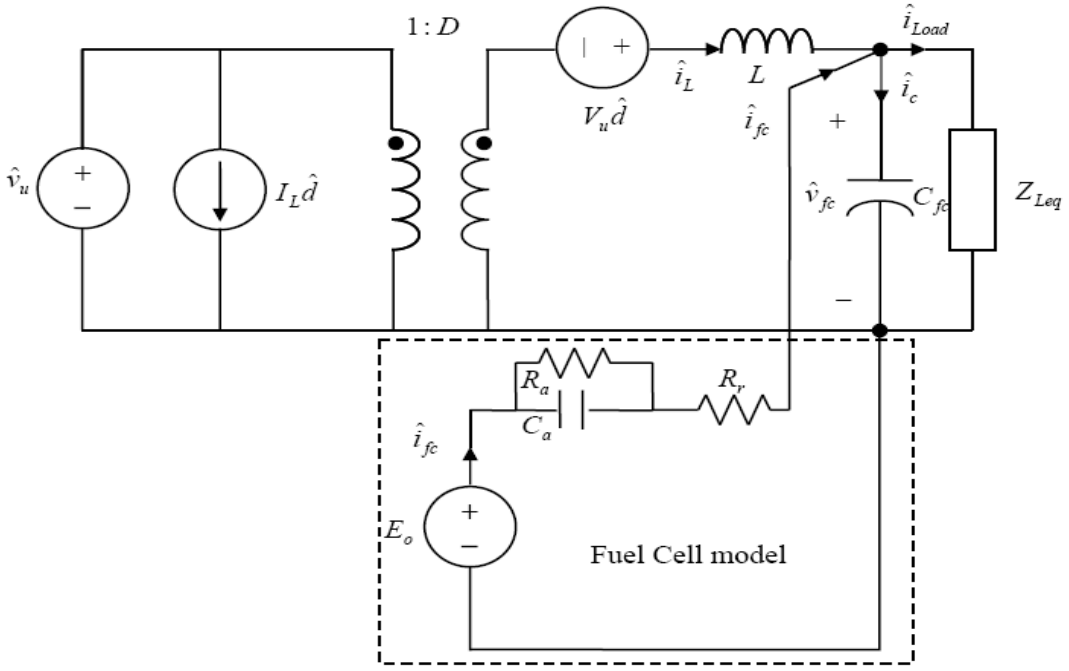

Figure 5.3 Average small signal circuit model of buck converter and fuel cell

Where:

$\hat{v}_u$: capacitor voltage variation,

$\hat{d}$: duty cycle variation,

D : DC values of duty cycle *d,*

In the fuel cell model of Figure 2.3,

$\hat{i}_{fc}$: fuel cell current variation,

E_o : open circuit voltage,

R_a : sum of the activation and concentration resistance,

C_a : Capacitive constant, and

R_r : ohmic resistance

By assuming that the impedance of E_o in the fuel cell model be less than the fuel cell's others internal impedances, the total internal fuel cell impedance [1] can be calculated by

$$Z_{fc}(s) = \left(R_a + \frac{R_a}{R_a \cdot Cs + 1} \right) \tag{5.5}$$

And the fuel cell terminal voltage can be defined as

$$V_{fc} = E_o - Z_{fc}(s) \cdot I_{fc}(s) \tag{5-6}$$

The transfer functions from duty cycle to inductor current and to fuel cell voltage can be obtained based on Figure 5.3.

$$\frac{\hat{i}_L}{\hat{d}} = G_{di2}(s) = \frac{V_u}{D} \cdot \frac{Z_{Leq} Z_{fc} Cs + Z_{Leq} + Z_{fc}}{Z_{Leq} Z_{fc} LCs^2 + (Z_{Leq} + Z_{fc}) Ls + Z_{Leq} Z_{fc}} \tag{5-7}$$

$$\frac{\hat{v}_{fc}}{\hat{d}} = G_{dv2}(s) = \frac{V_u}{D} \cdot \frac{Z_{Leq} Z_{fc}}{Z_{Leq} Z_{fc} LCs^2 + (Z_{Leq} + Z_{fc}) Ls + Z_{Leq} Z_{fc}} \tag{5-8}$$

The transfer function from the ultracap voltage to the fuel cell voltage ultracap voltage is given as

$$\frac{\hat{v}_{uc}}{\hat{v}_{fc}} = G_{vv}(s) = D \cdot \frac{Z_{Leq} Z_{fc}}{Z_{Leq} Z_{fc} LCs^2 + (Z_{Leq} + Z_{fc}) Ls + Z_{Leq} Z_{fc}} \tag{5-9}$$

As seen in Figure 5.3, even though the inductor current is coupled with the fuel cell

current, the direct relationship between the inductor current and the fuel cell voltage can be derived by Z_{fc}.

$$\frac{\hat{i}_L}{\hat{v}_{fc}} = G_{iv}(s) = \frac{Z_{Leq}Z_{fc}Cs + Z_{Leq} + Z_{fc}}{Z_{Leq}Z_{fc}LCs^2 + (Z_{Leq} + Z_{fc})Ls + Z_{Leq}Z_{fc}} \tag{5-10}$$

Specific control architectures of boost and buck modes will be described using the derived transfer functions in the following section.

5.1.3 Design of the Controller and Bandpass Filter

There are two voltage controllers: one is the ultracapacitor voltage controller and the other is fuel cell voltage controller. And the current controller controls the inductor current in the converter. The control architecture will be different in each mode because the input and output are exchanged vice versa for charging and discharging.

■ The Controller

i) Boost mode

If load variations lasts over 5 seconds and their capacities are less than the fuel cell stack capacity 5 kW, the boost mode (charging mode) is activated. In steady states of fuel cell systems, since the fuel cell voltage controller charges the ultracap voltage, the fuel cell voltage controller is placed in the most outer loop, which generates the reference ultracapacitor voltage through the BPF1, bandpass filter1 as shown Figure 5. 4. To generate the reference ultracapacitor voltage 74V, the initial duty ratio is set to D=0.527 based on the reference fuel cell voltage is assumed to be 35V because the

output voltage V_o of the boost converter is calculated by the duty ratio and the input voltage V_{in} shown in Equation (5-11) during the continuous conduction mode [59].

$$V_o / V_{in} = 1/(1-D) \tag{5-11}$$

The ultracapacitor voltage controller in the inner loop also generates the reference inductor current through the BPF2, bandpass filter2. These two bandpass filers, BPF1, and BPF2, can determine the frequency range in each control loop. For the ultracapacitor voltage controller in the inner loop, the low cutoff frequency of BPF2 is decided to be $f_1 = 100$ Hz because given any load change is slower than f_1 during boost mode, the ultracapacitor would respond. The high cutoff frequency of BPF2 is limited to be $f_2 = 10$ kHz to avoid the correlation of the switching frequency of the converter.

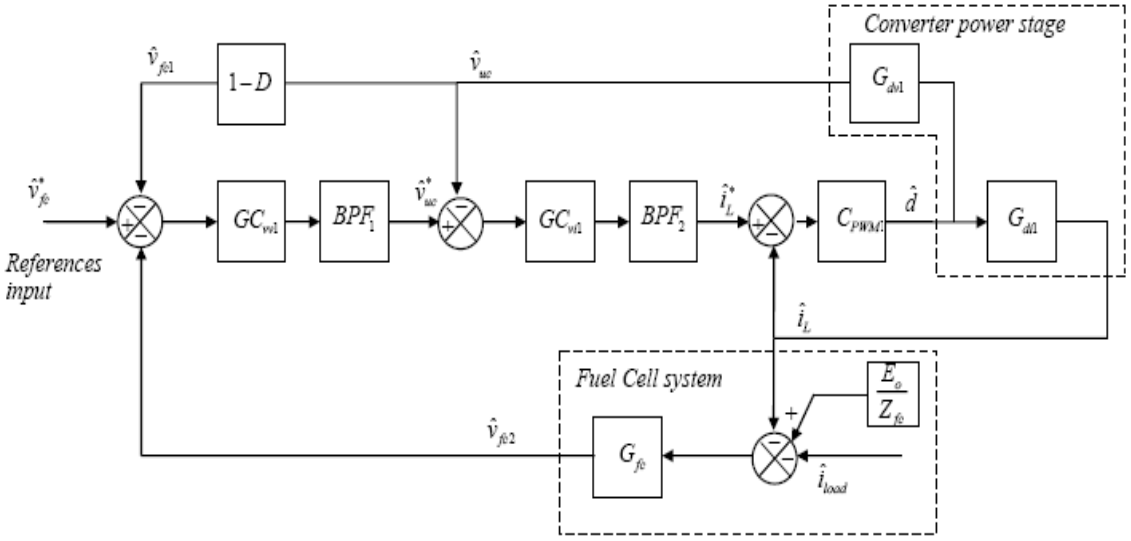

Figure 5.4 Control block diagram in the boost mode

The most outer loop cutoff frequencies of BPF1 are set to be in the range ($0.1f_1$, $0.1f_2$) [54] because it is expected to respond much slower than inner loop controller. However, in the buck mode, as the ultracap voltage will stabilize the fuel cell voltage, the ultracap voltage controller must be placed in the most outer loop.

ii) Buck mode

If the load variations last within 5 seconds and their capacities are over than 5 kW, the buck mode is activated. As seen in Figure 5.5, during buck (discharging) mode, the ultracapacitor voltage controller generates the reference fuel cell voltage and the fuel cell voltage controller generates the reference inductor current of the converter. To generate the reference fuel cell voltage 35V, the initial duty ratio is set to $D = 35/74 = 0.473$ based on that the reference ultracapacitor voltage is assumed to be 74V because the output voltage V_o of the buck converter is calculated by the duty ratio and the input voltage V_{in} given in Equation (5-12) during the continuous conduction mode [59].

$$V_o / V_{in} = D \tag{5-12}$$

Through Figures 5.4 and 5.5, the GC means the combined transfer function including the controllers. In terms of the fuel cell voltage feedback, the maximum fuel cell voltage output that is the sum of the fuel cell voltages from the buck converter and the fuel cell system are considered because the fuel cell terminal voltage is supplied by these two sources, the fuel cell and the ultracapcitor. The functions of bandpass filters are the same as in the boost mode.

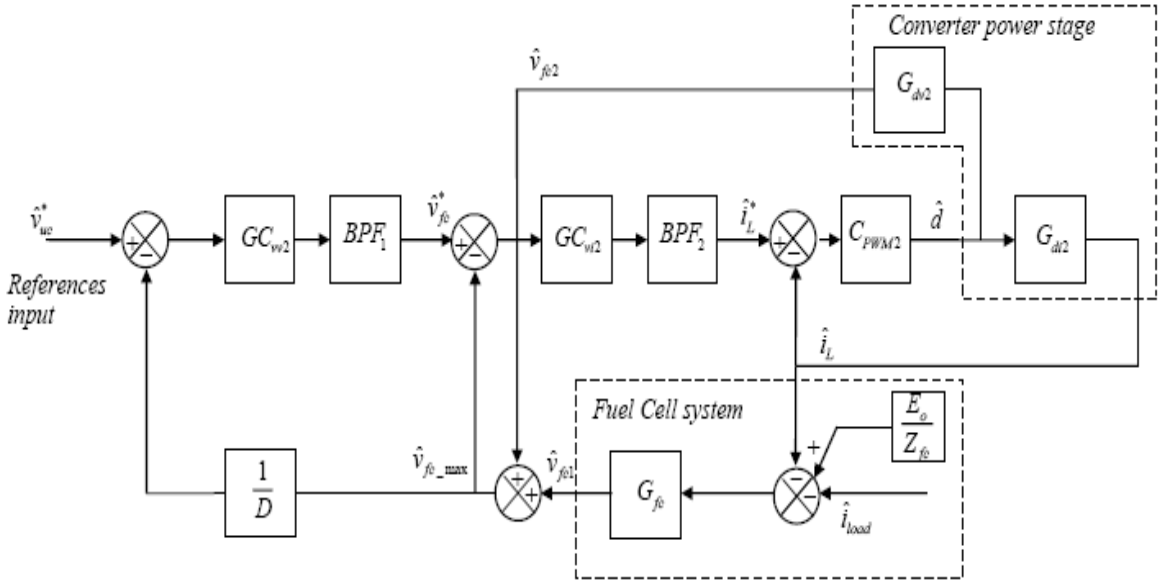

Figure 5.5 Control block diagram in the buck mode

■ Bandpass Filters Design

There are two bandpass filters, BPF1, and BPF2 in the control block diagram. The BPF1 is characterized by the frequency band $10Hz < \omega < 1kHz$ and the BPF2's passband $100Hz < \omega < 10kHz$ because the BPF1 is actually slower than the BPF2. Especially in the buck mode, for any load change which is less than the low cutoff frequency 100 Hz, the fuel cell system can respond without the help of ultracapacitor [53]. And the high cutoff frequency of BPF2 must be low enough so that it does not interact the switching frequency 10 kHz of the bi-directional converter. Hence, the high cutoff frequency of BPF2 is limited to be 10 KHz. In this research, the second order wide band pass filter [60] is used as in Equation (5-13) by letting $s \to j\omega$

$$H(j\omega) = H_0 \frac{j\omega/\omega_L}{(1+j\omega/\omega_L)((1+j\omega/\omega_H)} \tag{5-13}$$

where H_o is the mid frequency gain and ω_L is the low cutoff frequency and ω_H is the high cutoff frequency.

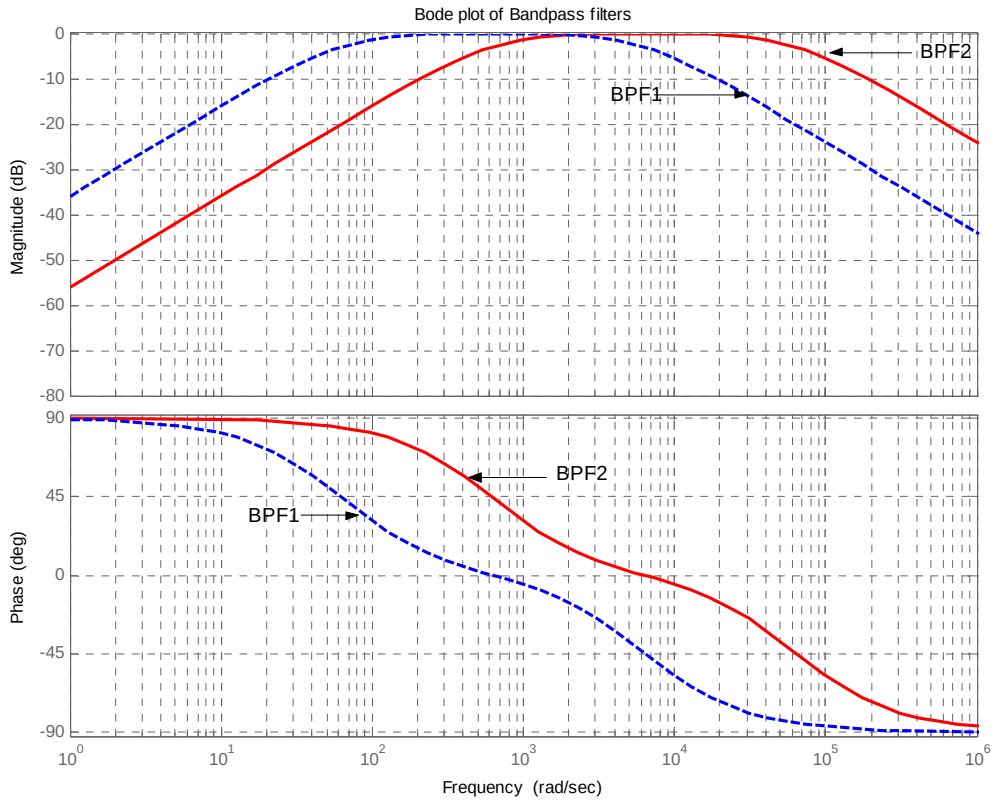

Figure 5.6 Bode plot of the bandpass filters BPF1 and BPF2

Based on the characterized cutoff frequencies in the BPF1 and BPF2, the Bode plot of the bandpass filters are shown in Figure 5.6.

5.1.4 Simulation Results

For the simulation, the 2500-ft^2 house load profile illustrated in Figure 5.7 [57] is used as a reference to calculate the transient power of the ultracapacitor.

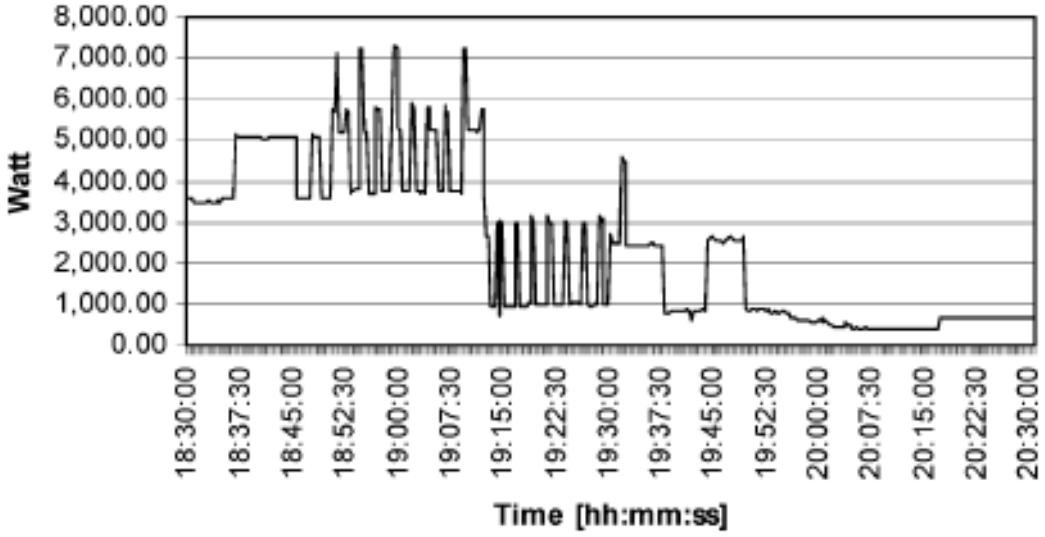

Figure 5.7 2500-ft^2 house load profile (Real power) [57]

Figure 5.7 shows that the peak loads varies from 7kW to 7.4kW and the sampling interval of load profile is 15-s. The maximum period of the peak demand is 75s when the load demand exceeds the 5kW maximum available power from the fuel cell system. By using the proposed system, the ultracapacitor is able to support the extra load of 2.4kW for 75s, which is 50W-h of energy and its minimum energy capacity rating of the ultracapacitor is 50/0.75=66.67Wh [57].

The Maxwell boostcap PC2500 ultracapacitor [61] is selected for the simulation. Its nominal voltage is 2.5V and the capacitance value is 2700F. Thus, 30 unit of ultracapcitor in series (the total capacitiace is 2700F/30=90F) is required to keep charging the reference voltage 74V through the bidirectional converter because $74\text{V}/2.5\text{V} = 29.6$. The calculated energy storage can store $0.5 \times 90 \times 74^2 / 3600 = 68.46\text{Wh}$, which can sustain the minimum energy rating of the ultracapacitor 66.67Wh. But, if we directly connect the fuel cell system with the

ultracapacitor without the bidirectional converter, 15 ultracapacitors (total 2700/15=180F) is needed because $36\text{V}/2.5\text{V} = 14.4$. And to meet the extra load demand 66.67Wh, at least two 15 ultracapacitors in parallel and extra more ultracapacitor are expected because 15 utlracapacitors in series only can store $0.5 \times 180 \times 36^2 / 3600 = 32.4$Wh, and 30 ultracapacitors can support 64.8Wh in this case. It is obvious to see that using the bidirectional converter is more beneficiary especially in saving the capacitor than only coordination with the ultracapacitor without using the converter.

The simulation is performed by a Ballard 5 kW PEMFC fuel cell stack model MK5-E composed of 36 cells; each cell has a 232 cm^2 active area, graphite electrodes, and a Dow membrane [25, 39]. Experimental data from J. Hamelin et al. [39] were used to compare the validity of the proposed system. The voltage and the current, the most important variables, were used for this comparison. In [39], a load profile with rapid variations between 0 and 150 A was imposed on the PGS-105B system. The corresponding stack current and voltage transients are plotted in Figure 5.8, where the experimental data [25] are indicated by solid lines. The details of load profile are shown in Figure 3.3, where the load resistances were changed from 0.119 Ω to 4.15 Ω during the simulation period.

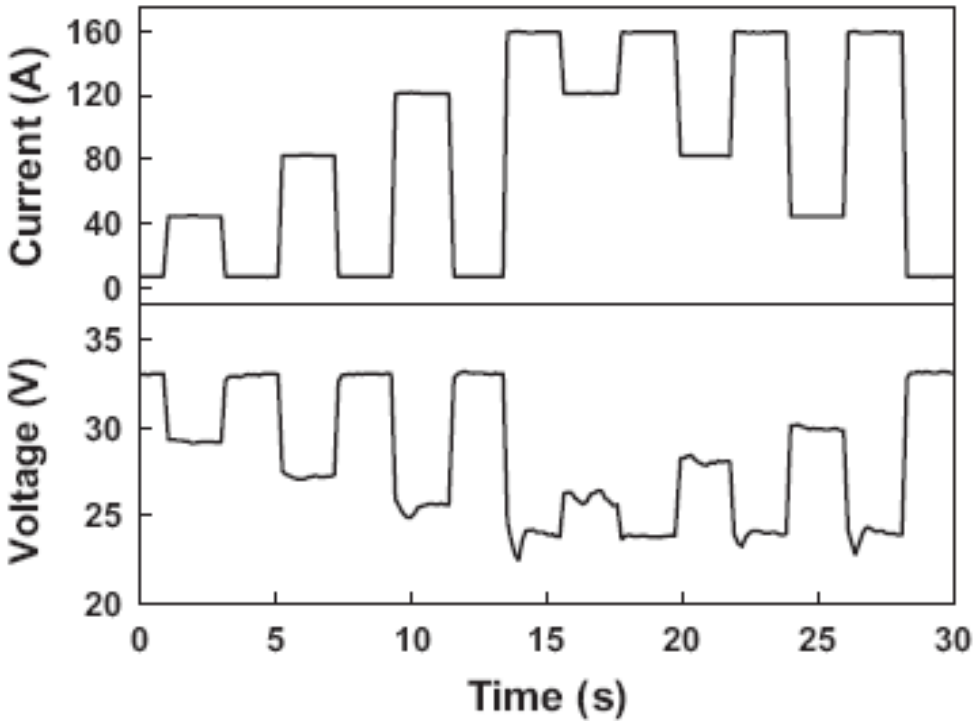

Figure 5.8 Fuel Cell current and voltage under load variations [39]

As shown in Figure 5.8, the fuel cell terminal voltage drops below 25 V. The rapid current increase can cause an immediate voltage drop across the internal resistors (activation and concentration) of the fuel cell. Based on the frequent load changes in Figure 5.7, normally buck mode (discharging) is imposed to the system.

The value of the inductor of the bidirectional converter is set to 1 mH to operate the boost and buck mode properly without high surge voltage. With the help of the ultracapacitor and bidirectional converter, the fuel cell terminal voltage does not drop below 30 V. But when the load resistance is changed from the smallest value 0.119 Ω to the biggest value 4.15 Ω, a 2~3 V voltage spike can be observed.

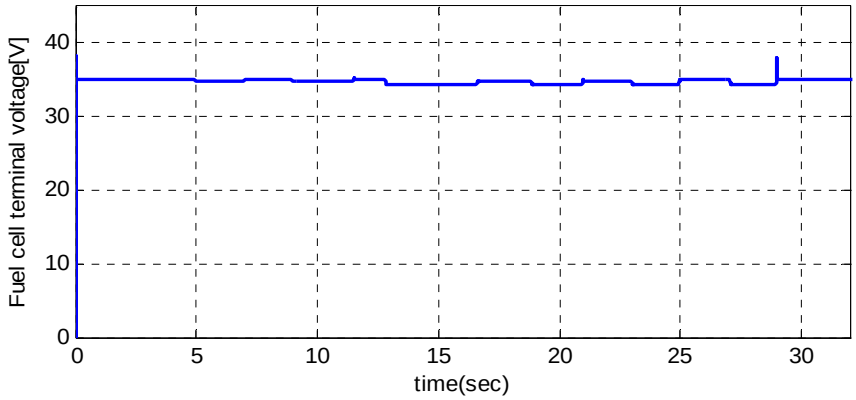

Figure 5.9 Fuel Cell Terminal voltage (discharging mode)

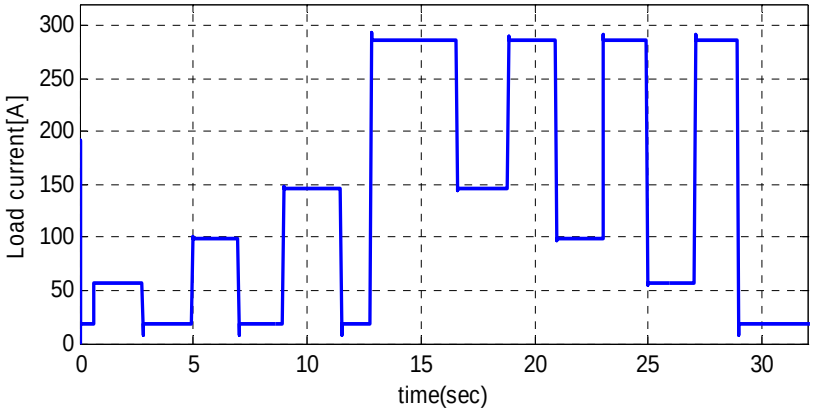

Figure 5.10 Load current (discharging mode)

Thus, in case of a sudden load change with a big variation, the surge protection should be mounted. In the simulation, the surge protection arrestor which has the maximum limit with 50V and 200A, is used.

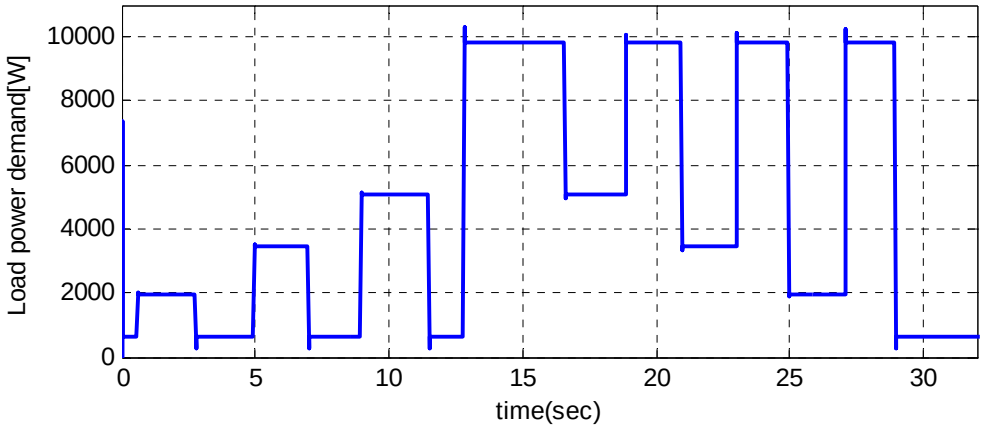

Figure 5.11 Load power demand (discharging mode)

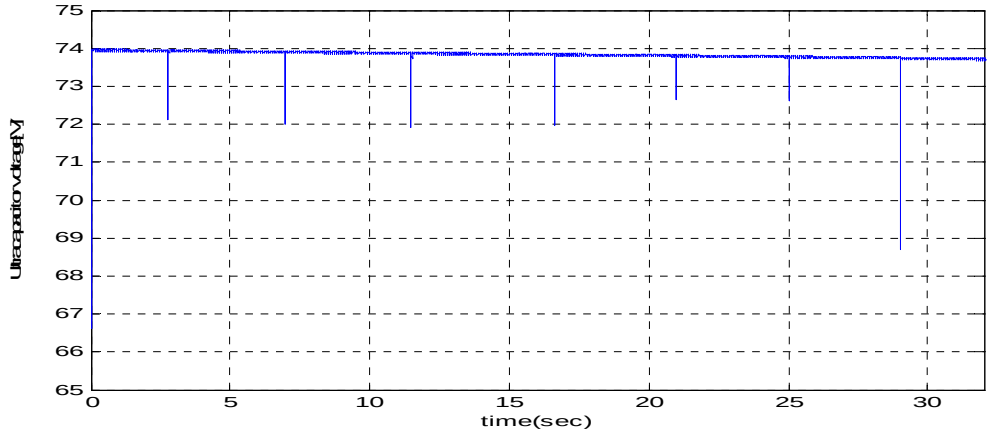

Figure 5.12 Ultracapacitor voltage (discharging mode)

Figures 5.10 and 5.11 show the load current and load power demand respectively. Due to the ultracapacitor and bidirectional converter, the load current lifts up to 290A and the load power demand can reach up to 10 kW. To utilize the total load power demand 10 kW, the additional ultracapacitor bank 90 F is needed because one 90 F ultracapacitor bank and the fuel cell stack can only support the total power of 7.4kW.

The ultracapacitor voltage gradually decreases and a voltage drop can be observed until 68.7 V due to sudden load changes as shown in Figure 5.12.

In case of a light load change in which the total load power demand is less than 5 kW and the load change duration is beyond 5 seconds, the boost mode (charging mode) is imposed.

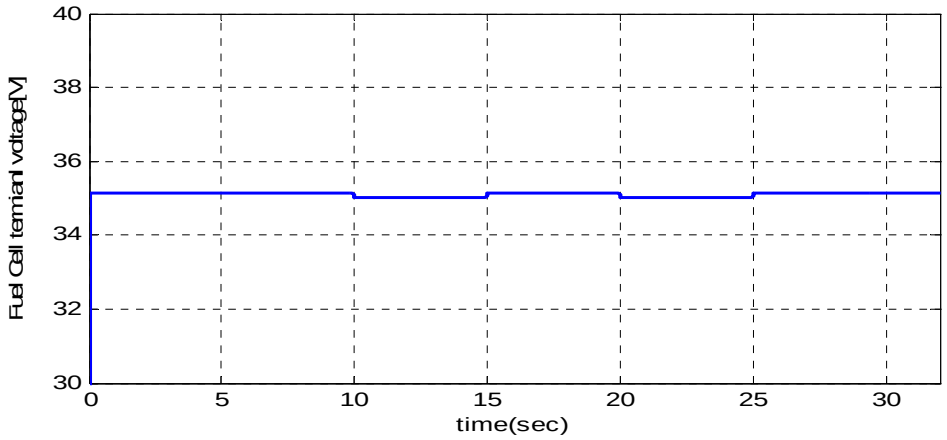

Figure 5.13 Fuel cell terminal voltage (charging mode)

The fuel cell voltage varies between 35V±0.3V because of the light load as seen in Figure 5.13. The load power varies less than 5 kW and the load current is changed between 18A and 58A in Figure 5.14.

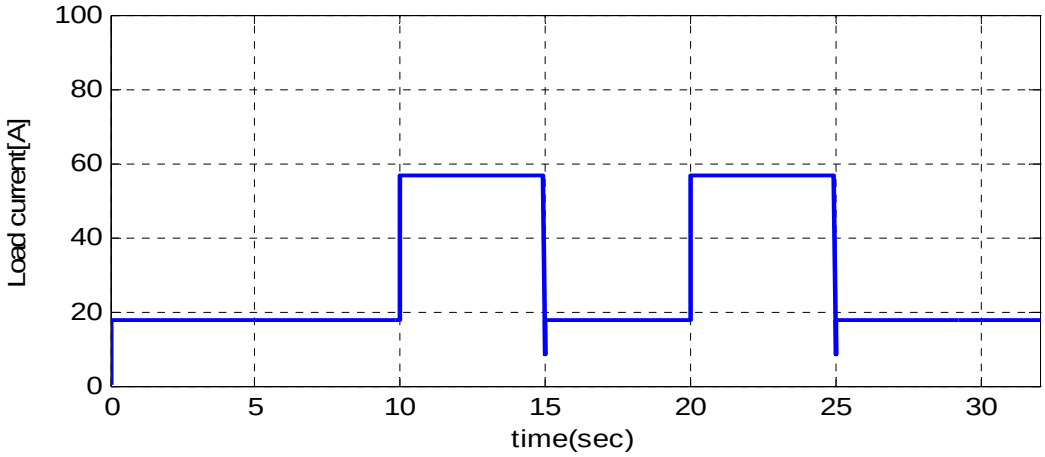

Figure 5.14 Load current (charging mode)

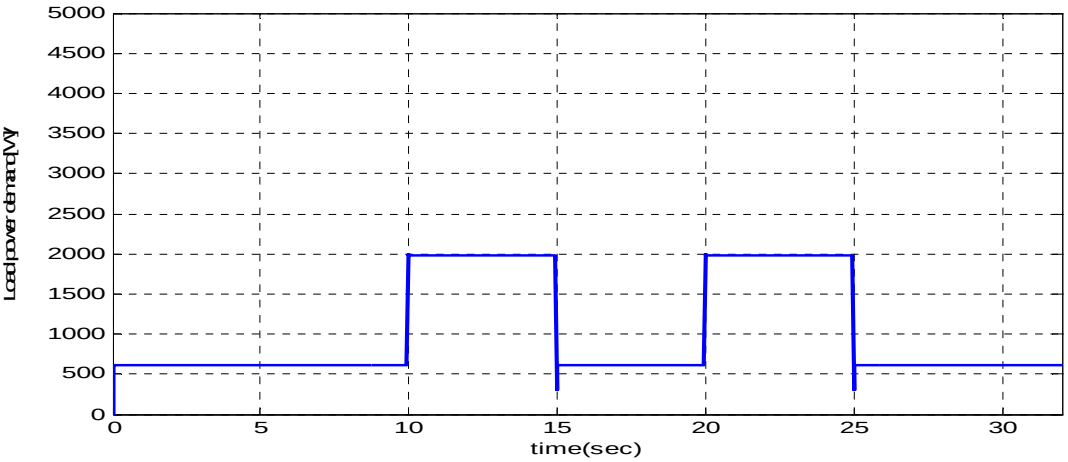

Figure 5.15 Load power demand (charging mode)

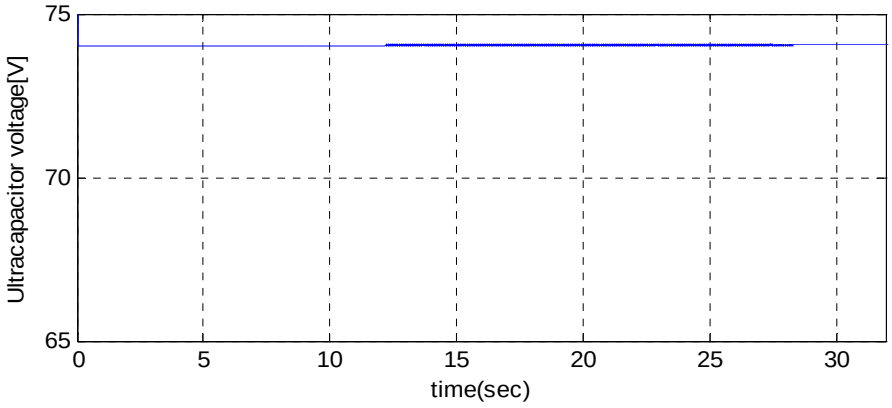

(a)

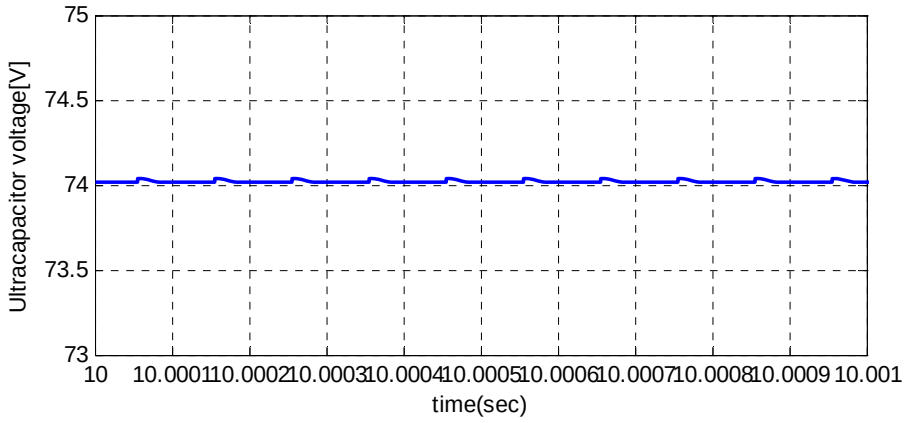

(b)

Figure 5.16 Ultracapacitor voltage (charging mode):
(a) Total time duration, (b) Zoom in between 10seconds and 10.001 seconds

To avoid an inrush current during the charging period, the initial condition of the ultracapacitor is set to 70.3 V, 95% of the reference voltage. As seen in Figure 5.16(b), a 10kHz ripple can be found due to the switching frequency of the converter.

5.2 Supervisory Control of PEMFCs, PV and UC Hybrid power system

5.2.1 Introduction

Lately several supervisory control studies regarding hybrid power systems (PV (Photovoltaic), wind and battery) [57, 62, 63] have been proposed for stationary applications, however, which does not include a fuel cell system. Since other studies [64-66] about the hybrid power systems including a fuel cell system, are deeply focusing on integration of hydrogen production, a supervisory control algorithm has not been developed for them.

This study is more concerned to develop a supervisory control algorithm for the hybrid power system consisting of PEMFCs, PV subsystems and energy storage. A 5kW PEM fuel cell system is considered for the residential system and the nominal voltage of ultracapacitor for the energy storage is set to 40V. For a fast load change, the fuel cell current slope should be limited to $4As^{-1}$[8] as mentioned in Section 5.1. And during the peak power period, the total maximum power is able to reach 10 kW. Hence, the power demand beyond 5kW, the fuel cell power capacity can be supplied by a PV system to cover a total load demand 7.5kW. And beyond the 7.5 kW, the sum of the fuel cell power and PV power capacity, the energy storage system, an ultracapacitor can generate the remaining power up to 2.5kW such that 10.0 kW, the total maximum load demand power, can be covered.

In the light load (less 5kW) and steady state conditions, the ultracapacitor is set to be charged via the supervisory control. The surplus energy from the fuel cell system and PV system also can be used to charge the ultracapacitor system. Hydrogen

production through the use of surplus energy for the fuel cell system is out of the scope of this paper to avoid the complexity of the system. This supervisory control fuel cell, PV and ultracapcitor hybrid system is tested using Matlab/Simulink.

5.2.2 PV System Modeling

The fuel cell system and ultracapacitor are already modeled in Section 2.3 and Section 5.1.2. In this section, the PV subsystem will be described.

■ PV Generation

The traditional I-V characteristics of a PV array are given by Equation (5-14) [62].

$$I_{pv} = n_p I_{ph} - n_p I_{rs}\left[\exp\left(\frac{q}{KTA}\frac{V_{pv}}{n_s}\right) - 1\right] \tag{5-14}$$

where:

I_{pv} : PV array output current (A);

V_{pv} : PV array output voltage (V);

n_s : Number of cells connected in series;

n_p : Number of modules connected in parallel;

I_{ph} : Photocurrent; I_{rs} is the cell reverse saturation current;

q : Charge of electron, 1.6×10^{-19}C;

K: Boltzmann's constant, 1.385×10^{-23}Nm/K;

A: P-n junction ideality factor; and

T: Cell temperature (Kelvin);

The factor A in Equation (5-14) is related to the solar cell deviation from p-n junction characteristics, in here, A is set to 2.46 [62]. The equivalent circuit of PV cell is given in Figure 5.17 [62]. R_{sh} is the intrinsic shunt resistance and R_s is the series resistance. The equivalent circuit can be simplified as in Figure 5.17.

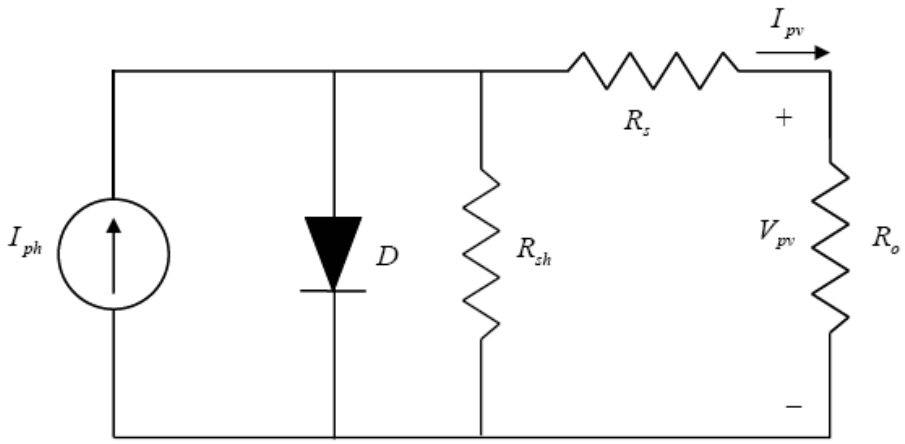

Figure 5.17 Equivalent circuit of PV cell [62]

The photo-current I_{ph} is varying with solar radiation S(mW/cm2) and temperatures are given in the Equation (5-15) [67].

$$I_{ph} = \left(I_{sc} + k_i\left(T - T_r\right)\right)\frac{S}{100} \tag{5-15}$$

where:

I_{sc} : Cell short circuit at reference temperature T_r 301.18K [62]

k_i : Short circuit temperature coefficient, 0.0017A/^{o}C [62]

S: Solar radiation in mW/m^2

The cell reverse saturation I_{rs} also varies with temperature and can be expressed

as Equation (5-16) [62]

$$I_{rs} = I_{rr}\left(\frac{T}{T_r}\right)^3 \exp\left(\frac{qE_g}{KA}\left(\frac{1}{T_r}-\frac{1}{T}\right)\right) \tag{5-16}$$

where:

I_{rr} is the reverse saturation current at T_r , 3,27A [62];

E_g is the band-gap energy of the semiconductor used in the cell,1.1V [62].

Hence, the power of PV arrays can be expressed as follows:

$$P_{pv}=V_{pv}I_{pv} = n_p I_{ph} V_{pv} - n_p I_{rs} V_{pv}\left[\exp\left(\frac{q}{KTA}\frac{V_{pv}}{n_s}\right)-1\right] \tag{5-17}$$

Using the conventional Maximum-Power-Point-Track (MPPT), $dP/dV = 0$, the maximum output power point can be obtained by the following equation.

$$\exp\left(\frac{q}{KTA}\frac{V_{\max}}{n_s}\right)\left(\frac{q}{KTA}\frac{V_{\max}}{n_s}+1\right) = \frac{I_{ph}+I_{rs}}{I_{rs}} \tag{5-18}$$

In this research, there are more concerns about supervisory control of the hybrid system other than developing MPPT algorithm.

5.2.3 Supervisory Control of the Hybrid Power System

In this section, the supervisory control algorithm for hybrid power system is presented. The configuration of the hybrid power system with PV panel, PEM fuel cell and energy storage is given in Figure5.18. In Figure 5.18, P_L , the power supplied to the load, is the sum of output power from the fuel cell generator P_{fc} , the PV panel P_{pv} , and

energy storage power P_{uc} that has a bidirectional power flow according to energy inside and outside of UC (Ultracapacitor) system. The total energy is balanced

$$P_L = P_{fc} + P_{pv} \pm P_{uc} \tag{5-19}$$

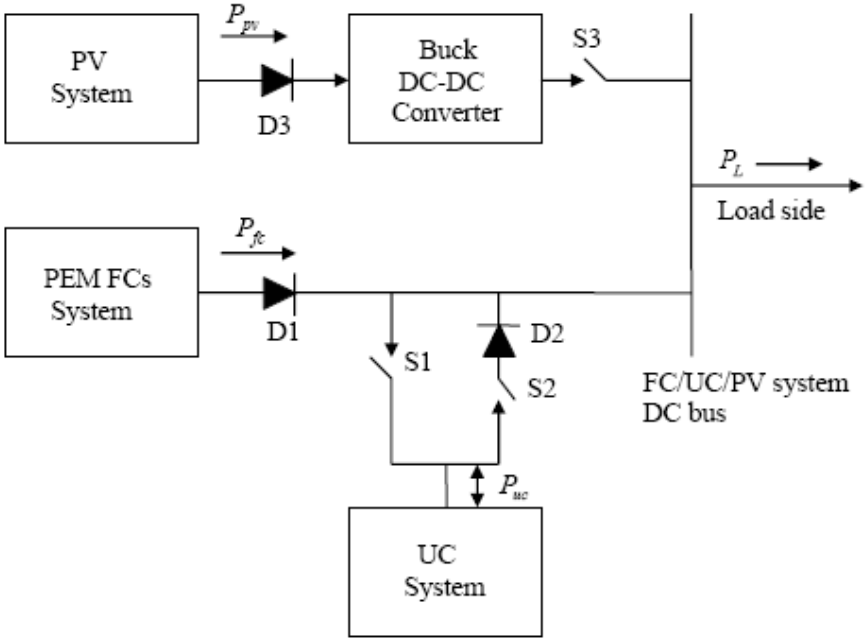

Figure 5.18 Configuration of the hybrid power system

The load in Figure 5.18 includes the energy used to the power conditioning unit (dc/dc converter and dc/ac inverter) and the residential load. And the auxiliary power for the fuel cell, the PV subsystems and the converters are not considered because it is a small portion comparing with the produced powers by the PV, fuel cell, and energy storage. The basic idea of supervisory control strategy is that the fuel cell generator generates up to 5kW, its maximum power, while the remaining ($P_s - P_{fc}$) is supplied by the PV subsystem and energy storage according to sunlight conditions. The

conditions and the role of the energy storage (either storing or supplying energy) define different modes of the systems. Hence, a supervisory control is critical to efficiently manage the operation of the subsystems according to different situations. Note that the fuel cell system plays the main role in power generation, whereas the PV and the energy storage subsystems would play a secondary role.

Four possible modes of operation in the system are defined as follows.

i) Mode 1

If the fuel cell power is sufficient to satisfy the total power demand, only the fuel cell subsystem is activated over the diode D1 while the PV system is inactive by setting off condition of the switch S3 and the energy storage system is in energy storing mode by closing the switch S1, absorbing the surplus power ($P_L - P_{fc}$). For the case that the total power demands exceed the maximum power that the fuel cell generator can provide, the supervisory control switches the hybrid system to Mode 2 and activates the PV system.

ii) Mode 2

The supervisory control has the fuel cell generator to generate the maximum power over the diode D1 and the PV cell system to be active to track a load power reference using MPPT algorithm over the diode D3 since the switch S3 is closed. The energy storage system is not requested to supply energy until the total power demand exceeds the sum of the fuel cell power (5kW) and PV power (2.5kW), and it would keep storing the difference between the total power demand and power sum of the fuel cell and PV systems by closing the switch S1 as long as it stays in Mode2. Once the

total power demand exceeds the maximum generation of the fuel cell and PV systems, the mode of the hybrid system will be transferred to Mode 3.

iii) Mode 3

The fuel cell system and PV system power are transferred to the load over the D1 and the S3 (closed state). Moreover, the energy storage system will be discharged through the diode D2 by closing the switch S2, acting as a power supplier. The reverse current can not flow from the energy storage system to the fuel cell system and PV system because of the blocking diode D1 and D3. The operation of Mode 3 continues as long as the total generation power capacity including the energy storage output is able to supply the total power demand range between 7.5kW and 10kW. If the total power demand goes beyond the maximum capacity (10kW) of the hybrid system, the load must be disconnected from the power supplies to avoid damages of the hybrid system, and the system enters Mode 4.

iv) Mode 4

This is an emergency mode defined for the security purpose since the hybrid power system is unable to supply enough power to the load power demand. The load is disconnected and the protection mode is enforced for the hybrid system as well as the power conditioning unit. The power capacity of each subsystem must be carefully designed to meet the load demand such that the hybrid system can be protected by the supervisory control algorithm.

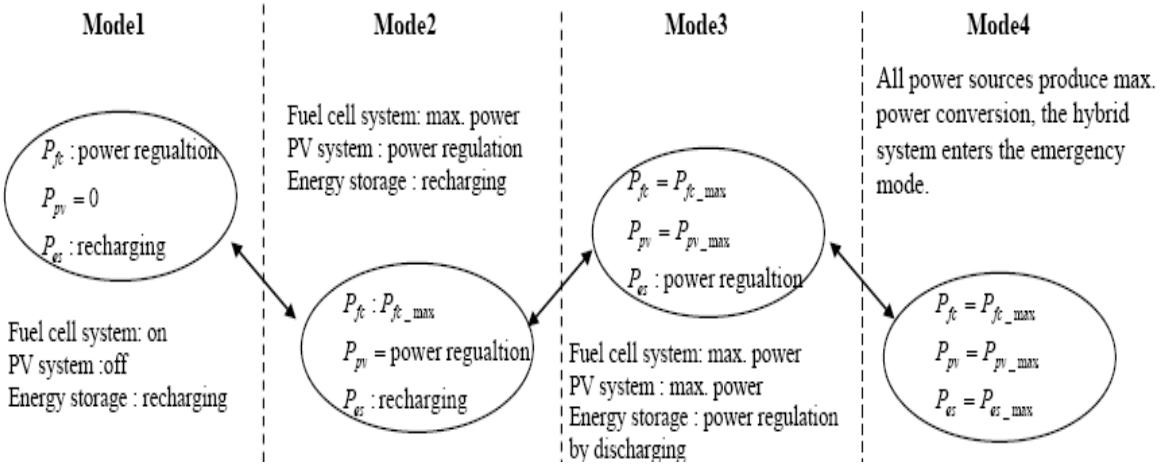

Figure 5.19 Schematic diagram of mode operation

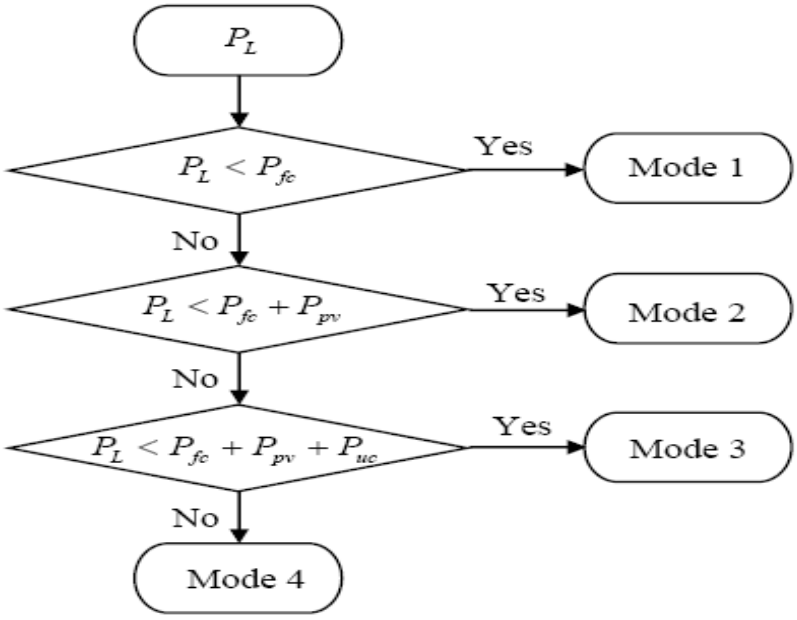

Figure 5.20 The flowchart of the supervisory control

In summary, the supervisory control is able to allow changes from one operation mode to another according to the undergoing sunlight conditions, the load demand and the energy storage system conditions (charging or discharging). The details of the

control design can be further understood through the schematic of mode operation and flowchart in Figures 5.19 and 5.20, respectively.

5.2.4 Simulation Results

In the simulation, we assume that the peak load could reach 10 kW and the PV system for the peak load shaving is available for day time with a clear sunlight. And the maximum period of the peak demand is assumed to be 75s when the load demand exceeds the 7.5kW, the maximum available power capacity of the fuel cell system and the PV system. Furthermore, the ultracapacitor is able to support the remaining load of 2.5kW for 75s, which is 52.1W-h of energy and its minimum energy capacity rating of the ultracapacitor is 52.1/0.75=69.47Wh [57].

The Maxwell boostcap PC2500 ultracapacitor [61] is also selected for the simulation. Its nominal voltage is 2.5 V and the capacitance value is 2700F. Thus, at least 16 units of ultracapcitor in series (the total capacitance is 2700F/16=168.75F) is required to keep charging the reference voltage 40V (=16 x 2.5V) through the control algorithm. The energy storage system can store $0.5 \times 168.75 \times 40^2 / 3600 = 37.5\text{Wh}$ by calculation, which can not sustain the minimum energy rating of the ultracapacitor 69.47Wh. Thus, to meet the remaining load demand 66.67Wh, at least two 16 ultracapacitor units in parallel are expected because 16 utlracapacitors in series only can store 37.5Wh.

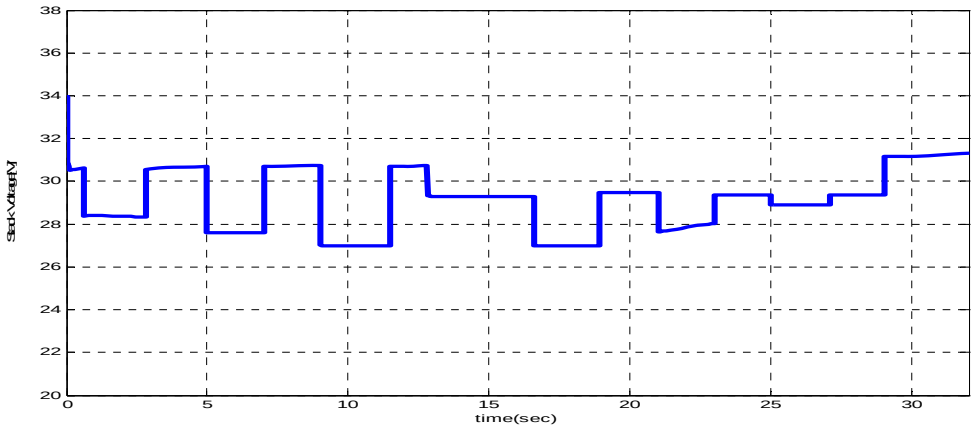

(a)

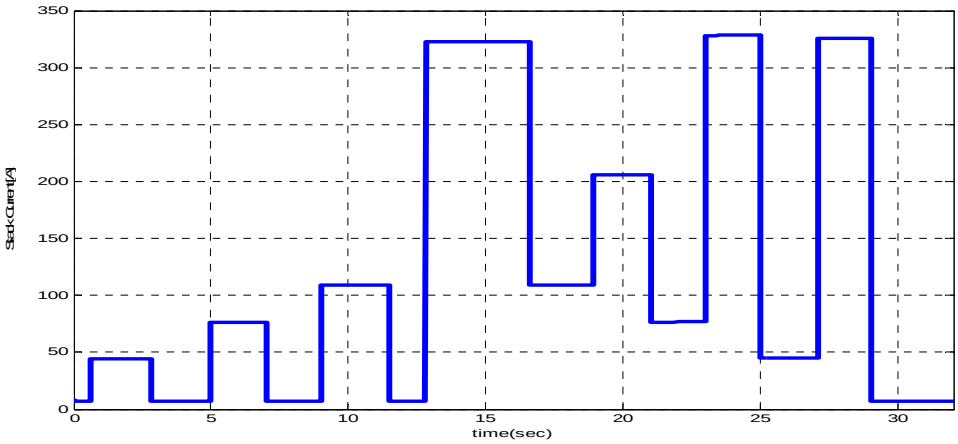

(b)

Figure 5.21 Fuel Cell Terminal voltage and current of the hybrid power system: (a) Voltage, (b) Current

As shown in Figure 5.8, the fuel cell terminal voltage drops below 25 V if only fuel cell system is operated. The fuel cell terminal voltage of the hybrid power system does not drop below 27V by using the supervisory control as seen in Figure 5.21. However, as seen Figure 5.19, using bi-directional converter is a better option to

compensate the fuel cell voltage drop than a supervisory controlled hybrid system. In this simulation, although the same load profile as in Figure 3.3 is used, the current is over 300 A and the total power demand is over 9 kW due to less voltage drop as seen in Figures 5.21 and 5.22.

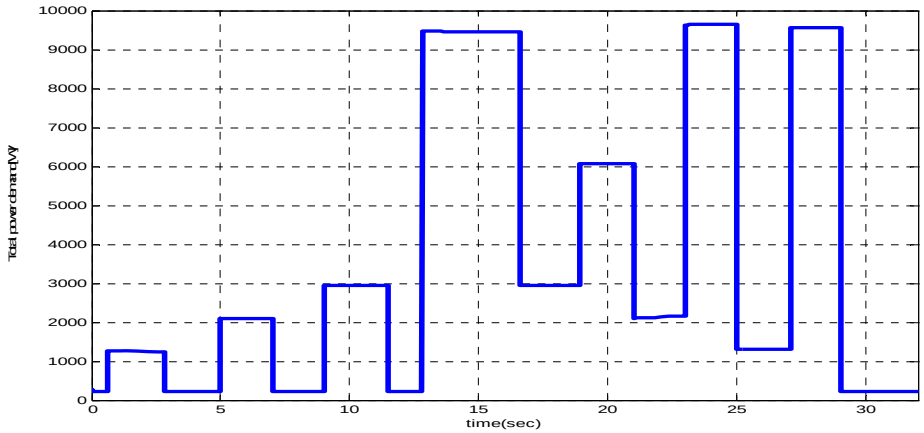

Figure 5.22 Total Power demand

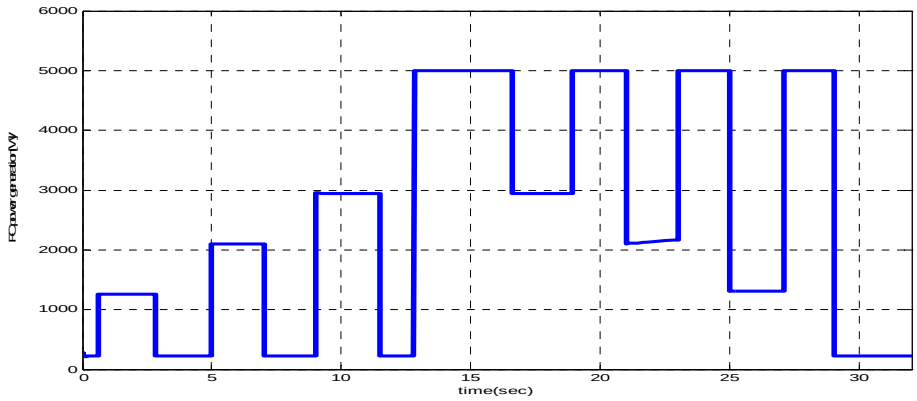

Figure 5.23 FC power generation

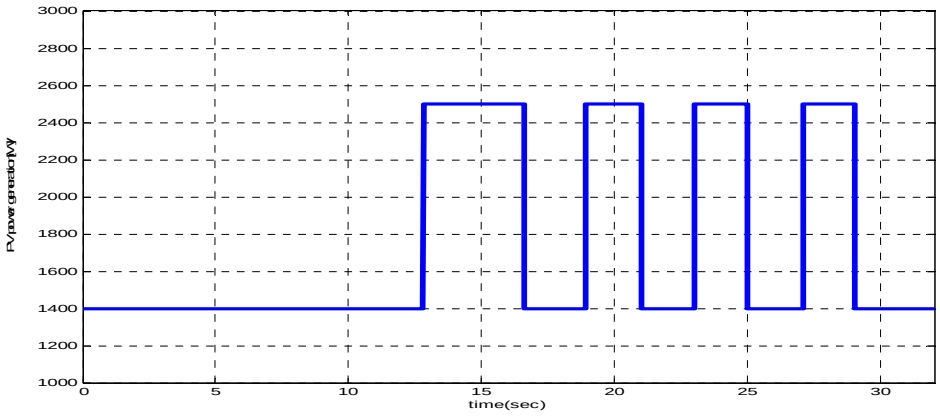

Figure 5.24 PV power generation

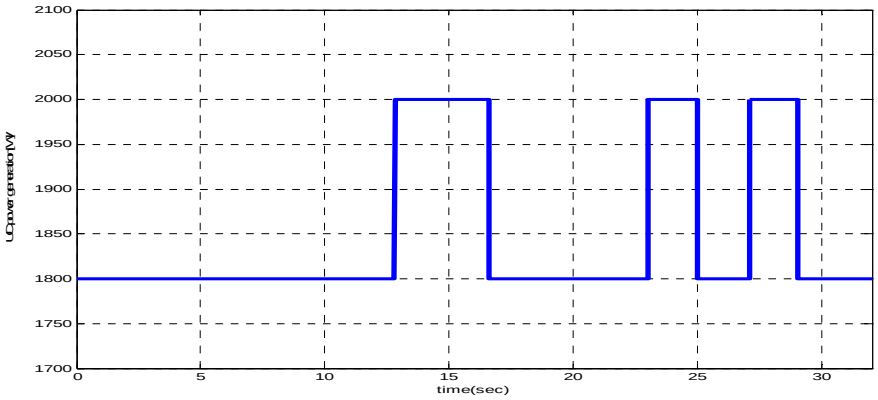

Figure 5.25 UC power generation

According to the propose supervisory control, Figure 5.23 shows that the FC system generates the maximum 5 kW power, and Figure 5.24 shows that the PV system can compensates the power up to 2.5 kW whenever the total load power demand is over 5kW. The UC (Ultracapacitor) system also can cover the remaining 2.5 kW if the total load power demand ranges from 7.5 kW to 10 kW. But in this simulation, since the maximum power load is 9.5kW shown in Figure 5.22, the maximum value 2.0 kW of UC system shown in Figure 5.25 is enough to cover the total power demand.

CHAPTER 6

CONCLUSION

6.1 General Conclusion

Most of my research is dedicated to developing a fuel cell dynamic model, its nonlinear control algorithm, and an optimal design for PEMFCs. With respect to the dynamic model and nonlinear control of PEMFCs, a feedback linearization-based nonlinear control design of dynamic PEMFCs has been developed [28]. As for the optimal design of PEMFCs, a multi-objective optimization study about PEMFCs has been investigated [6]. Furthermore, other control designs for water, heat management, and a power electronics interface design, a supervisory control of hybrid system (Fuel cell/Solar cell and Energy storage) have been studied. The conclusions of these works are summarized as follows:

First, this research work proposes a MIMO dynamic nonlinear model for PEMFC and presents a design for a nonlinear control for polymer electrolyte membrane fuel cells using feedback linearization. By adapting all water effects in the proposed dynamic model of PEMFC, we are able to investigate a more accurate transient behavior of the PEMFC. The MIMO nonlinear dynamic model is developed for PEMFC, which enables the creation of a platform for the design of a nonlinear control strategy using feedback linearization. The feedback linearization technique can cancel

the nonlinearities of the system and impose desired linear dynamics.

As illustrated by the Matlab/Simulink simulation results, the transient responses of the proposed nonlinear controller are superior to those of the conventional PI controller under load variations, which can prolong the fuel cell stack life by reducing the pressure differences between the anode and the cathode as much as possible.

However, in order to apply the proposed control algorithm for the fuel cell, exact measurements of water formation and other states must be guaranteed. Fortunately, several approaches [68, 69] to the measurement of the states of the fuel cell have recently been published, and the proposed nonlinear control strategy is likely to apply to the design of an overall control scheme for PEMFC, including the water and heat management systems, the fuel processor, and the air compressor.

Second, a new thermal equivalent circuit for the PEMFC is proposed. The analysis for the design of the PEMFC temperature controller is performed by using Bode plots of the thermal equivalent circuit transfer functions. The Bode plots show that the lag compensator with small PI gains is a good option for the design of the temperature controller for PEMFC. In addition, the proposed temperature controller is analyzed by comparing with the experimental results and Matlab/Simulink simulations. This paper has obtained some analytical results that provide a useful suggestion for the design of a temperature controller for PEM fuel cell systems.

Third, a joint optimization model of fuel cell system efficiency and cost is proposed. A multi-objective optimization technique, the SQP (sequential quadratic programming) method, has been applied to investigate the impact of the variations of

initial conditions on the efficiency and the cost of fuel cell system. Although the study shows that the change of air stoichiometric ratio is more closely related to the fuel cell efficiency and cost than any other variables in impractical region, the system pressure, hydrogen and current density must be appropriately selected for the optimal design because they also largely affect the fuel cell system and cost as well in the our study. Our work presents a way to determine the optimal design regarding the fuel cell efficiency and cost aspects simultaneously.

Fourth, this dissertation discusses the control method of boost and buck converter for the fuel cell stationary power applications. Through the simulation and comparing the experimental results, it shows that the proposed system not only improves the dynamic response of the fuel cell system, but it also can significantly compensate the voltage drop of the fuel cell system due to load changes. This control study based on the PEM fuel cell system, the ultra-capacitor model and the bidirectional converter together, which can provide a good platform to design a suitable power converter control system for fuel cell system applications.

Last, a supervisory control algorithm for a proposed hybrid power system, which consists of a fuel cell system, a PV system and a ultracapacitor for stand-alone stationary power applications is proposed. Through the simulation and comparison of the test results, it shows that the proposed hybrid system with the supervisory control not only improves the dynamic response of the fuel cell system, but it also can compensate the voltage drop of the fuel cell system due to load changes. But using bidirectional converter can compensate the fuel cell voltage drop more than just using

switching through the energy storage, ultracapacitor. The supervisory control strategy proposed in this paper for the PEM fuel cell system, the PV system and the UC system together, paves a way to supply safe electricity for stand-alone residential areas by renewable energy.

6.2 Future Research

The research works in my dissertation regarding a fuel cell system and power electronics have motivated me to a further research in a nonlinear control and power electronics design related to fuel cell systems and other renewable energy systems. Following three topics will be a possible future works.

6.2.1 Supervisory Control of Hybrid Power Systems using Wind, Solar, and Fuel Cells

There are two scopes of hybrid power systems. The first is a transportation application such as a fuel cell vehicle. Since a fuel cell system has slow dynamics by nature, it is recommended to have an additional auxiliary power source such as an ultra-capacitor or battery for acceleration or deceleration to improve system performance. Thus, a control strategy to synchronize between the main power source (fuel cell) and the auxiliary one has been studied to avoid the fuel starvation and fuel cell damage during transient energy delivery or recovery.

In my proposed study, a hybrid PV (photovoltaic)/fuel cell system is considered, and then it is found that the reliability of the PV system can be improved by using fuel cell and energy storage systems simultaneously based on a supervisory control algorithm. By this method, the efficiency of the hybrid PV/fuel cell system is increased

more than the fuel cell hybrid system. This supervisory control strategy will be proposed and will then be validated using a simulation and 1-kW prototype fuel cell test equipment.

The second is a stationary power application as a distributed generator. The proposed stationary hybrid power system consists of a wind turbine, a photovoltaic system (PV), a fuel cell, an electrolyzer, an energy storage-like battery, an ultra-capacitor, flywheel, a diesel generator, and several other power converters. Through the analysis of this system based on the simulation and the validation of the prototyped hybrid power system (each system will be less 50kW), it will be identified that the proposed system can supply high-quality power even including a grid on and off control and thus represents one of the best candidates for a future renewable power system.

6.2.2 Power Converter and Control Designs for Renewable Power Systems

Fuel cell voltage is highest when no load is applied, and it drops with increasing current due to the activation of over-voltage and ohmic resistance losses in the membrane. At high currents, the voltage drops significantly because of the slow dynamics of fuel cell systems (several seconds). Likewise, a wide-input-range power converter for fuel cell systems is desired. Hence, a new wide-range power converter, along with a robust power control and high efficiency, will be examined and tested. In transportation and stationary applications, utilizing an inverter is necessary for DC-to-AC power conversion, and therefore the effect of inverter ripple on the fuel cell stack performance should be investigated. To avoid the situation in which the fuel cell performance is degraded if the ripple currents are not adequately controlled, a shunt-

type active power-filter system can be one of the solutions. The optimal control strategy of this active power-filter system will be analyzed and tested through the simulation and experiment.

Also, with respect to the power conversion system of solar cell systems is one of the prominent research topics in renewable energy systems. To develop a maximum power point tracking algorithm (MPPT), many research projects are undergoing. The proposed approach is to use a nonlinear control algorithm and therefore a maximum power point tracking controller for solar cell systems will be investigated using the experiment and simulation.

In addition to solar and fuel cell systems, wind turbine control system can be another good research aspect of renewable energy systems because wind power keeps varying with wind speed. Below rated wind speeds, real power from the wind generator is regulated to obtain the maximum energy from varying wind speed. Above rated wind speeds, the maximum power control must be regulated by stalling the wind turbine to keep the constant power. So, a nonlinear control based power controller for the wind system will be analyzed and tested through the experiment and simulation.

6.2.3 Dynamic Modeling and Control of other fuel cells(DMFC and SOFC)

In order to utilize PEMFCs, the reformation from the fuels such as ethanol, methanol, and natural gas or direct use of hydrogen is required. The reformer for the reformation of fuels makes the fuel cell system more complex, expensive, and slow. In addition, the direct use of hydrogen brings with it issues regarding the appropriate and safe transportation and storage of the fuel.

Thus, an alternative method, such as direct-methanol fuel cells (DMFCs), which involves using a liquid methanol fuel directly without reformation, is preferable for a fuel-cell-based mobile power supply system in the power range from a few watts to several hundred kilowatts than are PEMFCs. For this reason, DMFCs will be another research topic for me to develop as a dynamic model and nonlinear control design. The proposed model and control system for DMFCs can be validated through the simulation and experiment.

In terms of solid oxide fuel cells(SOFCs) research, this will focus on the development of advanced energy systems. Hybrid systems consisting of solid oxide fuel cell system and gas turbine, offer the potential for ultrahigh efficiency with very low pollutant emissions. Future research includes detailed dynamic modeling of this fuel cell systems, and control of this hybrid systems.

APPENDIX A

JOURNAL PUBLICATIONS

1. Woon ki Na and Bei Gou, "Nonlinear Control of PEM Fuel Cells by Exact Linearization," *IEEE Transaction on IAS (Industrial Application Systems),* Volume 43, Issue 6, Nov.-Dec. 2007 Page(s):1426 - 1433.

2. Woon ki Na and Bei Gou, "Efficient and Economic Design of PEM Fuel Cell Systems by Multi-objective Optimization," *Journal of Power Sources,* Volume 166, Issue 2, 15 April 2007, Pages 411-418.

3. Woon ki Na and Bei Gou, "Feedback Linearization Based Nonlinear Control for PEM Fuel Cells," *IEEE Transaction on Energy Conversion,* 2008, Volume 23, Issue 1, March 2008 Page(s):179 – 190.

4. Woon ki Na and Bei Gou, "Nonlinear Control Approach for a New MIMO based Dynamic PEM Fuel Cells Model", *IEEE Transaction on Energy Conversion*, 2008 (Under review).

5. Woon ki Na and Bei Gou, "Design of temperature controller for PEM fuel cells system using Thermal Equivalent Circuit model," *IEEE Transaction on Energy Conversion, 2008* (Under review).

6. Woon ki Na and Bei Gou, "Analysis and Control of Bidirectional DC/DC Converter for Fuel Cell applications," *IEEE Transaction on Circuit and systems,* 2007 (Under review).

7. Woon ki Na and Bei Gou, "Supervisory Control of a Hybrid Power System with a PEM Fuel-Cell, PV and Ultracapacitor for Stand-Alone Residential Applications" was submitted to the *IEEE Transaction on Power Delivery,* 2008 (Under review).

APPENDIX B

CONFERENCE PUBLICATIONS

1. Woonki Na and Bei Gou, " Analysis and Control of Bidirectional DC/DC Converter for PEM Fuel Cell Applications," Accepted for presentation at 2008 *IEEE Power Engineering Society General Meeting, 200*8 to be held 20 - 24 July, 2008 in Pittsburgh, PA USA.

2. Woonki Na and Bei Gou**,** " A Thermal Equivalent Circuit for PEM Fuel Cell Temperature Control Design," Accepted for presentation at the *2008 IEEE International Symposium on Circuits and Systems*, Seattle, WA,USA, 18-21 May 2008.

3. Woonki Na and Bei Gou, " Supervisory Control of a Hybrid Power System with a PEM Fuel-Cell, PV and Ultracapacitor for Stand-Alone Residential Applications," Accepted for presentation at *UKC 2008*, US-Korea Conference on Science, Technology and Entrepreneurship, San Diego, 14-17 August 2008

4. Woonki Na and Bei Gou, " Efficient and Economic Design of PEM Fuel Cell Systems by Multi-objective Optimization," Accepted for poster presentation at the *NHA Annual Hydrogen conference* 2007, San Antonio.

5. Woonki Na and Bei Gou, "Exact Linearization Based Nonlinear Control of PEM Fuel Cells," Accepted for presentation and publication at the *IEEE Power Engineering Society General Meeting, 2007*,24-28 June 2007 Page(s):1 – 6.

6. Woonki Na " Nonlinear control of PEM fuel cells for automotive and power system applications," Invited for oral presentation at the *KSEA*(Korean-American Scientists and Engineers Association) North Texas Chapter Annual Conference, University of Texas at Arlington,USA, May 26, 2007

7. Woonki Na and Bei Gou "Multi-objective Optimization of PEM fuel cell systems for automotive applications," Invited for poster presentation at the *KSEA*(Korean-American Scientists and Engineers Association) North Texas Chapter Annual Conference, University of Texas at Arlington,USA, May 26, 2007

8. Woonki Na and Bei Gou, "An analysis of the dynamic performance of PEM fuel cells using a nonlinear model," Accepted for oral presentation at the *SIAM Conference on Control and It Applications* , June 29-July 1, 2007, San Francisco, California.

9. Woonki Na and Bei Gou, "Optimal Design of PEM fuel cell systems," Invited for poster presentation at the WBT(World's Best Technologies) Showcase, Arlington Convention Center, May 15-16, 2007, TX, USA.

10. Woonki Na and Bei Gou, "An Improved Nonlinear Control for PEM Fuel Cells," Accepted for oral presentation at the *IASTED conference on "Power and Energy Systems", IEEE PES,* Marina del Rey, CA, USA 2005.

11. Woonki Na and Bei Gou, "Nonlinear Control of PEM Fuel Cells by Exact Linearization," Accepted for oral presentation and publication in the proceedings at the *IEEE Industry Applications Conference*, 2005. Fourtieth IAS Annual Meeting. Volume 4, Oct. 2005, Page(s):2937 – 2943.

REFERENCES

[1] J. Larminie and A. Dicks, *Fuel Cell Systems Explained,* New York: Wiley, 2002.

[2] Rajashekrara, K. "Propulsion system strategies for fuel cell vehicles", SAE paper 2000-01-0369.

[3] F. Barbir and T. Gomez, "Efficiency and economics of PEM fuel cells", International Journal of Hydrogen Energy, Vol.22, No 10/11, pp. 1027-1037, 1997.

[4] A.M. Borbely and Jan G. Kreider, Distributed Generation: The Power Paradigm for the New Millennium, New York, CRC press, 2001.

[5] F. Barbir, *PEM Fuel Cells: Theory and Practice*, Elsevier Academic Press, 2005.

[6] J. Purkrushpan, A.G. Stefanopoulou, and H.Peng, "Control of fuel cell breathing," IEEE Control Syst. Mag., April 2004.

[7] J. Purkrushpan and H. Peng, Control of Fuel Cell Power Systems: Principles, Modeling, Analysis and Feedback Design, Germany: Springer, 2004.

[8] J. Purkrushpan, A.G. Stefanopoulou, and H. Peng, "Modeling and control for PEM fuel cell stack systems," Proc. Amer. Control Conf., Anchorage, AK, 2002, pp. 3117–22.

[9] J.C. Amphlett, R.M. Baumert, R.F. Mann, B.A. Peppy, P.R. Roberge, and A. Rodrigues, "Parametric modeling of the performance of a 5-kW proton exchange membrane fuel cell stack," Journal of Power Sources, 49, 349–56, 1994.

[10] R.F. Mann, J.C. Amphlett, M.A. Hooper, H.M. Jesen, B.A.Peppy, and P.R. Roberge, "Development and application of a generalized steady-state electrochemical model for a PEM fuel cell," Journal of Power Sources, v. 86, pp.173–180, 2000.

[11] M.J. Khan and M.T. Labal, "Dynamic modeling and simulation of a fuel cell generator," Fuel Cells no.1, pp. 97–104, 2005.

[12] P. Famouri and R.S. Gemmen, "Electrochemical circuit model of a PEM fuel cell," *IEEE Power Engineering Society General Meeting,* vol. 3, pp. 13–17, July 2003.

[13] L. You and H. Liu "A parametric study of the cathode catalyst layer of PEM fuel cells using a pseudo homogeneous model*," International Journal of Hydrogen Energy*, vol. 26, no. 9, pp. 991–999, Sept. 1991.

[14] G. Maggio, V. Recupero, and L. Pino, "Modeling polymer electrolyte fuel cells: An innovative approach," *Journal of Power Sources*, vol.101, no.2, pp. 275–285, Oct. 2001.

[15] A. Rowe and X. Li, "Mathematical modeling of proton exchange membrane fuel cells," *Journal of Power Source*, vol.102, no.1-2, pp. 82–96, Dec. 2001.

[16] C. Wang, M.H. Nehrir, and S.R. Shaw, "Dynamic model and model validation for PEM fuel cells using electrical circuits," *IEEE Trans.Energy Conversion,* vol.20, no.2, pp. 442–451, 2005.

[17] L.Y. Chiu, B. Diong and R.S. Gemmen, "An improve small-signal model of the dynamic behavior of PEM fuel cells," *IEEE Trans. Industry Applications*, vol. 40, no. 4, pp. 970–077, 2004.

[18] J.M. Correa, F.A. Farret, and L.N. Canha, "An analysis of the dynamic performance of proton exchange membrane fuel cells using an electrochemical model," IECON '01, The 27th Annual Conference of the IEEE Industrial Electronics Society, vol. 1, pp. 141–146, 2001.

[19] C.J. Hatiziadoniu, A.A. Lobo, F, Pourboghrat, and M. Daneshdoot, "A simplified dynamic model of grid connected fuel-cell generators," *IEEE Trans. Power Delivery,* 17(2), 467–73, 2002.

[20] M.Y. El-Sharkh, A. Rahman, M.S. Alamm, A.A. Sakla, P.C. Byrne, and T. Thomas, "Analysis of active and reactive power control of a stand-alone PEM fuel cell power plant," *IEEE Trans. Power Delivery,* 19(4), 2022–28, 2004.

[21] W. Yang, B. Bates, N. Fletcher, and R. Pow, "Control challenges and methodologies in fuel cell vehicle development," SAE paper 98C054, 1998.

[22] A. Sakhare, A. Davari, and A. Feliachi, "Fuzzy logic control of fuel cell for stand-alone and grid connection," *Journal of Power Sources,* vol. 135, no. 1-2, pp. 165–176, Sept. 2004.

[23] Almeida and M. Godoy, "Neural optimal control of PEM fuel cells with parametric CMAC network," *IEEE Trans. Industry Applications,* vol. 41, no.1, pp. 237–245, 2005.

[24] M.J. Khan and M.T. Labal, "Modeling and analysis of electro chemical, thermal, and reactant flow dynamics for a PEM fuel cell system," Fuel cells, no.4, pp. 463–475, 2005.

[25] Ballard Power System, Inc., Canada, at http:/www.ballard.com.

[26] M.P. Nielsen, P. Pedersen, C.A. Andesen, M.O. Christen, and A.R. Korgaard, "Design and Control of Fuel Cell System for Transport Application," Aalborg University, project report, 2002.

[27] J.J.E. Slotine and W. Li, *Applied Nonlinear Control*. Englewood Cliffs, N.J.: Prentice Hall, 1991.

[28] Woonki Na and Bei Gou, "Feedback Linearization Based Nonlinear Control for PEM Fuel Cells," Accepted for publication on the *IEEE Transactions on Energy Conversion*, 2007.

[29] J. Sun and V. Kolmannovsky, "Load governor for fuel cell oxygen starvation protection: A robust nonlinear reference governor approach," *IEEE Trans. Control Systems Technology*, 3(6), 911–13, 2005.

[30] S. Basu, M.W. Renfro and B.M. Cetegen, **"**Spatially resolved optical measurements of water partial pressure and temperature in a PEM fuel cell under dynamic operating conditions" *Journal of Power Sources*, 162(1), 286–93, 2006.

[31] R.E. Sonntag, C. Borgnakke, and G.J. V. Wylen, *Fundamentals of Thermodynamics*. New York: Wiley, 1998.

[32] W. Yang, B. Bates, N. Fletcher, and R. Pow, "Control challenges and methodologies in fuel cell vehicle development," SAE paper 98C054, 1998.

[33] B. W. Bequette, "Nonlinear control of chemical process: A review," Ind. Eng. Chem. vol. 30, pp. 1391–1413, 1991.

[34] M. A. Henson and D.E. Seborg, "Critique of exact linearization strategies for process control," Journal of Process Control, vol. 1, pp. 122–139, May 1991.

[35] A. Isidori, *Nonlinear Control Systems,* 3rd Ed. London: Springer Verlag, 1995.

[36] J. J. E. Slotine and W. Li, *Applied Nonlinear Control*. Englewood Cliffs, NJ: Prentice Hall, 1991.

[37] Q. Li, Y. Sun, and S. Mei, *Nonlinear Control Systems and Power System Dynamics*. Klunmer Academic Publishers, 2001.

[38] H. Nijmeijer and A.J. Van der Schaft, *Nonlinear Dynamical Control Systems,* Springer Verlag, 1990.

[39] J. Hamelin, K. Abbossou, A. Laperriere, F. Laurencelle, and T.K. Bose, "Dynamic behavior of a PEM fuel cell stack for stationary application," *International Journal of Hydrogen Energy*, 26, 625–29, 2001.

[40] R. W. Erickson, D. Maksimovic, Fundamentals of Power Electronics, Kluwer Academic Publishers, 2000.

[41] U.S. Department of Energy, Fuel cell handbook, 6th Ed., EG&G technical service Inc., 2002.

[42] Blunier, B. and Miraoui, A, "Optimization and air supply management of a polymer electrolyte fuel cell**",** Vehicle Power and Propulsion, 2005 IEEE Conference.

[43] P. Pei, W. Yang and P. Li, "Numerical prediction on an automotive fuel cell driving system", Int.J. Hydrogen Energy, Vol.31, pp 361-369, 2006.

[44] Cunningham JM, Hoffman Ma, et all, "The implications of using an expander in an air system of a PEM fuel cell engine ", Proceedings of the 17th international electric vehicle symposium & exposition, Montreal, Canada, October, 2000.

[45] Boyer, C. C., Anthony, R.G., and Appleby,A.J., "Design equations for optimized PEM fuel cell electrodes", Journal of Applied Electrochemistry, vol 30, pp777-786, 2000.

[46] Tomas CE, Barbour JP, James BD, Lomax FD, " Cost analysis of stationary fuel cell systems including hydrogen cogeneration" ACG-8-18012-02, Colorado: National Renewable Energy Laboratory; 1999.

[47] E. J. Carlson, P. Kopf, Sinha, S. Sriramulu and Y. Yang, "Cost analysis of PEM fuel cell systems for Transportation", TIAX LLC, Cambridge, MA, 2005.

[48] C. A. Frangopoulos, and L.G. Nakos, "Development of a model for thermoeconomic design and operation optimization of a PEM fuel cell system", Energy vol 31, pp1501-1519, 2006.

[49] H. Tsuchiya, and O. Kobayashi, "Mass production cost of PEM fuel cell by learning curve", International Journal of Hydrogen Energy vol. 29, pp 985-990, 2004.

[50] S. Kamarudin, W. Daud, A. Som, M. Takriff and A. Mohammad, " Technical design and economic evaluation of a PEM fuel cell system", Journal of Power Source, vol 157, pp 641-649, 2006.

[51] E. J. Carlson, P. Kopf, Sinha, S. Sriramulu and Y. Yang, "Cost analysis of PEM fuel cell systems for Transportation", TIAX LLC, Cambridge, MA, 2005.

[52] Optimization toolbox for use with Matlab ver.2 by Mathwork.

[53] L. Solero, A. Lidozzi, and J. A. Pomilio, "Design of Multiple-Input Power Converter for Hybrid Vehicles," *IEEE Trans. Power electronics,* 20(5), 1007–1016, 2005.

[54] A. Drolia, P. Jose, and N. Mohan, "An approach to connect ultracapacitor to fuel cell powered electric vehicle and emulating fuel cell electrical characteristics using switched mode converter," The 29th Annual Conference of the *IEEE Industrial Electronics* Society IECON '03, Vol. 1, 2-6 Nov. 2003, pp. 897 – 901.

[55] P. Thounthing, S. Rael, and B. Davat "Control strategy of fuel cell/supercapacitor hybrid power sources for electric vehicle", *Journal of Power Source*, 158, 806–814, 2006.

[56] M. Uzunoglu, and M. S. Alam, "Dynamic modeling, design and simulation of a PEM fuel cell/ultracapacitor hybrid system for vehicular applications," *Journal of Power Sources*, 48, 1544–1553, 2007.

[57] M. Uzunoglu, and M. S. Alam, "Dynamic modeling, design and simulation of a combined PEM fuel cell and ultracapacitor system for stand alone residential applications," *IEEE Trans. Energy Conversion,* 21(3), 767-775, 2006.

[58] K. H. Hauer, "Analysis tool for fuel cell vehicle hardware software(control) with an application to fuel economy comparisons of alternative system designs," Ph.D dissertation, Dept. Transport. Techno. Policy, Univ. Ca, Davis, CA, 2001.

[59] N. Mohan, T.M. Underland and W. P. Robibins *Power Electronic;Converter, Applications, and Design, Second Edition*, John Wiley & Sons, Inc.

[60] S. Franco, "*Design with Operational Amplifiers and AnalogIntegrated Circuits*," New York, McGraw-Hill (3rd Ed.), 2001.

[61] Electric Double Layer Capacitor: BOOSTCAP Ultracapacitor,Available:

http:/www.maxwell.com/pdf/uc/datasheets/PC2500.pdf.

[62] F. Valenciaga, P.E. Puleston, and P.E.Battaiotto, “Power control of a photovoltaic array in a hybrid generation system using sliding mode techniques”, IEE Proc.-Control theory Appl,, Vol.148, No.6, Nov. 2001, pp.448-455.

[63] S. K. Kim, J. H. Jeon, C. H. Cho, J. B. Ahn, and S. H. Kwon, “ Dynamic Modeling and Control of a Grid-Connected Hybrid Generation System with Versatile Power Transfer”, Industrial Electronics, IEEE Transactions on : Accepted for future publication.

[64] Rajashekara, K., “Hybrid fuel-cell strategies for clean power generation”, Industry Applications, IEEE Transactions on Volume 41, Issue 3, May-June 2005 Page(s): 682 – 689.

[65] Tao Zhou; Francois, B.; el hadi Lebbal, M.; Lecoeuche, S, “Modeling and Control Design of Hydrogen Production Process by Using a Causal Ordering Graph for Wind Energy Conversion System ”,Industrial Electronics, 2007. ISIE 2007, IEEE International Symposium on 4-7 June 2007 Page(s):3192 – 3197

[66] Agbossou, K.; Hamelin, J.; Laperriere, A.; Laurencelle, F.; Bose, T.K.;”Load commutation for stand alone wind and PV hydrogen energy system”, Electrical and Computer Engineering, 2000 Canadian Conference on Volume 1, 7-10 March 2000 Page(s): 555 – 558.

[67] Hussein, K. H., Muta, I., Hoshino, T., and Osakada, M., “Maximum photovoltaic power tracking,” *IEE Proc., Gener. Transm. Distrib. Ind. Electron.*, 1998, 45,(1), pp. 59-64.

[68] Woonki Na and Bei Gou, "Efficient and Economic Design of PEM Fuel Cell Systems by Multi-objective Optimization," *Journal of Power Sources*, Volume 166, Issue 2, 15 April 2007, Pages 411-418**.**

[69] G. Georgiou, G., and Pioufle, B.L., “Nonlinear speed control of a synchronous servomotor with robustness,” *EPE proc., Firenze,* pp. 3-42–3-48, 1991.

[70] D. Xue and Z. Dong, “ Optimal fuel cell system design considering functional performance and production costs”, Journal of Power Sources, vol 76, pp 69-80, 1998.

BIOGRAPHICAL INFORMATION

Woon Ki Na received the B.S. and M.S. degrees in Electrical Engineering from Kwangwoon University, Seoul, South Korea, in 1995 and 1997, respectively. He worked for T.H.ELEMA in Ansan, South Korea and LG Electronics in Seoul, South Korea as Power Electronics Engineer and Research Engineer from 1997 to 2001. He has been pursuing a Ph.D. degree in the Electrical Engineering Department at the University of Texas at Arlington since 2003. His research interests include power electronics, power systems, nonlinear control design, and integration of renewable energy systems and fuel cell vehicle systems.